CHARACTERIZATION OF THE HAMAMATSU R1449 PHOTOMULTIPLIER TUBE

by

Robert John Komar

A thesis submitted to the Department of Physics
in conformity with the requirements for
the degree of Master of Science

Queen's University
Kingston, Ontario, Canada
November, 1987

Copyright ©Robert John Komar, 1987

Abstract

The Sudbury Neutrino Observatory (SNO) Collaboration proposes to build a large underground heavy water Čerenkov detector for the detection of solar neutrinos. The Čerenkov radiation from the fast electrons produced by neutrino interactions will be detected by photomultiplier tubes (PMT's) placed outside the D_2O volume. A characterization of the Hamamatsu R1449 20″ diameter PMT was performed so that its suitability for the SNO detector could be determined. The tests were performed at the single photoelectron level using a weak pulsed light source of wavelength 650 ± 10 nm (fwhm), and pulse width ≤1.9 nsec fwhm. The timing resolution and transit time differences for spot illumination over the photocathode were measured, and the transit time spread (TTS) was deduced from this to be ~10.4 nsec. From computer simulations of photoelectron trajectories, it was found that most of the TTS is produced in the dynodes, and that magnetic fields ≥0.1 gauss will reduce the photoelectron collection efficiency by $\geq5\%$.

Acknowledgements

I would like to show my appreciation to my two advisors, Drs. H.-B. Mak and B.C. Robertson, without whose aid, guidance and patience this work could not have been performed; and to acknowledge that a good part of my education has come from the example set by these two men.

I would like to express my gratitude to the rest of the Queen's Nuclear Physics Dept. (professors, staff and students) for providing an environment dedicated to learning and growth, to the entire Queen's Physics Dept. for more of the same, and to Dr. Peter Skensved for his invaluable assistance on the computers.

Special thanks go to the two Toms, Radcliffe and Goetz, for their friendship, humour and willingness to hold forth on and hash out any ideas that cropped up. Extra special thanks to Phil Matthews, my long-term housemate and pal.

Contents

List of Figures

List of Tables

List of Abbreviations

ADC	analogue-to-digital converter
Amp.	amplifier
CFD	constant fraction discriminator
DCF	double constant fraction
fwhm	full width at half maximum
GDG	gate and delay generator
LE	leading edge
LEAC	leading edge amplitude compensated
LED	light emitting diode
LGS	linear gate and stretcher
MCA	multichannel analyzer
p.e.	photoelectron
PMT	photomultiplier
PSA	pulse shape analyzer
SNO	Sudbury Neutrino Observatory
SPR	single photoelectron response
TAC	time-to-amplitude converter

TFA	timing filter amplifier
TSCA	timing single channel analyzer
TT	transit time
TTD	transit time difference
TTS	transit time spread

Chapter 1

Introduction

Since 1970, the ongoing Cl/Ar radiochemical experiment of R. Davis *et al.* for detecting solar neutrinos had produced a ν_e flux measurement a factor of four or more lower than that predicted by the standard solar model [Ba85]. In that experiment [Ro85], a tank of liquid perchloroethylene (C_2Cl_4) is used to detect solar ν_e through the inverse beta process

$$^{37}\mathrm{Cl}\ + \nu_e\ \rightarrow {}^{37}\mathrm{Ar}\ + e^-$$

At regular intervals (~2 months), the tank is purged and the radioactive ^{37}Ar atoms are separated out. From the ^{37}Ar activity, the ν_e capture rate, and thus the ν_e flux, is deduced. The experiment is mainly sensitive to the high energy ν_e from the beta decay of ^{8}B produced within the sun. The discrepancy between the ^{8}B ν_e flux deduced from the Cl/Ar experiment and that predicted by the standard solar model is considered to be an important problem in modern physics, and theories to explain the discrepancy have been extensively discussed. One class of theories attributes the problem to an incorrect solar model [Ku76]. Other theories, concerning the propagation of neutrinos, attribute the reduced ν_e flux at the earth either to neutrino decay [Ba86], a neutrino magnetic moment or oscillation of the three neutrino flavours [Wo79]. To verify these theories, experimental information on the total ^{8}B neutrino flux is needed.

To resolve this solar neutrino problem, the Sudbury Neutrino Observatory (SNO) Collaboration proposes to detect solar neutrinos using a large underground heavy water Čerenkov detector [Ch85]. The detector is designed to yield the energy and the direction of motion of fast electrons produced through neutrino interactions. The neutrinos would be identified through the three reactions [Aa87]

$$\nu_e + d \rightarrow p + p + e^- \tag{1.1}$$

$$\nu_x + e^- \rightarrow \nu_x + e^- \tag{1.2}$$

$$\nu_x + d \rightarrow \nu_x + p + n \tag{1.3}$$

where ν_x is any left-handed neutrino. Unlike the Cl/Ar experiment, the heavy water detector would be sensitive to ^{8}B neutrinos of all flavours. In the case of the charged-current reaction (1.1), the electron is emitted with most of the kinetic energy from the reaction (E$_\nu$ - 1.44 MeV) [Ke66], and with an angular distribution with respect to the neutrino direction given by $W(\theta_e) = 1 - \frac{1}{3}\cos\theta_e$. The secondary electron from reaction (1.2), however, is scattered in a forward direction with respect to the neutrino's initial direction, and thus could be separated from that of reaction (1.1). Hence, the ^{8}B ν_e flux, spectrum and direction would be deduced through reaction (1.1), and the total ^{8}B neutrino flux, integral spectrum and direction would be deduced through reaction (1.2). From standard electroweak theory, the cross-section for ν_e scattering from electrons [Al85] is expected to be six times larger than that for ν_μ [Ah83] or ν_τ. Thus, the deduced total ^{8}B neutrino flux from reaction (1.2) would depend on the results from reaction (1.1). An independent measurement of the total ^{8}B neutrino flux would be obtained through the neutral-current reaction (1.3), where the cross-section is independent of neutrino flavour. In this case, the 6.25 MeV gamma ray produced through the $d(n,\gamma)t$ capture reaction would produce fast electrons through the photoelectric, pair production and Compton interactions. The direction of motion of the electrons would be random with respect to the neutrino's initial direction of motion.

The fast electrons produced in neutrino or gamma interactions in the D_2O emit Čerenkov radiation (a few hundred photons per MeV of electron energy, mostly in the ultraviolet). The Čerenkov light is emitted preferentially along the direction of the electron's velocity, and is confined to a cone of vertex angle θ given by

$$cos\theta = \frac{1}{\beta n}$$

where β is the fraction of the velocity of light at which the electron is travelling, and n is the index of refraction of the water. The Čerenkov photons are detected by photomultiplier tubes (PMT's) located in the light water outside the heavy water tank (see figure 1.1). The position and time of production of the fast electron (X_0, Y_0, Z_0, T_0) is calculated by minimizing the χ^2 given by [Sn87]:

$$\chi^2 = \frac{\sum_{i=1}^{NPTS} \left[R_i - \Delta T_i \cdot \frac{c}{n}\right]^2}{(NPTS - 4)}$$

$$\begin{aligned} R_i &= \sqrt{(X_i - X_0)^2 + (Y_i - Y_0)^2 + (Z_i - Z_0)^2} \\ \Delta T_i &= T_i - T_0 \end{aligned}$$

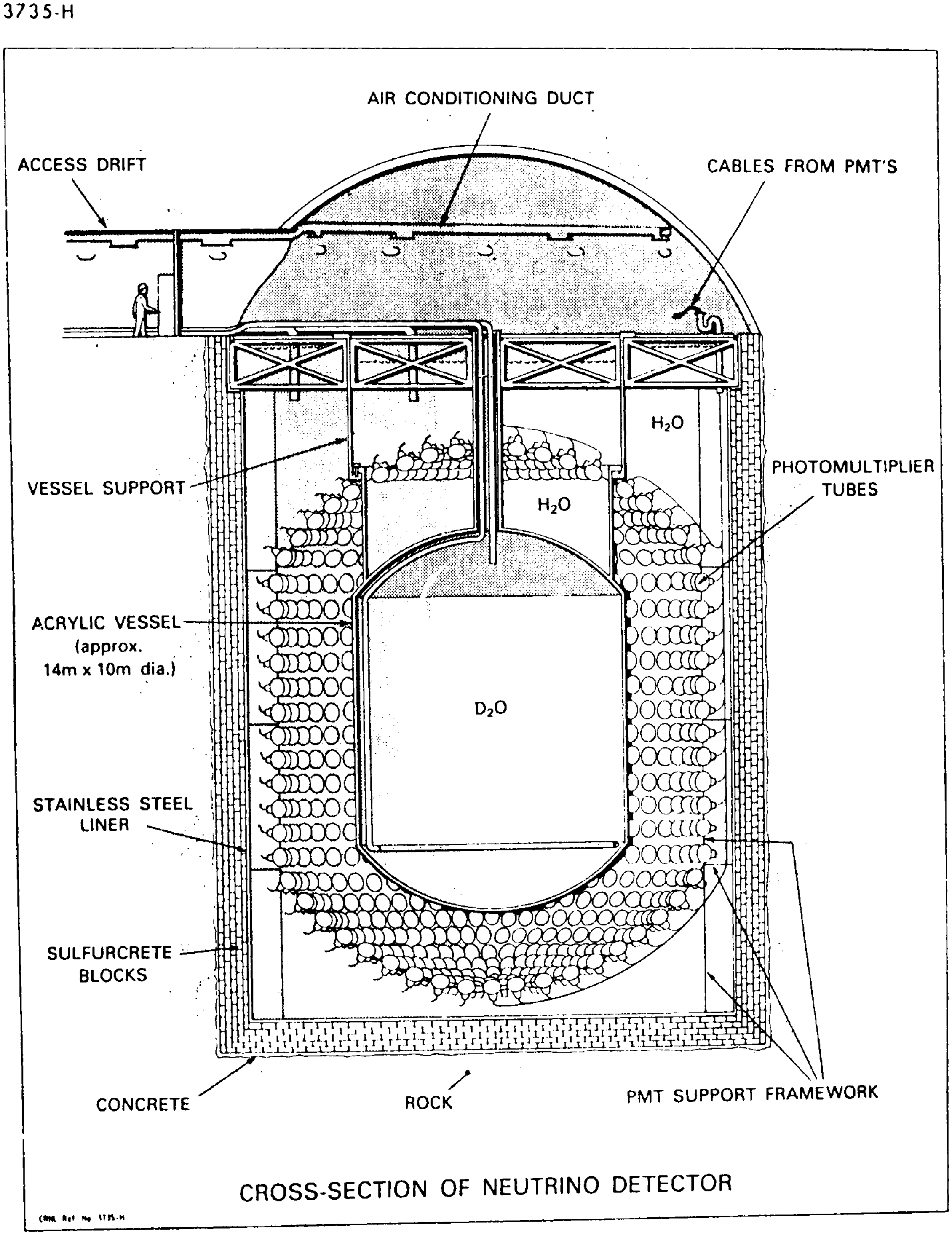

Figure 1.1: Conceptual design of the SNO underground heavy water Čerenkov detector [Mc87]. The Čerenkov light produced through neutrino interactions in the heavy water is detected by the PMT's placed in the surrounding light water tank.

where $NPTS$ is the number of PMT's triggered, (X_i, Y_i, Z_i, T_i) is the position of PMT$_i$ and the time at which it was struck by the Čerenkov photon, and c/n is the local speed of light in water. The space-time coordinates of the fast electron are treated as free parameters and varied until the value of (X_0, Y_0, Z_0, T_0) is found which minimizes the χ^2. The energy of the fast electron is deduced from the number of PMT's triggered, and its direction is deduced from the vector sum of the position vectors from the vertex to each triggered PMT.

For good energy resolution the PMT's must be efficient, and must cover a large fraction of the heavy water tank's surface area. The timing resolution of the PMT's must be good for several reasons. Accurate reconstruction of the electron's position is needed, as the direction of motion of the electron is deduced from this. Also, the spatial resolution of the reconstruction must be good to reduce the chance of mapping interactions in the light or heavy water tanks into each other, and thus decreasing the signal-to-noise ratio of the detector. Finally, good PMT timing resolution allows tighter time windows to be set around the true events to reduce background counts due to PMT dark noise and natural radioactivity in the detector.

The Hamamatsu R1449 20″ diameter PMT (see figure 1.2) was designed for the large underground light water Čerenkov detector at Kamioka, Japan, making it a good candidate for use in the SNO detector. The purpose of this work is to characterize this PMT, so that its suitability for the SNO project can be determined. An important part of the characterization is the measurement of the timing resolution of the PMT, which is best described by the transit time spread (TTS). The electron transit time is the time between the photoelectron's production by the incident light

Figure 1.2: The Hamamatsu R1449 20″ diameter photomultiplier tube designed for detecting Čerenkov light in water.

photon and the PMT's output pulse reaching its maximum amplitude. Due to the fluctuations in the initial energies and paths of the electrons inside the PMT's, the transit time varies from pulse to pulse. The TTS is defined as the full width at half maximum (fwhm) of the electron transit time distribution. Measurements using the electronics at Kamioka on one hundred of the R1449 PMT's indicate that the average single photoelectron timing resolution is 12.5 nsec fwhm [Su87]. In the present work, measurements of the TTS of the R1449 PMT were performed using various timing techniques to determine which gives the best timing resolution. The dark noise rate of the PMT was measured to determine if it is low enough to ensure that true signals from the heavy water will not be buried in PMT noise, and the single photoelectron response of the PMT was measured to determine if the signals generated by Čerenkov light can be distinguished from some of the PMT noise based on the pulse height. In addition, photoelectron trajectories were simulated by computer to determine their contribution to the TTS, and to gauge the effects of magnetic fields on the timing and efficiency of the PMT. With this information, an evaluation of the PMT's suitability can be made by the designers of the heavy water detector.

Chapter 2

Theory

2.1 The Photomultiplier Tube

The photomultiplier tube is a photosensitive detector that converts weak light signals into current pulses. It consists of a photoemissive cathode (photocathode), focussing electrodes, an electron multiplier and an electron collector (anode), all contained within an evacuated glass envelope. The basic elements of a typical transmission-type PMT, the Philips 56AVP [Ph70], are shown in figure 2.1.

The incident photons initially pass through the window of the PMT. Some of these photons interact in the semi-transparent photocathode, producing photoelectrons. These photoelectrons are focussed onto the first stage of the electron multiplier. Through charge multiplication due to secondary emission in each of the stages of the multiplier, a pulse of typically 10^6 electrons is produced. This pulse is then collected by the anode and passed out of the PMT. The time taken for this whole process is termed the transit time. In the following subsections, each of the components in a PMT will be discussed in further detail, with particular emphasis on its effects on the timing performance of PMT's.

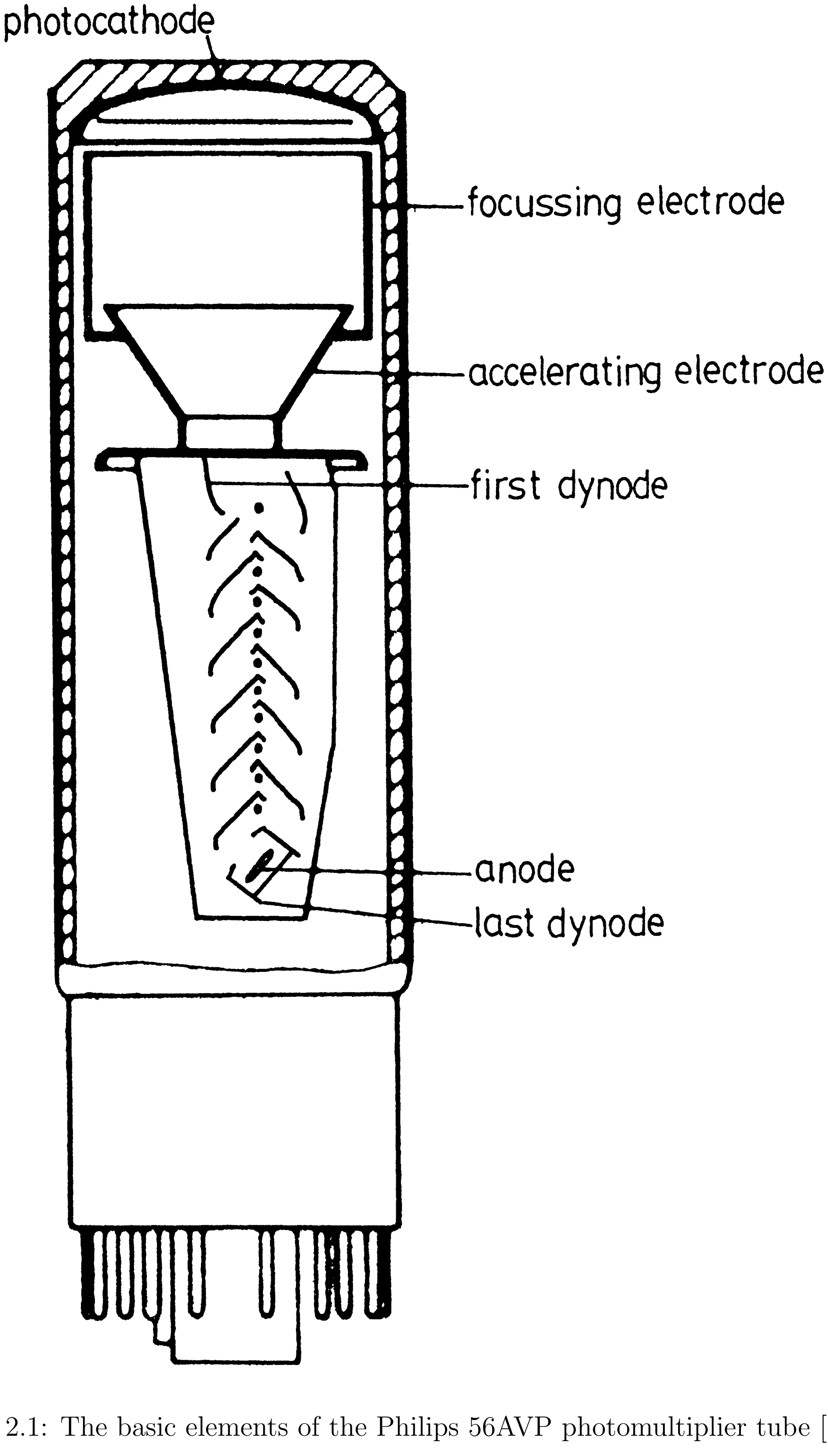

Figure 2.1: The basic elements of the Philips 56AVP photomultiplier tube [Ph70].

2.1.1 The Photocathode

The incident radiation striking the photocathode must first pass through the window of the PMT. All window materials are made of glass, with a short wavelength cutoff below which most photons are absorbed. For ordinary glass, the cutoff wavelength is in the ultraviolet range at about 350 nm [Rc80]. However, there are special types of glass with cutoffs as low as 200 nm [Rc80]. Thus, the choice of the window material will determine the sensitivity of the PMT at short wavelengths. Besides the cutoff, there are other factors to be considered in choosing a window material. The SNO project requires large photocathode coverage at reasonable costs, and the PMT's will be kept underwater at depths in excess of 20 m. The window material will have to be strong, resistant to water corrosion, and easily worked into the large envelope required.

For the transmission-mode tubes used in scintillation detection and photon counting, the window is also the backing upon which the photocathode material is deposited. Electrons are ejected from the photocathode via the photoelectric effect. The process can be visualized as a three-stage process:

1. the incident light photon is absorbed in the photocathode. Its energy is transferred to an electron which is promoted from the valence band to the conduction band.

2. the electron migrates to the surface of the material.

3. if it has enough energy to overcome the electron affinity at the surface, it escapes from the photocathode.

The total time for the production of photoelectrons is typically less than 0.1 nsec [Rc80].

To leave the photocathode surface, the valence electrons must be given at least as much energy as the sum of the band gap energy and the electron affinity of the material. Thus, there is a minimum photon energy below which photoemission will not occur. Depending on the type of photocathode material, this long wavelength cutoff is usually in the red to infrared part of the spectrum. Thus, all PMT's have a low frequency as well as a high frequency cutoff. This spectral response is an important parameter in choosing a particular PMT for an experiment.

In addition to the ejected photoelectrons, there will be electrons in the conduction band with enough thermal energy to overcome the electron affinity and escape from the photocathode. Since this thermal emission of electrons is not related to the incident photons, it represents a source of noise. As might be expected, the thermionic noise rate depends on the temperature of the photocathode, as well as the type of material. Figure 2.2 shows typical thermionic emission current density characteristics for a few photocathodes as a function of reciprocal temperature [Rc80]. Due to their larger work functions, the bialkali photocathodes exhibit the lowest thermionic noise rates.

2.1.2 The Focussing Electrodes

Once the photoelectrons leave the photocathode, they are guided into the electron multiplier by an electric field produced by the focussing electrodes. The electrodes and multiplier are held at positive potential with respect to the photocathode, and

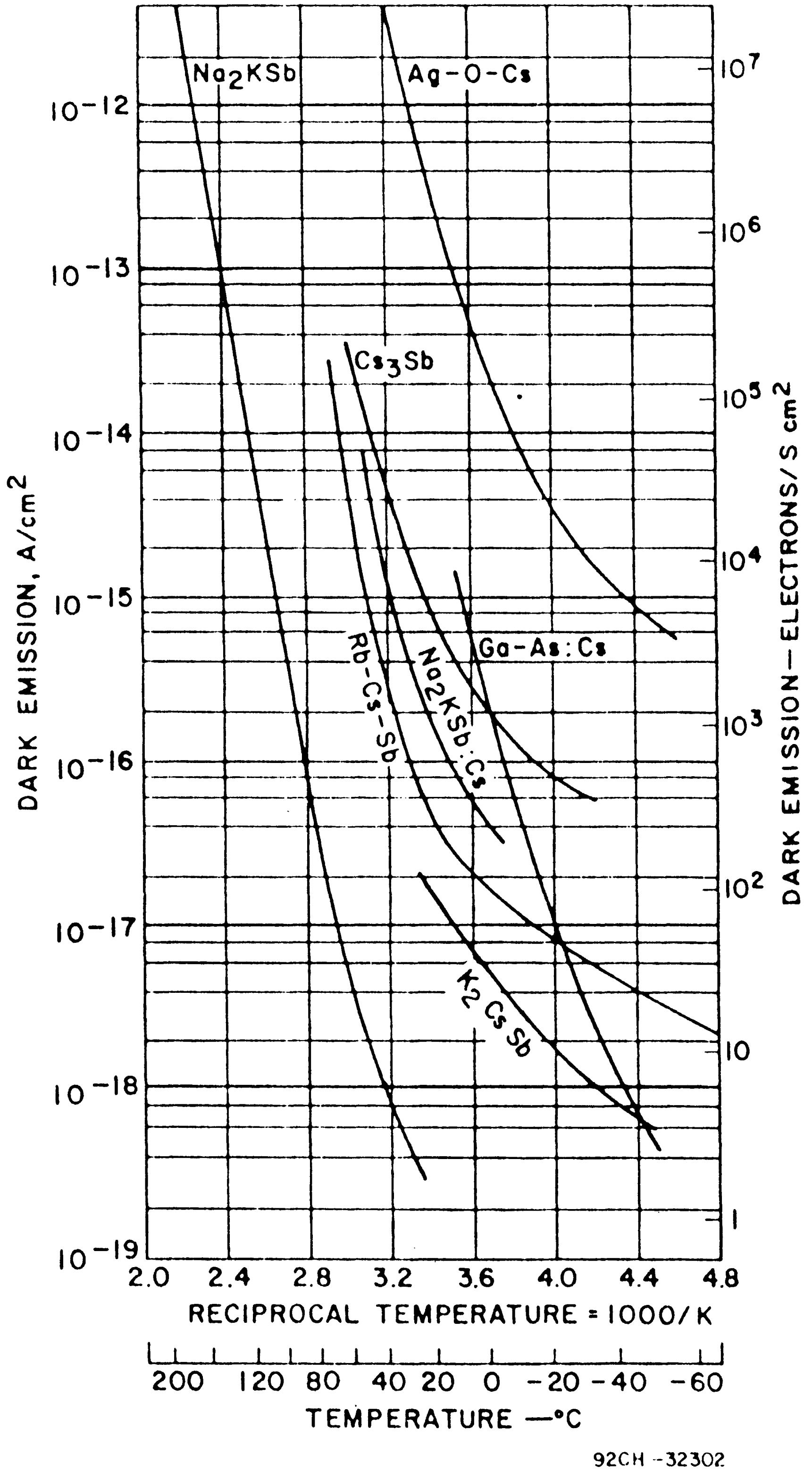

Figure 2.2: Thermionic emission current density as a function of reciprocal temperature for some typical photocathode materials [Rc80, fig. 16].

are arranged so that most of the photoelectrons will be incident on the first stage of the multiplier. Figure 2.3 illustrates some calculated equipotential lines and electron trajectories in the Hamamatsu R1449 PMT.

Ideally, the PMT should be designed for maximum efficiency, so that every photoelectron is collected. For good timing resolution, the time of flight between the photocathode and first dynode should be equal for all photoelectrons. However, not only are the flight times usually different for photoelectrons originating form differing points on the photocathode, they can differ substantially for photoelectrons originating from the same point, since the photoelectrons are emitted with various initial velocities. Thus, there will always be some variation in their flight times, and this will contribute to the transit time spread of the PMT. In general. the timing resolution can be improved by not collecting the photoelectrons with widely deviating flight paths.

Depending on the design of each particular tube, the average photoelectron flight time will typically fall within the range of five to twenty nanoseconds. Variations in the flight time will generally increase with longer flight times, that is, for larger tubes and smaller accelerating potentials. The best timing resolution is obtained with small PMT's and large applied voltages. The flight time spread will also depend on the incident photon energy, as those photons with higher energies will eject photoelectrons with, on average, higher initial velocities. Since the photoelectrons are emitted in all directions, higher initial velocities mean larger variations in flight paths and times. Figure **??** shows the single photoelectron time spectra from a Philips 56CVP PMT measured for different wavelengths of incident light [Mo77]. It was shown that, for

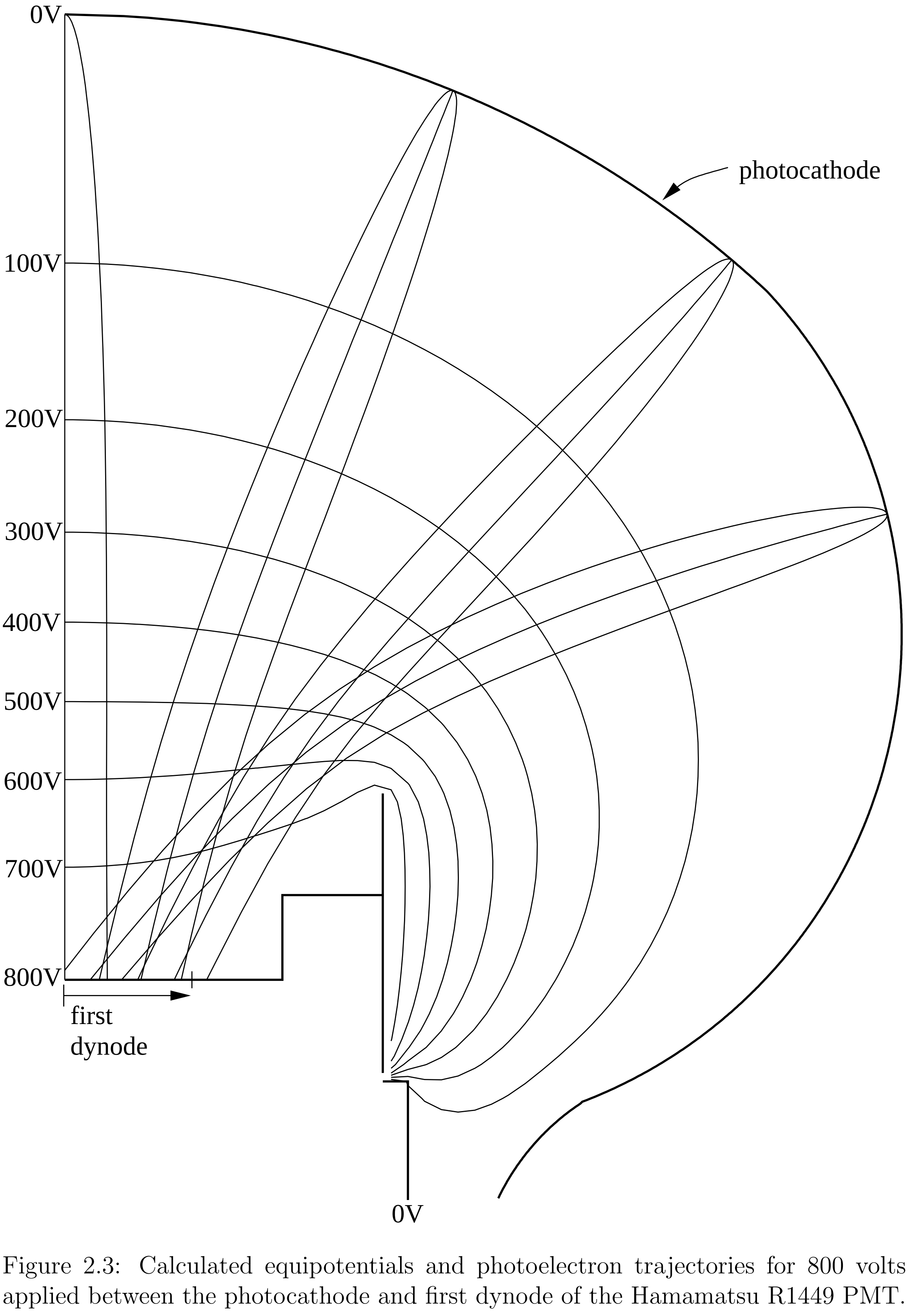

Figure 2.3: Calculated equipotentials and photoelectron trajectories for 800 volts applied between the photocathode and first dynode of the Hamamatsu R1449 PMT. The paths shown are tracked for an initial electron energy of 0.5 eV and emission angles of 0° and ±90°.

this PMT, the flight time spread is proportional to the square root of the maximum initial energy of the photoelectrons (the photocathode and electrode shapes of this PMT are similar to that shown in Figure 2.1). This simple relation is not expected to hold for the more complicated geometry of the Hamamatsu R1449 PMT. However, there will probably be some systematic increase in the TTS with increasing photon energy.

2.1.3 The Electron Multiplier

For most nuclear physics applications, the number of photoelectrons emitted from the photocathode per pulse is usually less than a few thousand, but can be as low as one in some photon counting applications (such as the SNO project). These are very weak signals, and must be amplified before they can be handled by standard electronics. The amplification is done in the electron multiplier of the PMT, where charge gains of about six orders of magnitude are typical.

Figure 2.5 shows a simplified version of an electron multiplier with an in-line focussed dynode structure [Rc80]. The photoelectrons from the photocathode are directed onto the first dynode, where they slow down and transfer their energies to other electrons, ejecting them from the dynode's surface (this is known as secondary emission, a process similar to photoemission). These secondary electrons are then accelerated to the next dynode by an electrostatic field, where they, in turn, produce more secondary electrons. This is repeated from stage to stage until the electrons are ejected from the last dynode, and are collected by the anode.

Like the photoemission process, the time taken for secondary emission is typi-

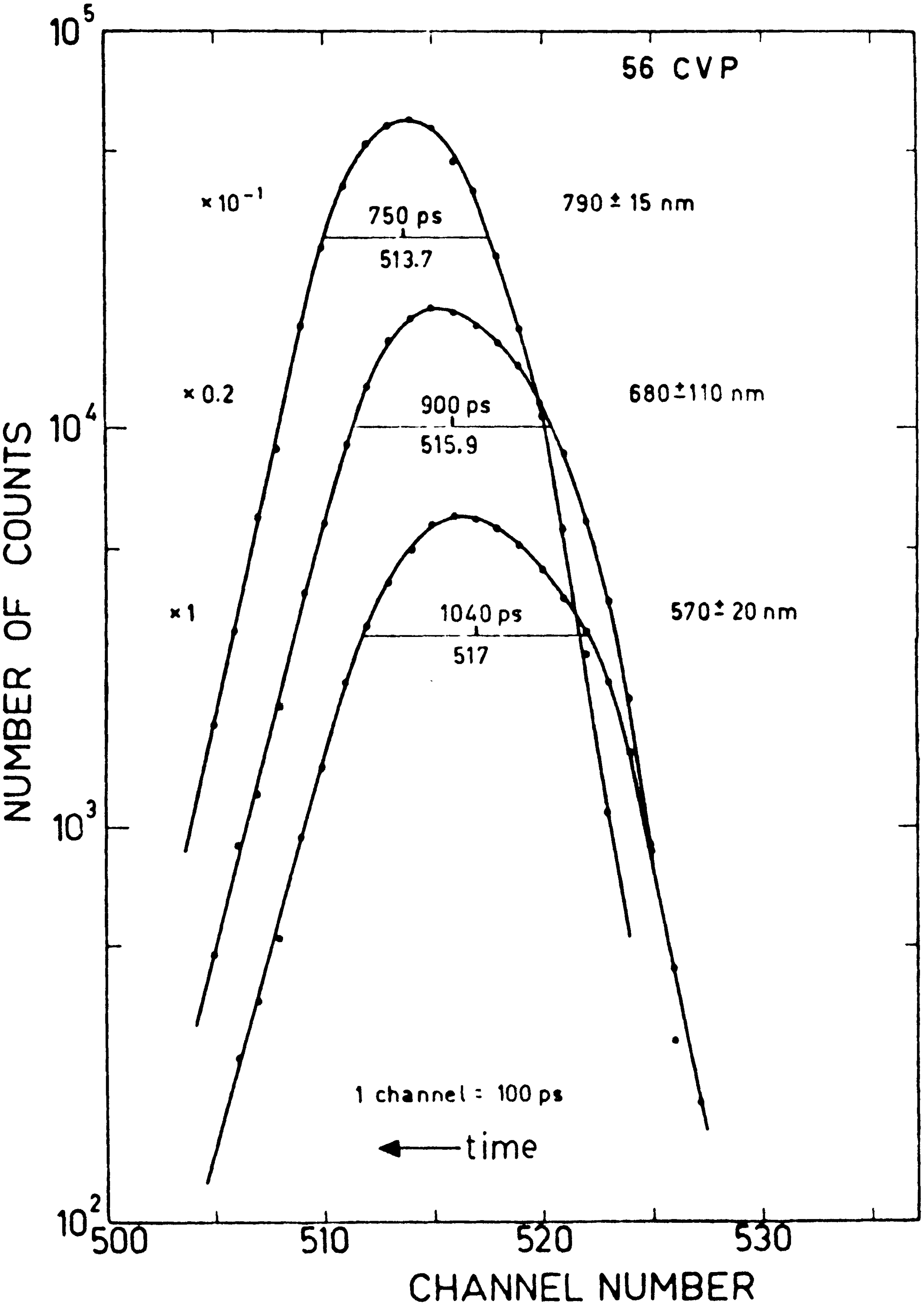

Figure 2.4: Single photoelectron timing spectra measured with the Philips 56CVP PMT for three wavelengths of incident light [Mo77, fig. 2]. Note the systematic increase in the transit time spread with increasing incident light energy.

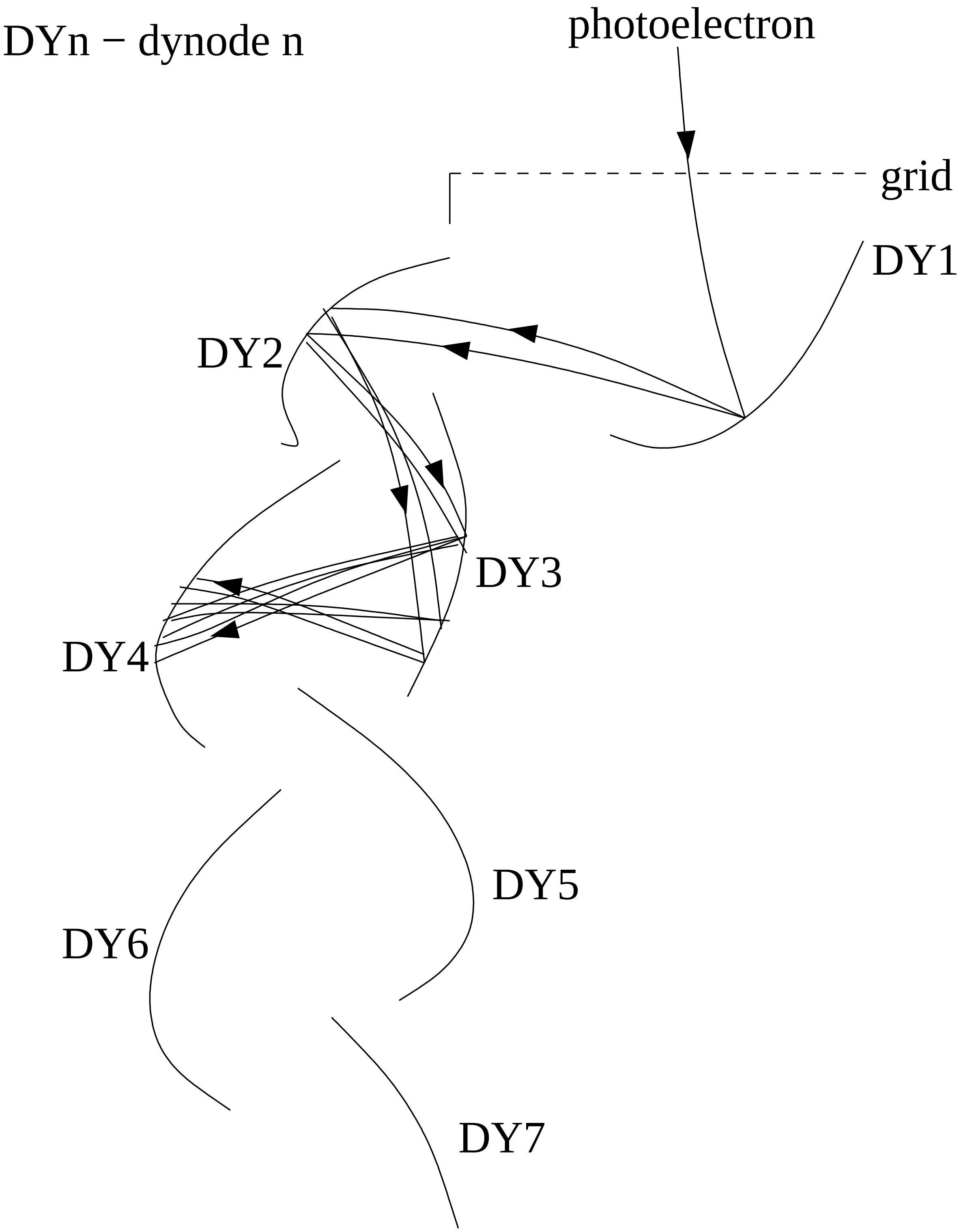

Figure 2.5: Schematic diagram of charge multiplication through secondary electron emission in an in-line focussed dynode structure [Rc80], with a secondary emission ratio of two. To produce nearly equal transit times through the multiplier, larger electron paths and weaker fields alternate with shorter paths and stronger fields from dynode to dynode.

cally less than 0.1 nsec [Rc80]. This means that the secondary electrons spend most of their time in flight between the dynodes. The multipliers are designed to minimize flight path differences between each stage. Because the secondary electrons are produced by random scattering interactions rather than photoabsorption, the initial velocity spread is even greater for the secondary electrons than for the photocathode photoelectrons. It is this spread that has the greatest adverse effect on a multiplier's timing properties [Le75].

A good way to combat this problem is to increase the electric field strength at the dynode surfaces. This would reduce the effects of the differences in the initial velocities of the secondary electrons. The multipliers with the best timing properties have their dynodes configured so that the electric field is strongest at their surfaces (a good example is the in-line focussed structure shown in figure 2.5). The time response is also improved by operating the PMT at its maximum voltage rating, as this maximizes the field strength. The transit time through the multiplier depends on the number of dynode stages and on the physical size of the multiplier. The number of stages used in most PMT's ranges from four to fourteen, and the multiplier transit times range from about ten to fifty nanoseconds. Those with small structures and few stages have the best timing properties.

2.1.4 The Anode

The electrons emitted from the last stage of the multiplier are collected by the anode, producing a current pulse. For good timing resolution, the risetime and width of the current pulse should be as short as possible, and care must be taken to ensure that the anode does not degrade the pulse. For example, the stray capacitance of the anode should be kept small to avoid reducing the amplitude and increasing the decay time constant of the signal, the anode impedance should be matched to that of the outside circuit to avoid ringing, and a large electric field should be applied between the anode and the last dynode to reduce space-charge effects caused by the large number of electrons coming from the last stage of the multiplier.

2.1.5 The Voltage Divider

To accelerate the electrons from the photocathode to the multiplier, the first dynode must be held at a positive potential with respect to the photocathode, and each subsequent dynode must be at a higher potential than the one before it. This is usually accomplished by applying a single large potential across the cathode and anode, and picking the intermediate voltages off a resistive voltage divider between the two. Figure 2.6 shows the two most common designs for voltage dividers. Figure 2.6a shows the scheme where a negative high voltage is applied to the photocathode and the anode is grounded. The signal is taken directly from the anode. Figure 2.6b shows the scheme where the photocathode is grounded and a positive high voltage is applied to the anode. The signal is taken from the anode through a decoupling capacitor. The capacitors at the last few stages of the dynodes stabilize the dynode voltages. They provide the current to the dynodes during peak current pulses, and maintain the inter-stage potentials.

The anode ground scheme has a disadvantage in that charge leakage through the glass envelope to the cathode, which is at a high negative potential, can increase

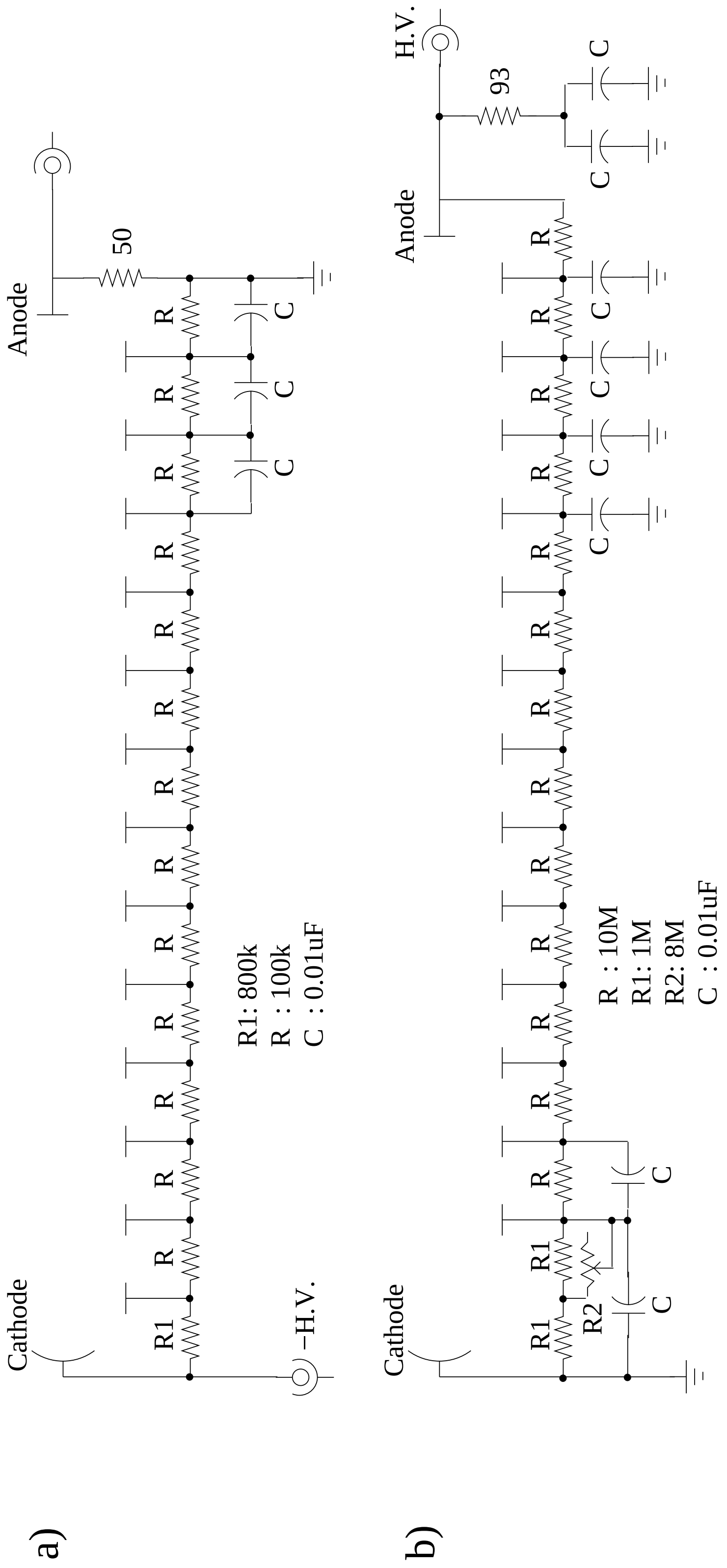

Figure 2.6: Voltage dividers used with the R1449 PMT. Shown are the anode ground scheme (a), and the cathode ground scheme (b). In the latter case, the signal is picked off further along the power line through a decoupling capacitor.

the noise rate of the PMT considerably. A metal shield [Ha85] around the PMT held at the same potential as the photocathode will eliminate this problem if it can be implemented without interfering with the light collection or becoming a safety hazard to operators.

2.1.6 The Overall Timing Performance

From the brief description of the basic parts of a PMT, it is possible to determine the effects of the processes (*i.e.* the emission and flight of the electrons) on the timing performance. Since photoemission and secondary emission both occur in less than 0.1 nsec, their direct contribution to the transit time and transit time spread is negligible. Indirectly, however, these processes are important in that they determine the initial energy and angular distribution of the emitted electrons. Thus, the transit time spread is due to the fluctuations in the flight times of the emitted electrons, resulting from variations in their initial positions and velocities. In general, most of the transit time and transit time spread is due to the secondary electrons in the multiplier [Le75]. However, in large PMT's the photoelectron flight time spread can become as large as the spread through the multiplier.

2.2 Timing Techniques

For the SNO project, it is important to accurately determine the time at which the Čerenkov photon strikes the photocathode of a triggered PMT. To accomplish this, a timing unit is used which produces a logic pulse at some fixed time with respect to the time of occurrence of the PMT pulse. There are various types of timing units, and the rest of the chapter will be devoted to describing the operation of a few kinds along with their advantages or disadvantages for use.

2.2.1 Leading Edge Timing

This is the simplest of the timing techniques, where the logic pulse is produced when the leading edge of the signal from the PMT reaches a pre-fixed voltage level. Figure 2.7 shows a simplified block diagram of a circuit that could be used for leading edge timing. The circuit is inexpensive and compact, which becomes an important consideration when thousands of these units will be needed. Also, for input pulses of constant shape and amplitude, the timing jitter of this unit is low compared to other types. However, the triggering time will depend on the size and rise time of the input pulse (time slewing). Figure 2.8a shows the rise time walk caused by pulses with different rise times. Figure 2.8b shows the trigger walk due to variations in pulse amplitude. Because of the different slopes of the pulses, they cross the discriminator level at different times. Both types of trigger walk introduce a spread into the measured appearance time of the pulse from the PMT, and thus degrade the timing resolution of the system.

It is fortunate that, in general, the shape of the output pulse from a PMT is uniform, so that rise time walk is not important in most cases. However, where the dynamic range of the output pulses is great, the amplitude walk can be as large as the rise time. Since pulse rise times are on the order of nanoseconds, this could degrade the timing resolution enough to reduce the accuracy of the vertex reconstruction. In such cases, a timing unit that minimizes amplitude walk is required.

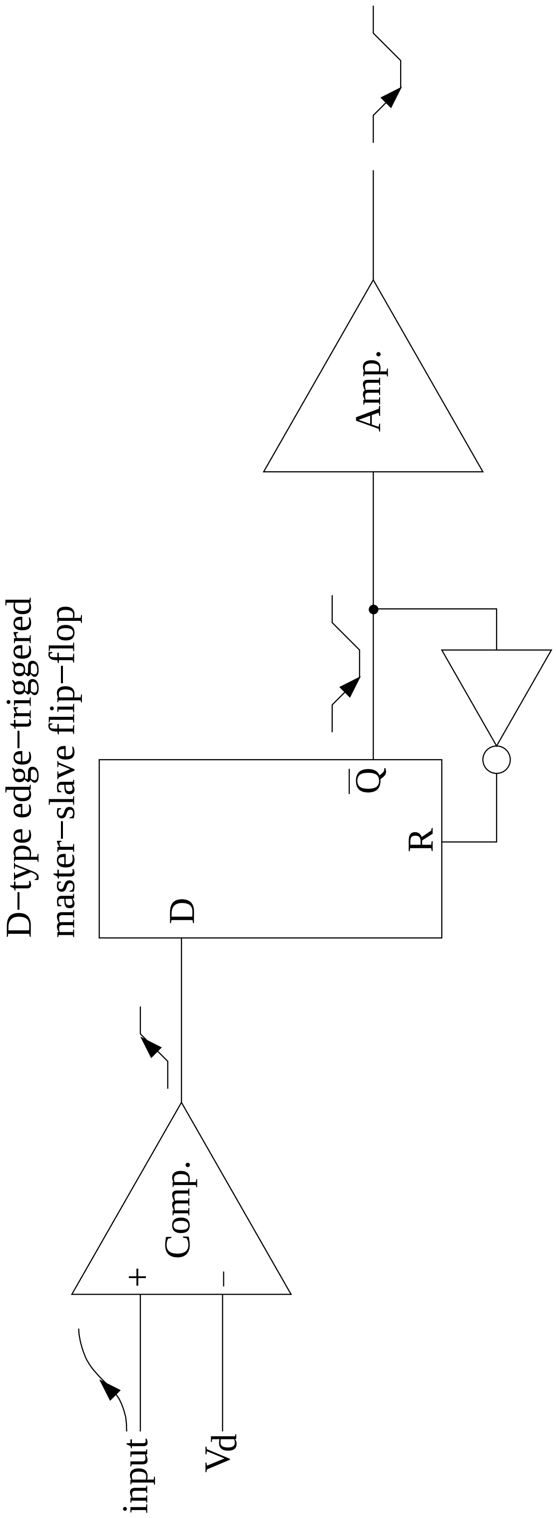

Figure 2.7: Block diagram of a circuit for a leading edge discriminator. When the input signal exceeds the discriminator voltage V_d, the output of the comparator goes high and triggers the production of a fast negative pulse by the D-type edge-triggered master-slave flip-flop.

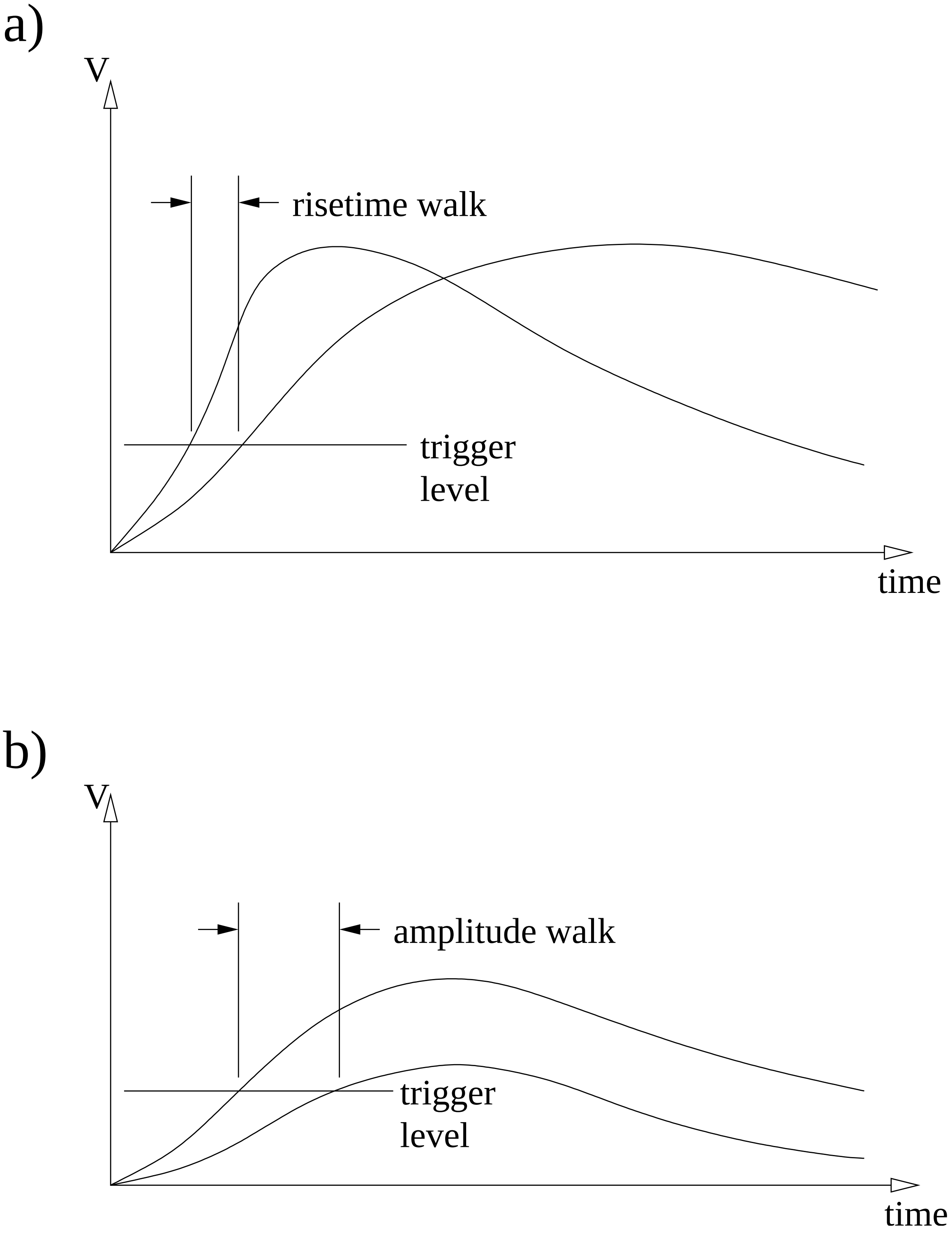

Figure 2.8: Trigger time walk in leading edge timing due to variations in pulse rise time (a) and pulse amplitude (b).

2.2.2 Constant Fraction Timing

The constant fraction timing technique is designed to eliminate amplitude walk for input pulses of the same shape. Figure 2.9 shows a simplified block diagram of a typical circuit used in constant fraction discriminators. The input signal is first split into two branches: one to the leading edge comparator and one to the constant fraction comparator. The signal to the constant fraction comparator is further split into two branches, where in one branch it is attenuated and in the other delayed. These two signals are then compared, and when they are equal, the comparator triggers the production of the output logic pulse. The leading edge comparator and AND-gate are used to ensure that the output is generated by a true signal, not on random triggerings of the constant fraction comparator due to noise.

The principles of constant fraction timing are discussed in reference [Po79], so only brief description will be given here. Since the shape of each input pulse is constant, each pulse can be expressed as

$$
\begin{aligned}
A(t) &= A_0 \cdot f(t) \\
\text{where} \quad A_0 &= \text{amplitude of pulse} \\
f(t) &= \text{a function describing the shape of a pulse} \\
& \ \text{with an amplitude of one unit}
\end{aligned}
$$

The attenuated signal to the constant fraction comparator can be expressed as $xA(t)$, where x is a factor which is less than one. The delayed signal can be expressed as $A(t-\tau)$, where τ is the delay time. The time t' at which these two signals are equal

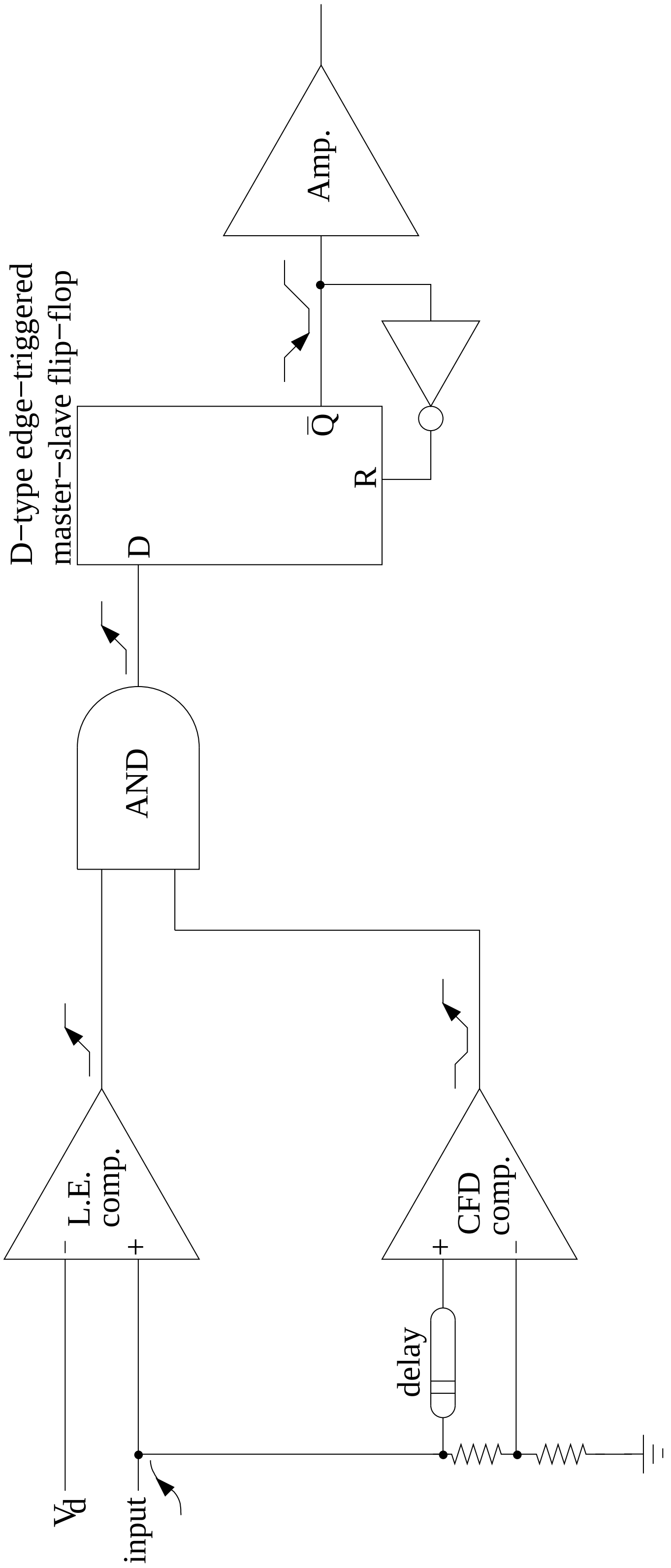

Figure 2.9: Block diagram of a circuit for a constant fraction discriminator. Its operation is explained in the text.

is given by:

$$\begin{aligned} A(t'-\tau) &= xA(t') \\ \text{or} \qquad f(t'-\tau) &= xf(t') \end{aligned}$$

Here, t' does not depend on the amplitude A_0 of the input pulse. It only depends on τ and x (both of which are fixed by the discriminator circuit) and on $f(t)$. If $f(t)$ is the same for all pulses, then the trigger time of the comparator will be constant with respect to the start of the pulses.

There will always be differences in the shapes of pulses from a PMT, so that amplitude walk can never truly be eliminated. However, the timing performance of a constant fraction discriminator (CFD) will be better than that of a leading edge (LE) discriminator when the dynamic range of the input pulses is large. One disadvantage of the CFD technique is that the circuit is more complicated than that for the LE discriminator, and thus more difficult and expensive to build. Also, the input pulse is delayed in one branch by passing it through a long length of coaxial cable (roughly one foot of cable is needed for each nanosecond of delay), and this means that the physical size of each unit will be greatly increased over that of the LE discriminator. In addition, the trigger efficiency of the CFD is not 100% as in the case of the LE discriminator, as the signals to the AND-gate from the two comparators may not always be in coincidence.

2.2.3 Leading Edge Amplitude Compensated Timing

It is possible to correct for the amplitude walk in LE timing, not with a more complicated timing unit such as the CFD, but with the amplitude information. For pulses of the same shape, the triggering time of a LE discriminator is a well-defined function of pulse amplitude. By measuring the amplitude of each pulse, the trigger time offset can be calculated by computer, and the trigger time corrected by this amount to determine the "true" appearance time of the pulse. This technique is known as leading edge amplitude compensated (LEAC) timing.

For example, figure 2.10 shows that for pulses with linear rising edges and a constant rise time the trigger offset is inversely proportional to the amplitude of the pulses, that is:

$$t_d = \frac{V_d t_0}{A}$$

where t_d = trigger time offset

V_d = discriminator level (Volts)

A = pulse amplitude (Volts)

t_0 = time to reach max. voltage

The true appearance time would then be equal to the trigger time minus the offset time t_d.

In general, true PMT pulse shapes are too complicated to be expressed as a simple function of time, so the trigger time offset as a function of amplitude has to be found empirically. The procedure for this is difficult (it is discussed in Chapter 4) and any error introduced in these measurements will translate into a poorer timing resolution for the PMT/electronics system.

Which of the three timing units is the best for SNO depends on a) the timing resolution needed to accurately reconstruct the neutrino's interaction location, b) the

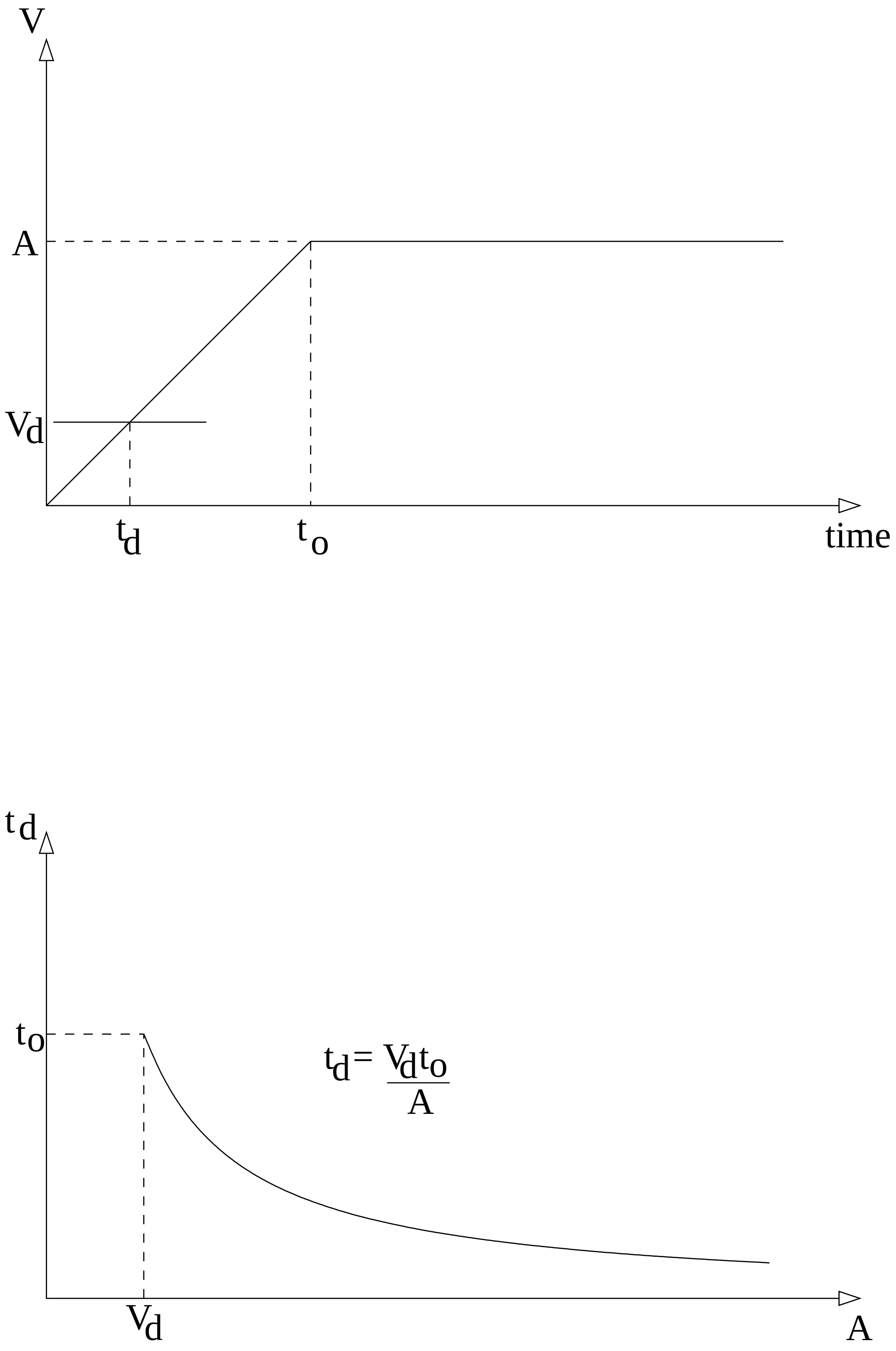

Figure 2.10: The leading edge trigger time offset t_d for pulses with linear rising edges, where V_d is the discriminator level, A is the pulse amplitude and t_0 is the time for the pulse to reach its maximum voltage.

pulse shapes from the particular PMT used in the project, and c) the cost of each unit.

Chapter 3

Apparatus

To characterize the Hamamatsu R1449 PMT, measurements of the TTS, dark noise rate and single photoelectron response were performed. Included in the measurements were tests of the various timing discriminators and voltage divider schemes to determine which would be the most suitable for the SNO project. Before describing the techniques and electronics used in the measurements, a description of the basic parts common to all of the experimental set-ups will be given. These include the PMT's, a light pulser and a light-tight box housing the 20″ PMT.

3.1 The Hamamatsu R1449 PMT

This PMT was designed specifically for the large underground Čerenkov detector built at Kamioka, Japan for proton decay studies. The design of this detector is similar to that of the SNO detector, except that it was used to search for decaying protons in light water. However, the basic requirements for the PMT's are the same for both projects; that is, they must have a large photosensitive area, good timing properties, be able to detect single photoelectrons, withstand high pressures underwater, and must remain stable over a period of years.

Figure 3.1 shows the Hamamatsu R1449 20″ PMT. The envelope is made of borosilicate glass HARIO-32, which is water-durable and has a short wavelength cutoff at about 300 nm (subsequent information on this PMT is from reference [Ku83]). The photocathode window is hemispherical in shape for structural strength and to reduce flight time differences between the photocathode and the first dynode. The photocathode is made of a bialkali material. Figure 3.2 shows the measured quantum efficiency of the R1449 PMT and the Čerenkov light spectrum after passing through 15 m of water. The electron multiplier is a 13-stage venetian blind type (see figure 3.3). An advantage of this type of dynode structure is that a large photoelectron collection area can be produced for high collection efficiencies. The first dynode in the R1449 PMT is three inches in diameter. Also, the inter-stage collection efficiency for secondary electrons is high for venetian blind dynodes, and this results in an improved gain over other designs. The gain of the multiplier in the R1449 PMT is about 10^7 for an operating voltage of 2000V, which makes it suitable for single photoelectron detection. The disadvantage of the venetian blind design is that the electric field at the dynode surfaces is low, which means a slower time response and greater time spread over other designs.

3.2 The RCA 8850 PMT

This PMT was used to test the experimental set-ups for the 20″ PMT. It is a 2″ diameter photocathode transmission-type PMT with good single photoelectron resolution often used in timing measurements. The window is made of pyrex glass (with a short wavelength cutoff at about 280 nm), and the photocathode material is K_2CsSb (a

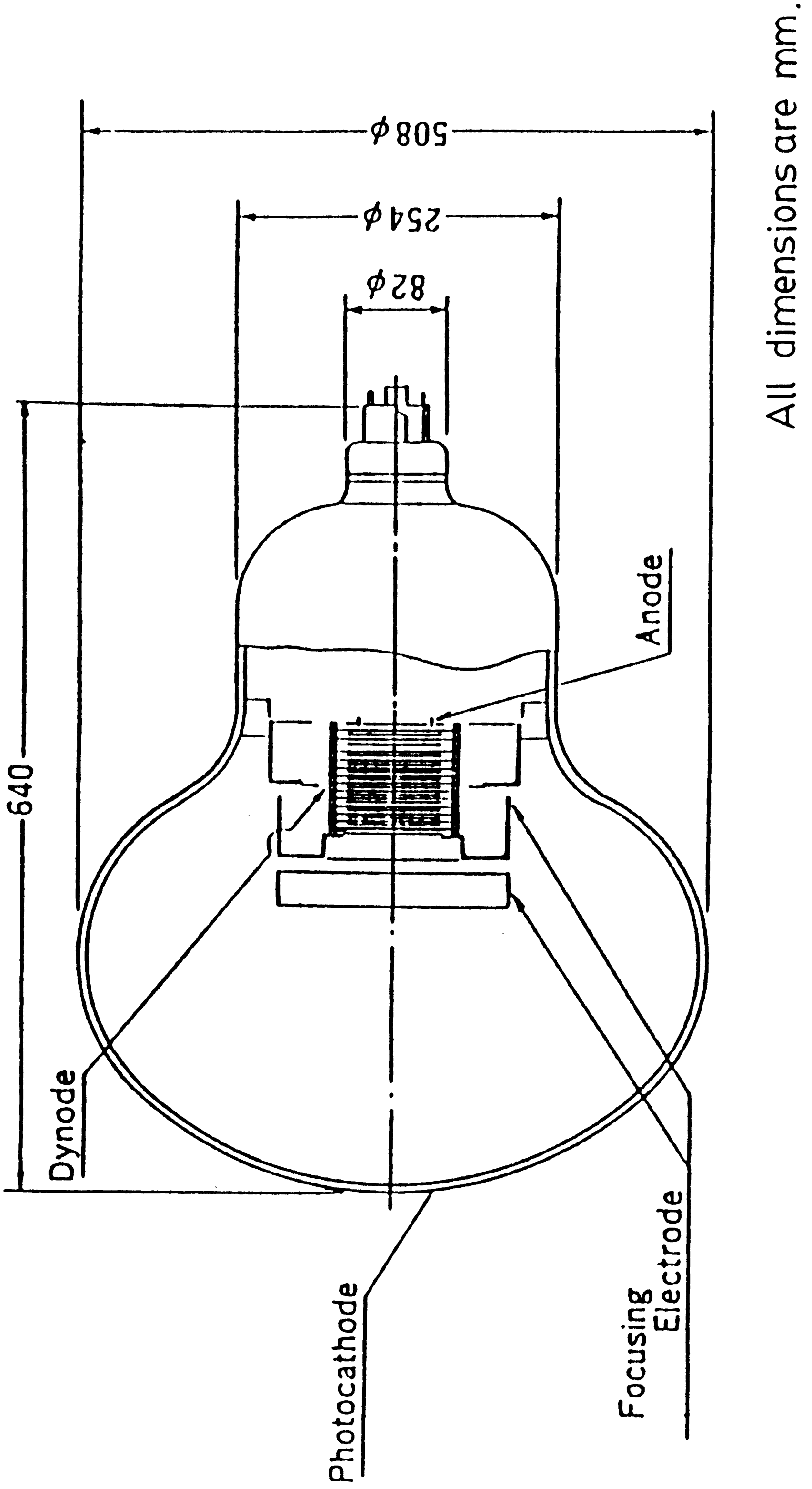

Figure 3.1: Construction of the Hamamatsu R1449 PMT (fig. 2 from [Ku83]).

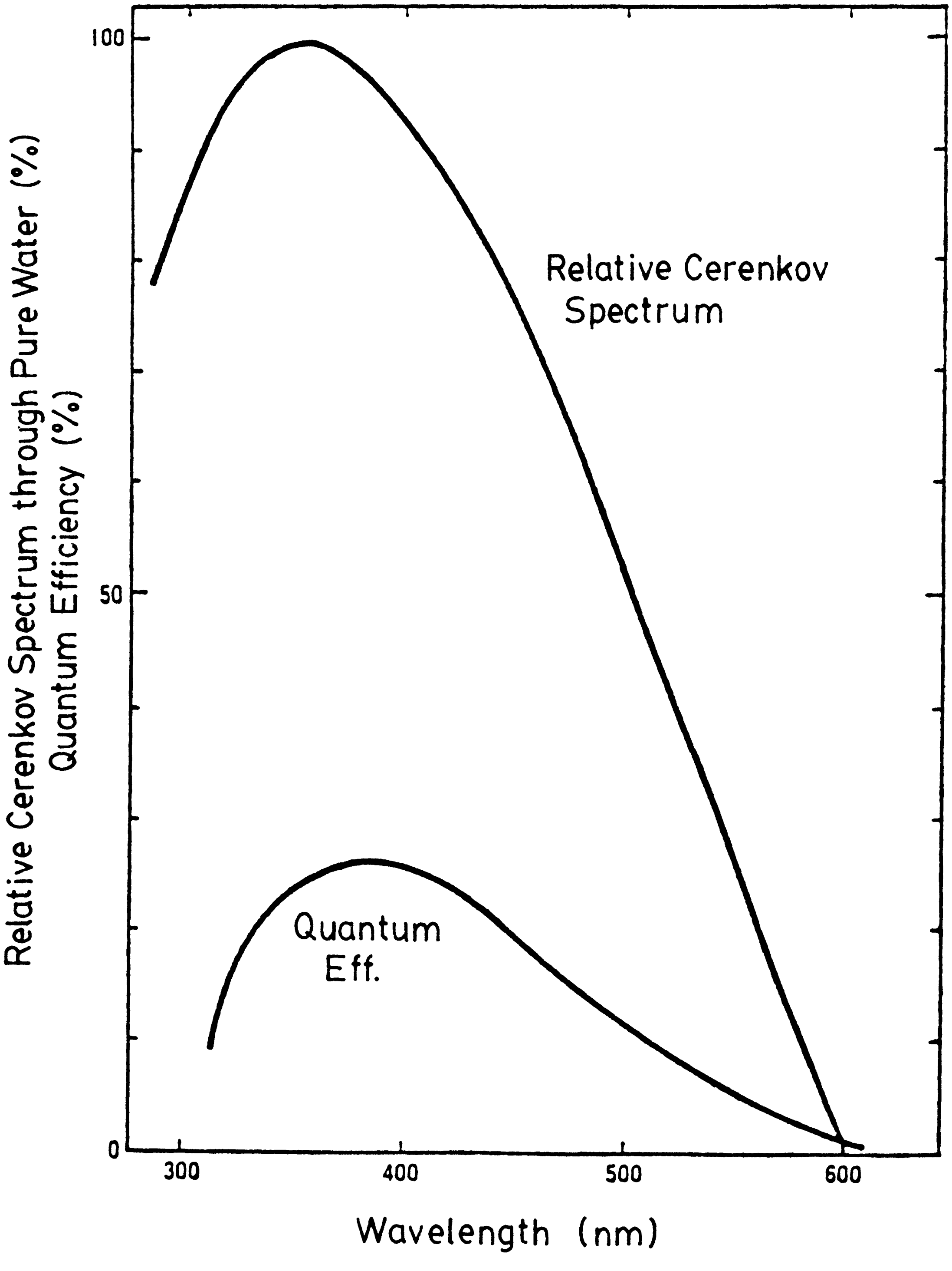

Figure 3.2: The spectral distribution of Čerenkov light after passing through 15 m of water and the quantum efficiency of the Hamamatsu R1449 PMT (fig. 3 from [Ku83]).

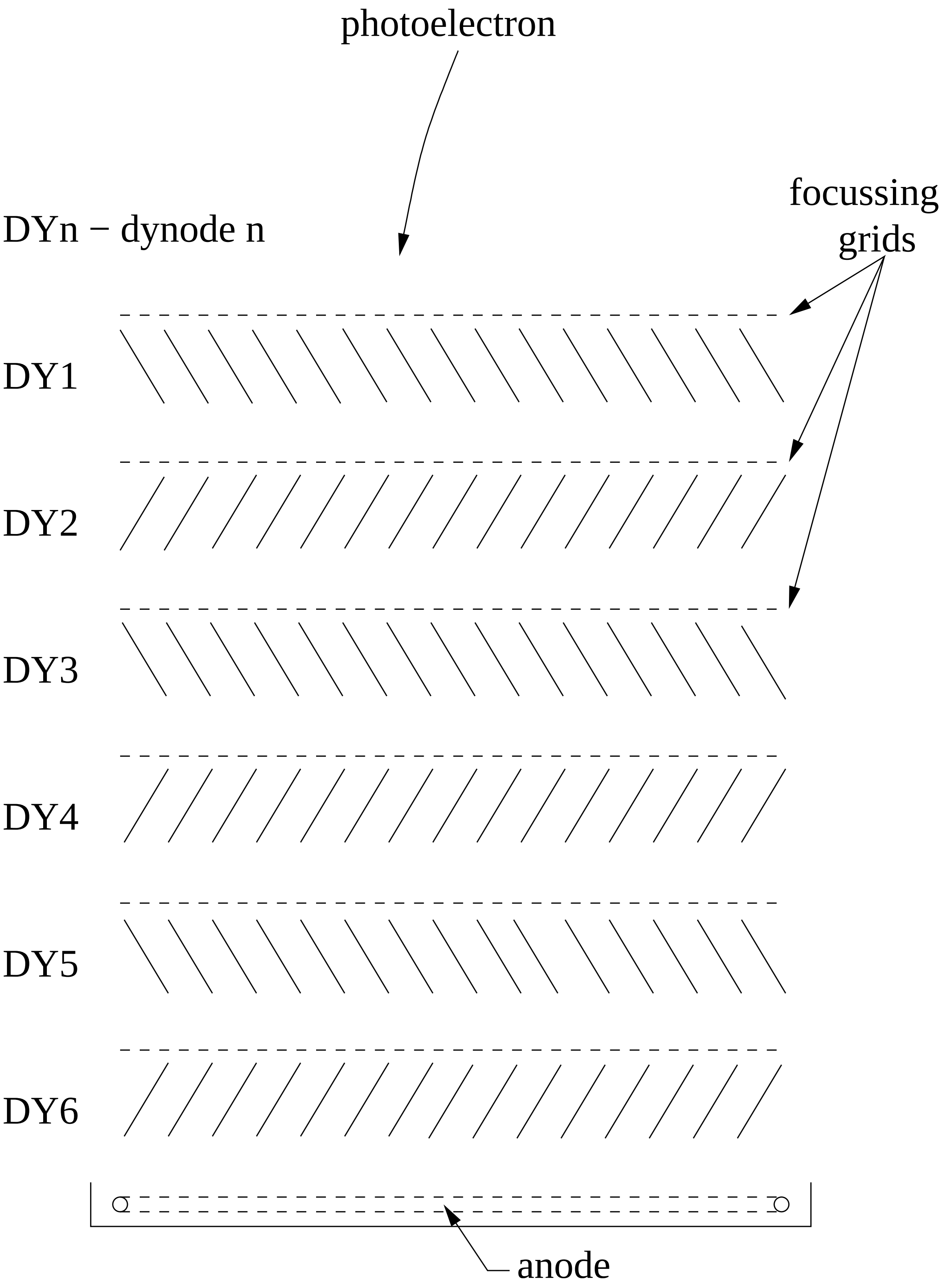

Figure 3.3: Schematic diagram of a venetian blind dynode structure.

bialkali), so its spectral response should be similar to that of the R1449 PMT. The multiplier has a 12-stage in-line dynode structure for good timing properties. The transit time spread for this PMT as given in the RCA Handbook [Rc80] is 0.59 nsec for emission from the centre of the photocathode, and 0.64 nsec for emission from the whole photocathode.

3.3 The Light Pulser

To accurately measure the TTS of the PMT, a light pulse is needed whose width is much less than the TTS (7.0 nsec as measured by Hamamatsu [Ku83]). The light pulser must also produce a fast electrical pulse at some fixed time with respect to the light pulse for triggering the measurement electronics. The method that was chosen for producing the short pulses used avalanche-mode transistor circuits to produce a fast electrical pulse which, when applied to a suitable LED, generated the short light pulse needed. This method is well understood [Mi65], and has often been used in previous tests on PMT's [An74, Gr78, Fr79, Be85]. Figure 3.4a shows a basic avalanche transistor delay line pulse generator, and figure 3.4b shows the I-V characteristic of an avalanche-mode transistor. The load line is chosen so that there is always a very low current through the transistor, and thus always some charge stored in the base region. The charge line (characteristic impedance R_0) is charged to a voltage V_{cc} which is slightly less than the breakdown voltage BV_{cer}. When a signal is applied to the base, the transistor breaks down and the collector voltage drops to LV_{cer}; because there was charge stored in the base region prior to breakdown, the turn-on time of the transistor is very short (∼1 nsec). Thus, there is a negative voltage step

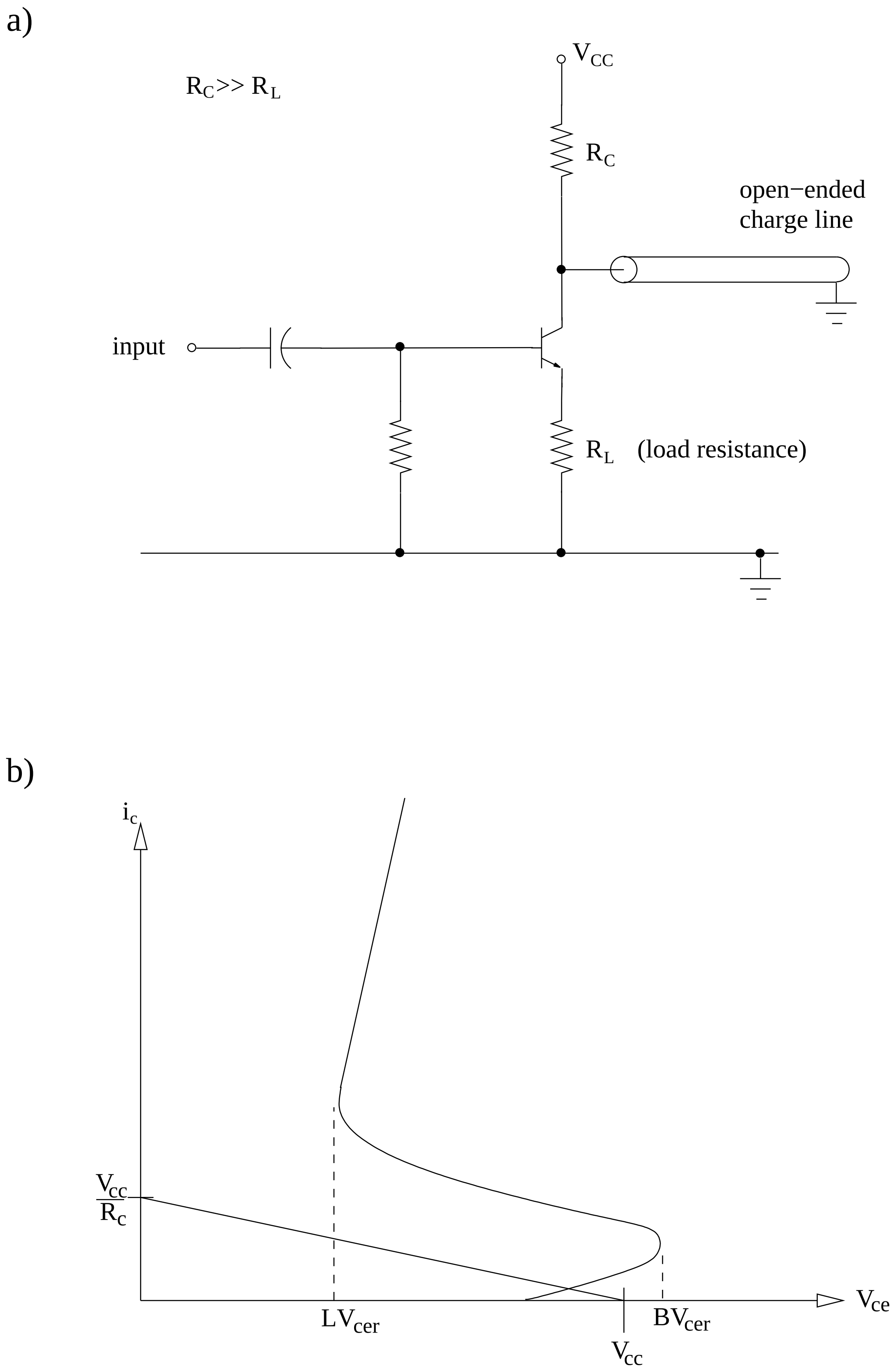

Figure 3.4: Circuit of a basic avalanche transistor delay line pulse generator (a), and the I-V characteristic of an avalanche-mode transistor (b).

$\Delta V = LV_{cer} - V_{cc}$ applied to the charge line through the resistor R_L, producing a step current pulse

$$i(t = 0^+) = \Delta V/(R_L + R_0) = I$$

(define current flow into the charge line as positive). At time $t = \tau_d$, the current step reaches the open end of the charge line, and is reflected back inverted. At time $t = 2\tau_d^+$, this reflected step reaches the start of the charge line, where the net current becomes

$$i(t = 2\tau_d^+) = I + (-I) + (-I)\rho$$

where ρ is the reflection coefficient for current in a transmission line. In this case, the reflection coefficient is expressed as

$$\rho = (R_0 - R_L)/(R_0 + R_L)$$

and so

$$i(t = 2\tau_d^+) = -I\rho = \Delta V(R_L - R_0)/(R_L + R_0)^2$$

By choosing $R_L \leq R_0$, this would make $i(2\tau_d^+) \geq 0$ (since $\Delta V < 0$).

Thus, at time $t = 0^+$, the transistor breaks down and a current of $(V_{cc} - LV_{cer})/(R_L + R_0)$ flows out of the charge line and through the transistor. At time $t = 2\tau_d^+$, for $R_L \leq R_0$, the current reverses and immediately turns the transistor off. The result is a current pulse through R_L that lasts for time $2\tau_d$.

Figure 3.5 shows the circuit for the light pulse generator that was constructed for the measurements at Queen's University. It consists of three of the basic avalanche-mode transistor circuits. The first is triggered by an external pulse, providing a very

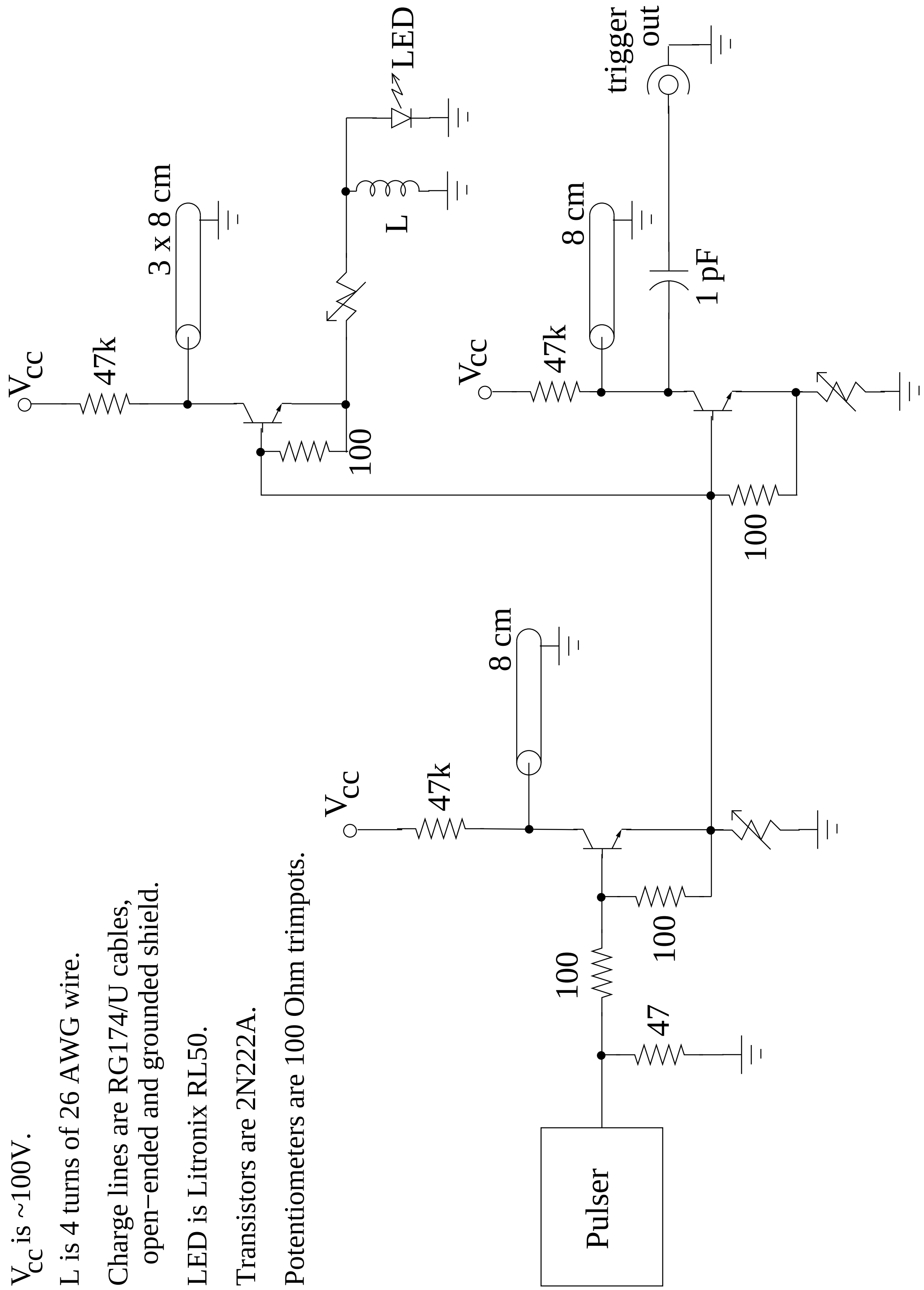

V_{cc} is ~100V.

L is 4 turns of 26 AWG wire.

Charge lines are RG174/U cables, open−ended and grounded shield.

LED is Litronix RL50.

Transistors are 2N222A.

Potentiometers are 100 Ohm trimpots.

Figure 3.5: Circuit of the light pulse generator constructed at Queen's University for testing the Hamamatsu R1449 PMT.

sharp trigger pulse to the two following parts of the circuit. The second part drives the LED, and the third provides a negative pulse for timing purposes. The charge lines were 8 cm long each, so that

$$\begin{aligned} 2\tau_d &= 2L/(c\beta) = 2(8\text{ cm})/(30\text{ cm/nsec} \times 0.66) \\ &= 0.8\text{ nsec} \end{aligned}$$

where $c\beta$ is the pulse propagation speed in the charge line. However, due to finite turn-on and turn-off times, the width of the pulse was about 1.9 nsec (see section **??**).

Various fast LED's were tried in the light pulse generator, but only one, a Litronix RL-50 red LED, was found that yielded a light pulse width ≤ 2 nsec. It was found that the response times of LED's increase with the frequency of the light emitted, and that LED's that emit light of higher frequencies tend to fluoresce and add long tails to the pulses. Hence, the PMT's were tested with red light only ($\lambda \approx 650$ nm). This is unfortunate in that there is no way of determining how the TTS of the PMT depended on the energy of the incoming photons. The higher energy Čerenkov photons could increase the spread in the photoelectron flight times significantly over that for the red light. Also, the red light falls just within the tail-end of the spectral response of the 20″ PMT (see figure 3.2), so that the detection efficiency for the light pulses is low. This was advantageous in that single photoelectron pulses were obtained without having to attenuate the light pulses. However, the detection efficiency is sensitive to photocathode impurities for light at the tail of the response curve [Na70], so that using red light resulted in changes in the efficiency that would not be seen for higher frequency light.

3.4 Shielding the R1449 PMT

All PMT's require shielding from background light. As well as increasing the noise rate during measurements, the background light could easily increase the current down the multiplier enough to burn out the last few dynode stages. A large wooden and aluminum light-tight enclosure was built to shield the PMT (see figure 3.6). Light pulses were transmitted through a constant length of fibre-optic cable to points on the photocathode surface. The fibre-optic cable was fed into the enclosure through a length of copper tubing that was mounted normal to the top of the box. The cable was kept in contact with the PMT surface, illuminating only a very small point on the photocathode. The mounting could be slid along one side of the rounded top surface so that the fibre-optic could be moved over the surface of the PMT, and held nearly normal to it to reduce reflection of the light from the glass surface. There were holes (roughly $2''$ and $1''$ diameter) in the top of the box that could be opened to check the position of the fibre-optic cable end. The whole enclosure was draped in black cloth, and the room was darkened whenever the bias was applied to the PMT.

Besides being sensitive to light, the large dynode structure of the PMT acts as an antenna in the RF range. To reduce the noise which would be picked up, the PMT was moved to a room on the first floor of the building away from computers or other sources of RF noise. The light pulse generator was housed in a metal box and was operated in a separate room from that with the PMT. Once these precautions were taken, the spurious firing of the CFD caused by electrical noise pick-up was eliminated.

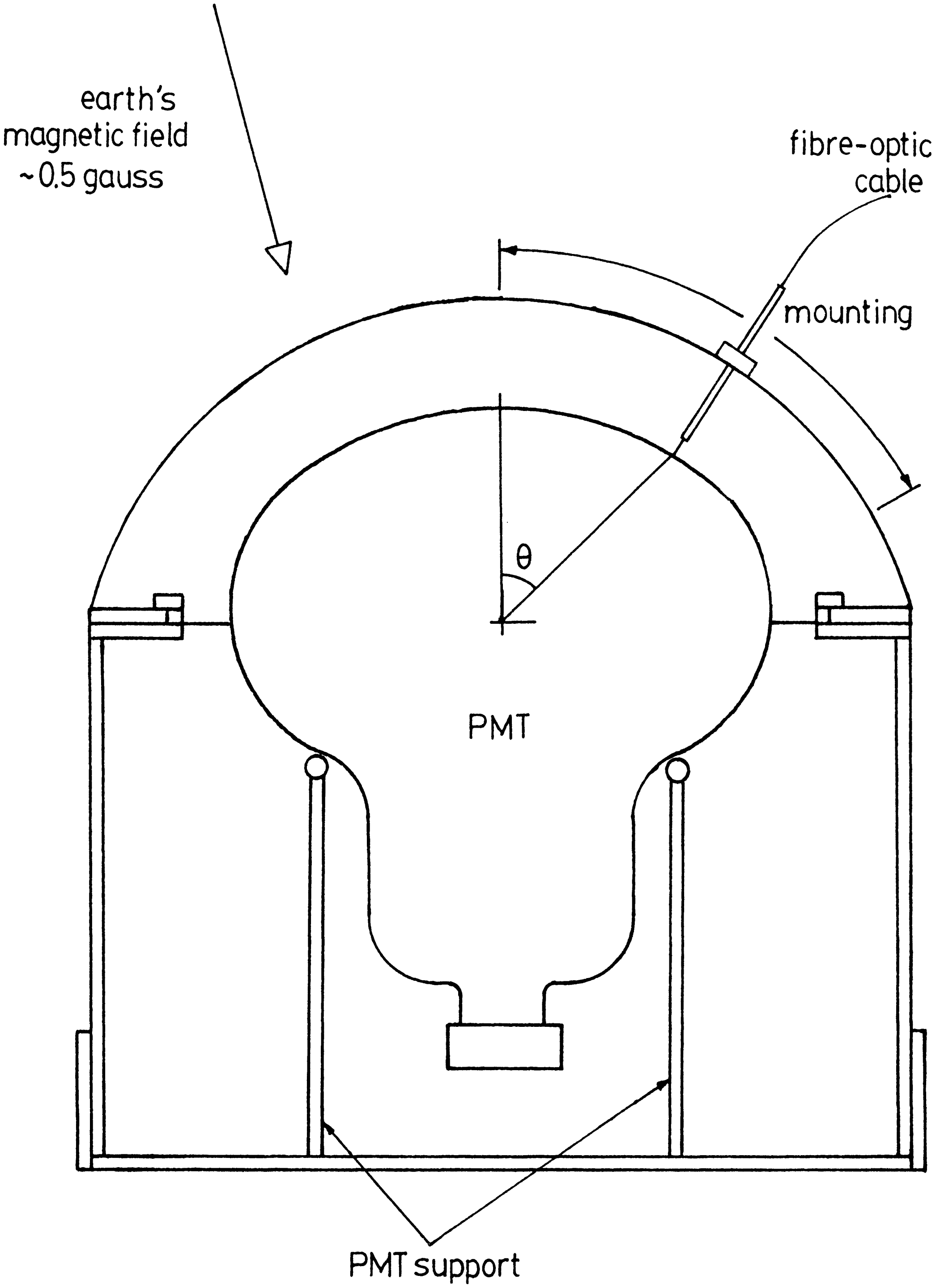

Figure 3.6: Construction of the light-tight enclosure housing the Hamamatsu R1449 PMT. The fibre-optic cable carrying the light pulse is held normal to the curved top of the box by the mounting, and can be moved along the PMT surface. Also shown are the strength and direction of the earth's magnetic field, and the angle θ defining the position on the PMT's surface at which the light is shone.

Due to the long flight paths of the photoelectrons and the weak electric fields, the 20″ PMT's are very sensitive to magnetic fields. Depending on the orientation of the earth's magnetic field with respect to the PMT, its photoelectron collection efficiency could drop by as much as 35%. To reduce the magnetic field strength, a μ-metal (high magnetic permeability) shield or compensation coil can be placed around the PMT. However, the PMT was not shielded from the earth's magnetic field during the measurements. The effects of this will be discussed in the next chapter.

3.5 The Measurement Electronics

The techniques for single photon detection and timing with PMT's have been in use for decades and are discussed in many references [Po72, Hu80, Da85]. Thus, only a brief description of the techniques used will be given here. There were three basic set-ups which will be described in the order that they were used. It should be noted that the timing measurements were performed on the PMT/electronics system as a whole. Hence, different set-ups were often used to measure the same quantity in an effort to determine the effects of the electronics on each result.

3.5.1 Timing Properties over the Photocathode

Figure 3.7 shows a block diagram of the electronics used to measure the light pulse width, and the single photoelectron pulse height spectrum and timing resolution of the 20″ PMT as a function of the position on the photocathode at which the photoelectrons were generated. The light pulse generator, operated at 50kHz, simultaneously sent a light pulse to the PMT along the fibre-optic cable and a fast pulse to start the

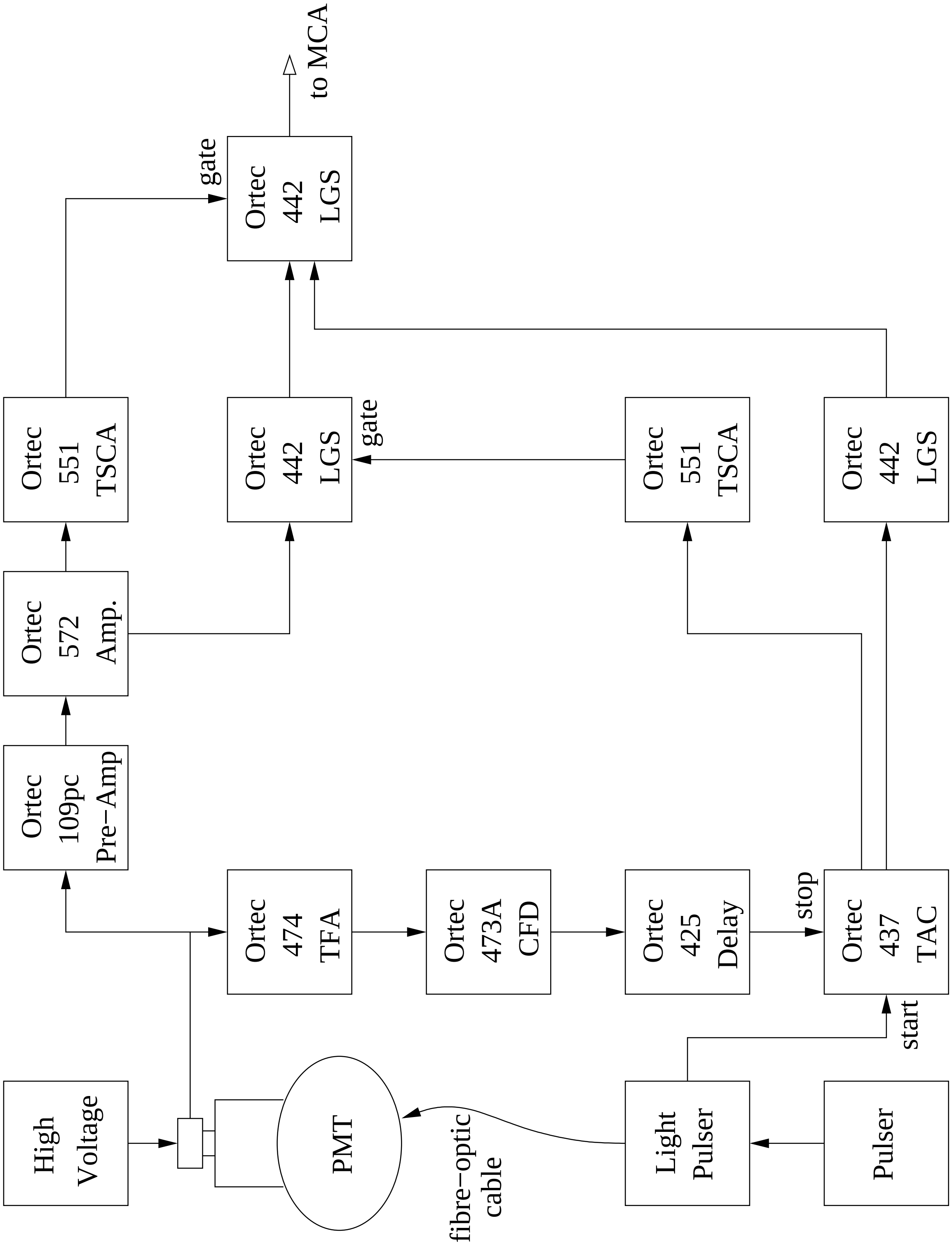

Figure 3.7: Block diagram of the electronics used to measure the light pulse width and the timing resolution over the photocathode of the R1449 PMT.

Ortec 437 Time-to-Amplitude Converter (TAC). The output pulse from the PMT was split into two cables and processed in the slow and fast circuits shown in the diagram. In the fast circuit, the pulse from the PMT was amplified in an Ortec 474 Timing Filter Amplifier (integration time of 10 nsec), and was fed into an Ortec 473A Constant Fraction Discriminator. The CFD produced a fast logic pulse which was delayed and used to stop the TAC. In the slow circuit, the pulse from the PMT was amplified by an Ortec 109PC Preamplifier and an Ortec 572 Amplifier. The slow linear signals were gated by logic signals from an Ortec 551 Timing Single Channel Analyzer (TSCA) set on the peak of the timing spectrum. This eliminated most of the counts in the pulse height spectrum not produced by the light pulse generator. The timing and linear signals to the multichannel analyzer (MCA) were also gated by a TSCA set on the slow linear signal. This was done to set the threshold of the measurement and to reduce the noise background.

The triggering rates of the CFD and both TSCA's were monitored. The rate at which the TSCA on the TAC pulses was triggered was the rate at which light pulses were detected (plus the dark count rate in the narrow time window). This rate was always less than 5% of the rate at which the light pulser was triggered, so it is unlikely that more than one photoelectron was generated per pulse (see section 4.1 for a detailed discussion of this). The discriminator level on the CFD was set lower than the level on the TSCA at the linear circuit, in order to ensure that the CFD was not rejecting pulses that would be accepted by the TSCA.

3.5.2 A Comparison of Timing Techniques

Figure 3.8 shows a block diagram of the electronics used in comparing the CFD and LEAC timing techniques. The first part of the system (starting from the PMT) is the same as that used in the earlier measurements; the gating system that follows is different. The width and delay of the output of each Ortec 472 Linear Gate and Stretcher (LGS) was adjusted so that the TAC signal was coincident with the linear signal when the PMT was triggered by a generated light pulse. The ADC's were gated so that they digitized only those TAC and linear signals that arrived in coincidence with each other. In this way, most of the PMT dark counts were excluded from the spectra. The pairs of digitized signals were then either immediately analyzed and sorted into two spectra, or were written to magtape in event-by-event mode by the PDP-15 computer. The data on magtape were later read back by the computer, and the TAC pulses were sorted into various timing spectra according to the amplitude of the corresponding linear pulses.

3.5.3 Double Constant Fraction Timing

The results from the measurements on the 20″ PMT using the previously described circuits indicated a measured TTS of about 10.4 nsec (see section 4.2), which is much larger than the anticipated value of 7 nsec [Ku83]. To determine whether the TTS of the PMT really was greater than 10 nsec, or if it had been significantly degraded by the measuring electronics, a Tektronix 466 100 MHz storage oscilloscope was used to visually examine single photoelectron pulses, and to measure the spot timing resolution of the PMT. A block diagram of the circuit is shown in figure 3.9.

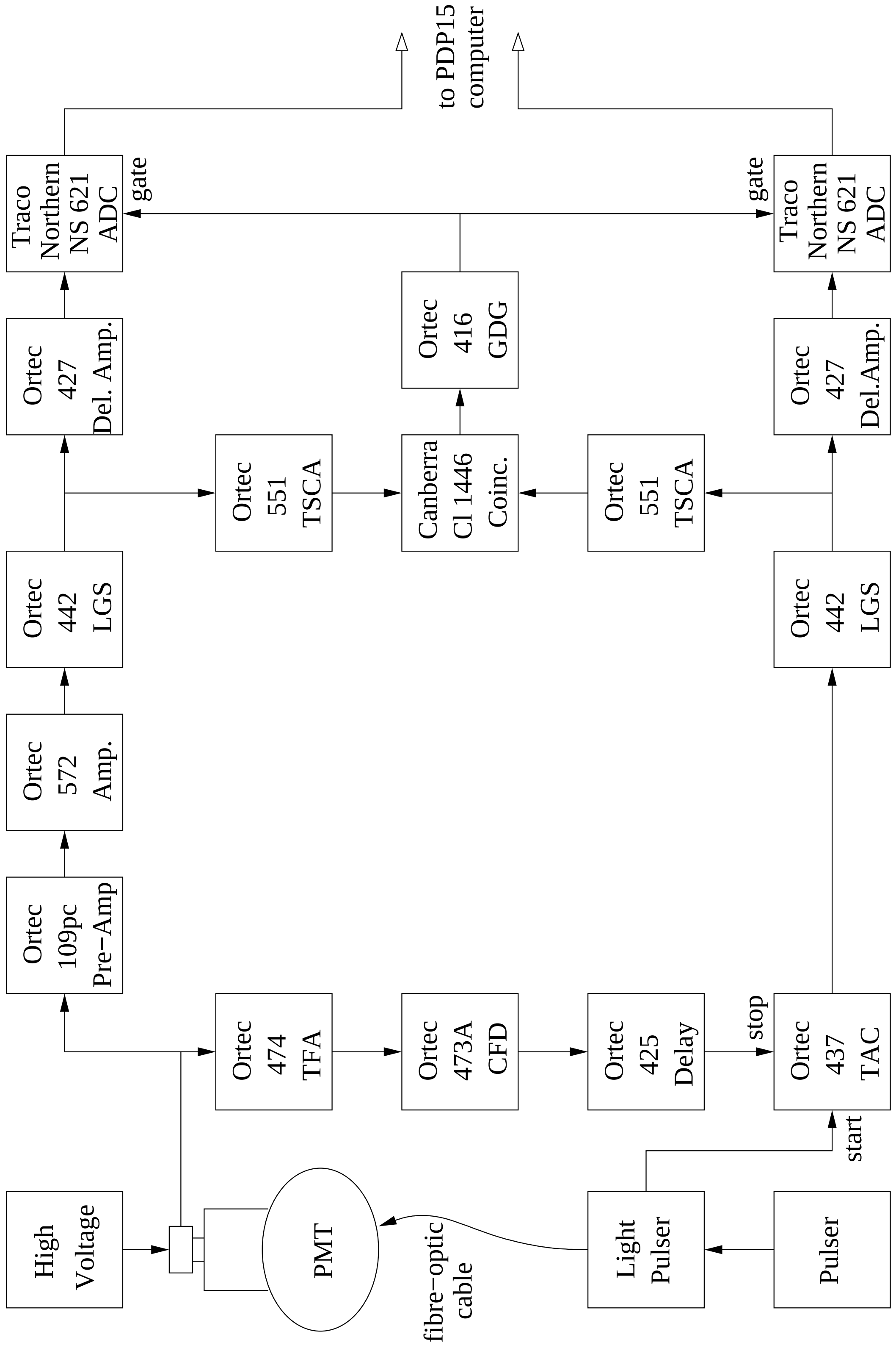

Figure 3.8: Block diagram of the electronics used to compare the CFD and LEAC timing techniques.

The light pulse generator simultaneously produced a light pulse and a fast logic pulse. The light pulse was directed onto the 20″ PMT via a fibre-optic cable. The output from the PMT was split into two branches. In one branch, it was amplified and fed into a CFD. The slow logic pulse from the CFD (width ∼500 nsec) was inverted and fed into the strobe input of the EG&G C126N Strobed Coincidence Unit. The fast logic pulse from the light pulse generator was delayed long enough to arrive at the coincidence unit about 20-30 nsec after the arrival of the strobe input signal from the CFD, to make sure that the two signals overlapped. The output from the coincidence unit was used to trigger the oscilloscope. The signal from the PMT was delayed long enough to ensure that it arrived at the oscilloscope after the external trigger pulse.

With the storage oscilloscope, individual pulses from the PMT were stored and viewed for up to a few minutes. The oscilloscope was triggered by pulses from the light pulse generator only when the PMT pulse amplitude exceeded the level set by the discriminator on the CFD. In this way, almost all of the pulses viewed were single photoelectron pulses, and variations in the arrival time of these pulses with respect to the trigger pulse were a measure of the TTS of the PMT.

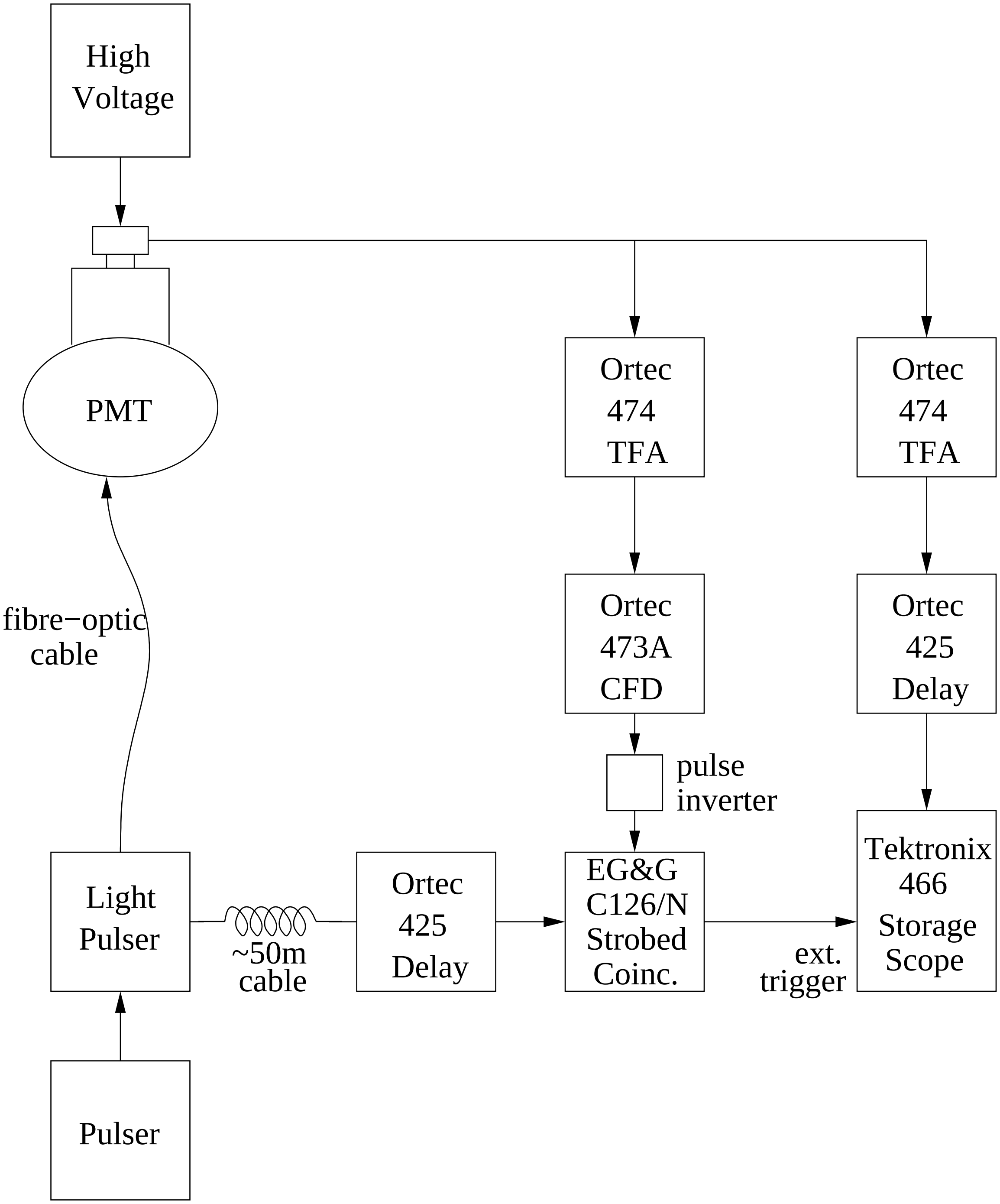

Figure 3.9: Block diagram of the electronics used to visually examine single photoelectron pulses from the R1449 PMT, and to measure the spot timing resolution using double constant fraction timing.

Chapter 4

Procedure and Results

4.1 Measuring the Light Pulse Width

To measure the light pulse width produced by the avalanche-mode pulser (see figure 3.5), the RCA 8850 PMT was used with the electronics described in section 3.5.1. Figure 4.1 shows a typical pulse from the 8850 PMT before and after amplification by the Ortec 474 TFA. The pulse from the TFA had a risetime of ∼7 nsec and a fwhm of ∼8 nsec. The light pulser was operated at 50 kHz, and the fibre-optic was positioned at the centre of the photocathode.

With the fibre-optic cable decoupled from the LED, but with the pulser still operating, two noise spectra were collected. Figure 4.2a shows the ungated pulse height distribution. The count rate was 985±5 counts/sec. When both LGS units were gated, the count rate was 0.92±0.01 counts/sec, indicating that the gating system was effective in reducing the noise. The noise appears to be at the single photoelectron level, as expected [Da85]. With the fibre-optic cable re-coupled to the LED, ungated and gated pulse height distributions were collected. The count rates were 1160±5 and 189.1±0.4 counts/sec for the ungated and gated spectra, respectively.

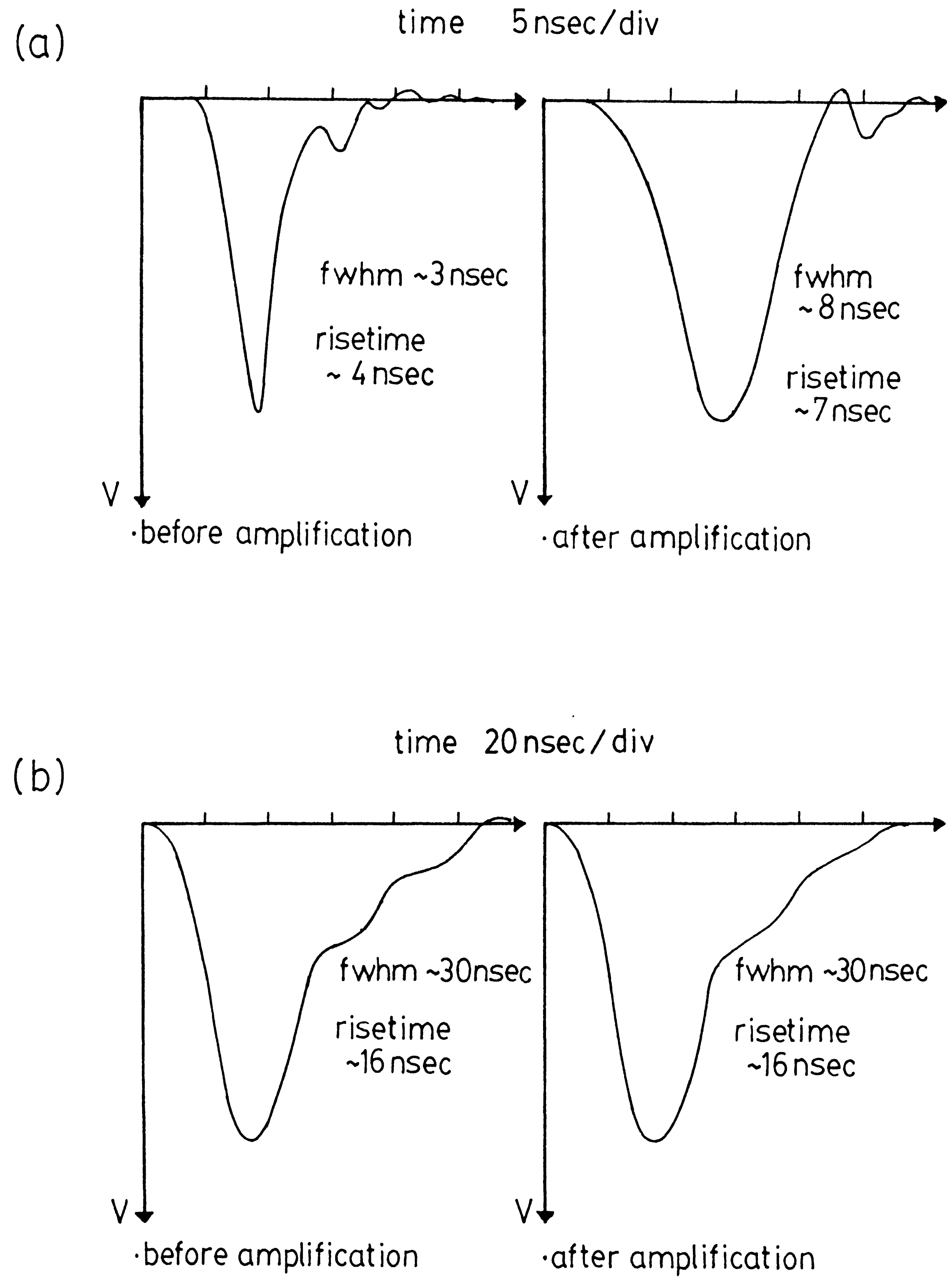

Figure 4.1: Typical pulses before and after amplification by the Ortec 474 TFA (integration time ~10 nsec) from the RCA 8850 PMT (a) and the Hamamatsu R1449 PMT #ZW4706 (b).

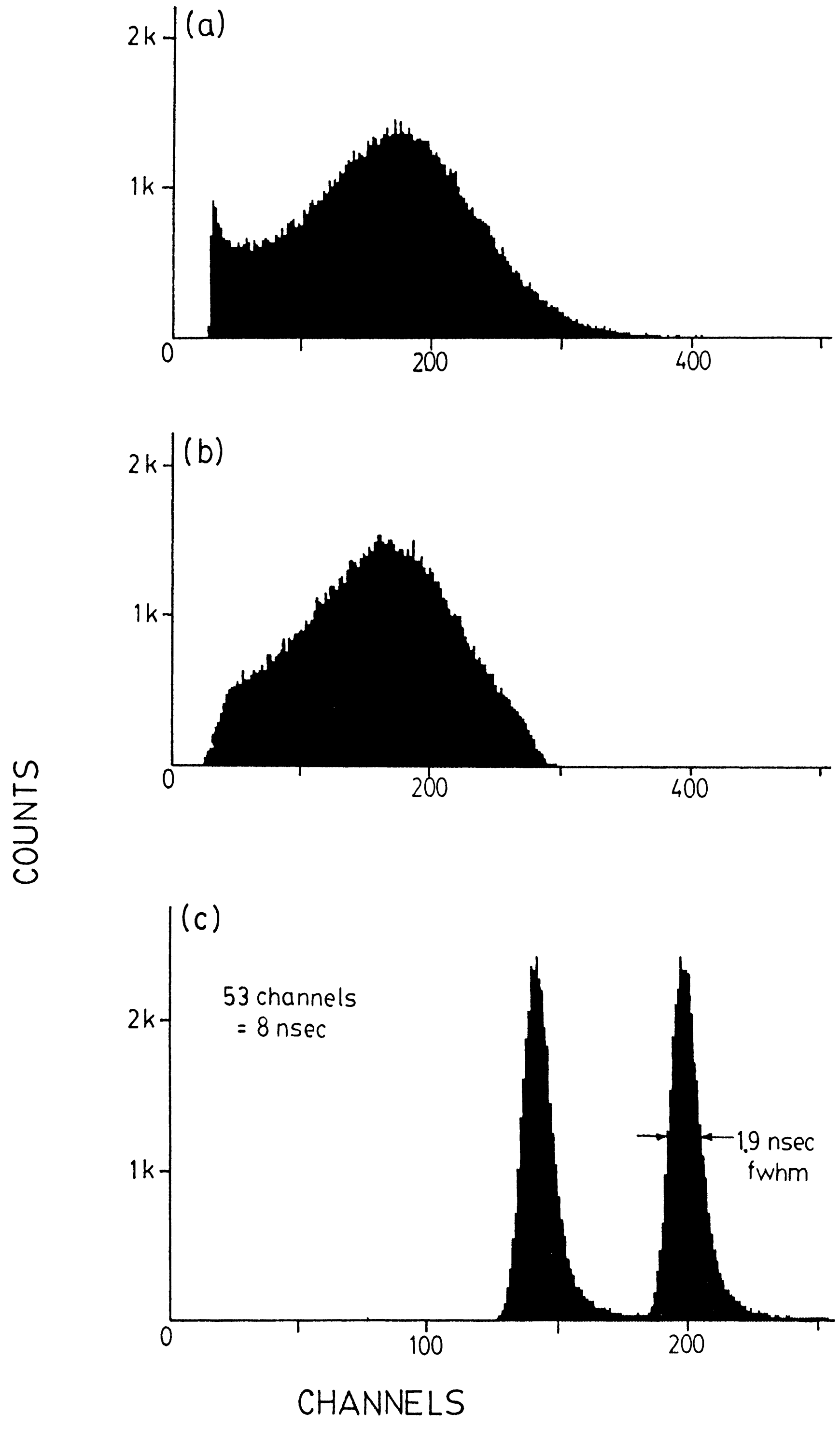

Figure 4.2: The noise pulse height spectrum (a), the single photoelectron pulse height spectrum (b), and part of the single photoelectron timing spectrum for the RCA 8850 PMT (c). The two peaks in the timing spectrum were produced by delaying the stop pulse to the TAC by 8 nsec for half of the collection time, and were used to calibrate the spectrum.

The single peak in the gated spectrum (see figure 4.2b) at the same position as the noise peak indicates that the light generated pulses were on the single photoelectron level. Another indication of this is that only 0.38% of the light pulses were generating pulses from the PMT. If it is assumed that the number of photoelectrons produced per light pulse follows a Poisson distribution [Rc80]:

$$P(n) = \frac{m^n e^{-m}}{n!}$$

where n = # photoelectrons generated/pulse

m = mean # photoelectrons generated/pulse

then, for m $\ll 1$, $P(1) \approx m = 0.0038$ in our case. The rate of double photoelectron pulses is expected to be a factor of $m/2 = 0.002$ lower than the single photoelectron rate.

The timing spectrum obtained with both LGS units is shown in figure 4.2c. The two peaks were separated by increasing the delay through the Ortec 425 unit by 8 nsec for one of them. Using this to calibrate the spectrum, the peaks were found to have a fwhm of 1.9 nsec. Since some of the time spread came from the TTS of the PMT, the widths of the light pulses were $\leq$ 1.9 nsec fwhm. These pulses are short enough to measure TTS's on the order of 7 nsec.

4.2 The Timing Resolution of the R1449 PMT over the Photocathode

With the grounded anode voltage divider (see figure 2.6a), an applied voltage of -2200V on the Hamamatsu R1449 PMT #ZW4706 and the electronics described in section 3.5.1, the timing resolutions and single photoelectron pulse height spectra were collected for various locations of the fibre-optic cable on the photocathode surface. The light was scanned over the PMT in two perpendicular directions; one parallel to and one perpendicular to the vanes on the first dynode. The PMT was rotated by 90° between the two sets of measurements so that the effects of the earth's magnetic field would be the same in both cases (see figure 3.6 for the direction of the earth's magnetic field). The walk adjust on the CFD was adjusted so that the width of the TAC peak was minimized for the fibre-optic cable at the centre of the photocathode, and was left at this setting for the other readings.

Figure 4.1b shows a typical pulse from the PMT before and after amplification by the Ortec 474 TFA (10 nsec integration time). The pulses from the TFA had a risetime of ~16 nsec and a fwhm of ~30 nsec. The light pulse generator was operated at 50 kHz. Figure 4.3a shows the pulse height spectrum, and figure 4.3b shows part of the timing spectrum for the fibre-optic cable located at the centre of the photocathode. Note that the pulse height spectrum shows no sign of a single photoelectron peak. This is typical for the R1449 PMT, which has poor energy resolution. However, because the pulse rate of the PMT was less than 4% of that of the light pulser, it was assumed that the signals were produced by single photoelectrons. The dark noise rate above the cutoff was measured to be about 8 kHz. Figure 4.4 shows the results of the scans parallel and perpendicular to the first dynode vanes. The lower pulse height cutoff was at channel #22. The gain of the PMT varied by ±35%, indicating that it is sensitive to the angle and position at which the photoelectrons strike the first dynode vanes. The timing peak centroids range over about 4.3 nsec, while their fwhm's range

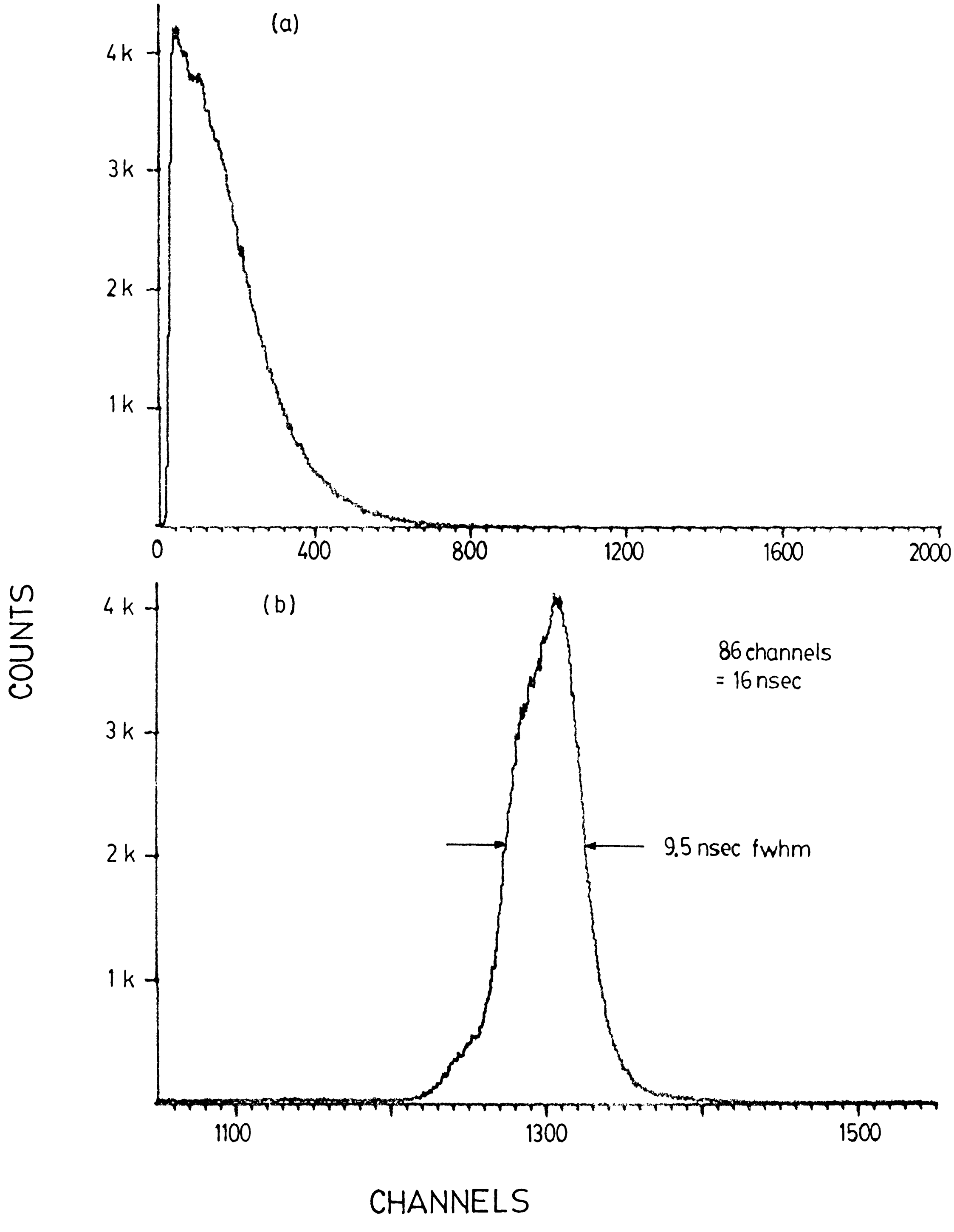

Figure 4.3: The single photoelectron pulse height spectrum (a) and part of the timing spectrum (b) for the fibre-optic cable located at the centre of the photocathode of PMT #ZW4706.

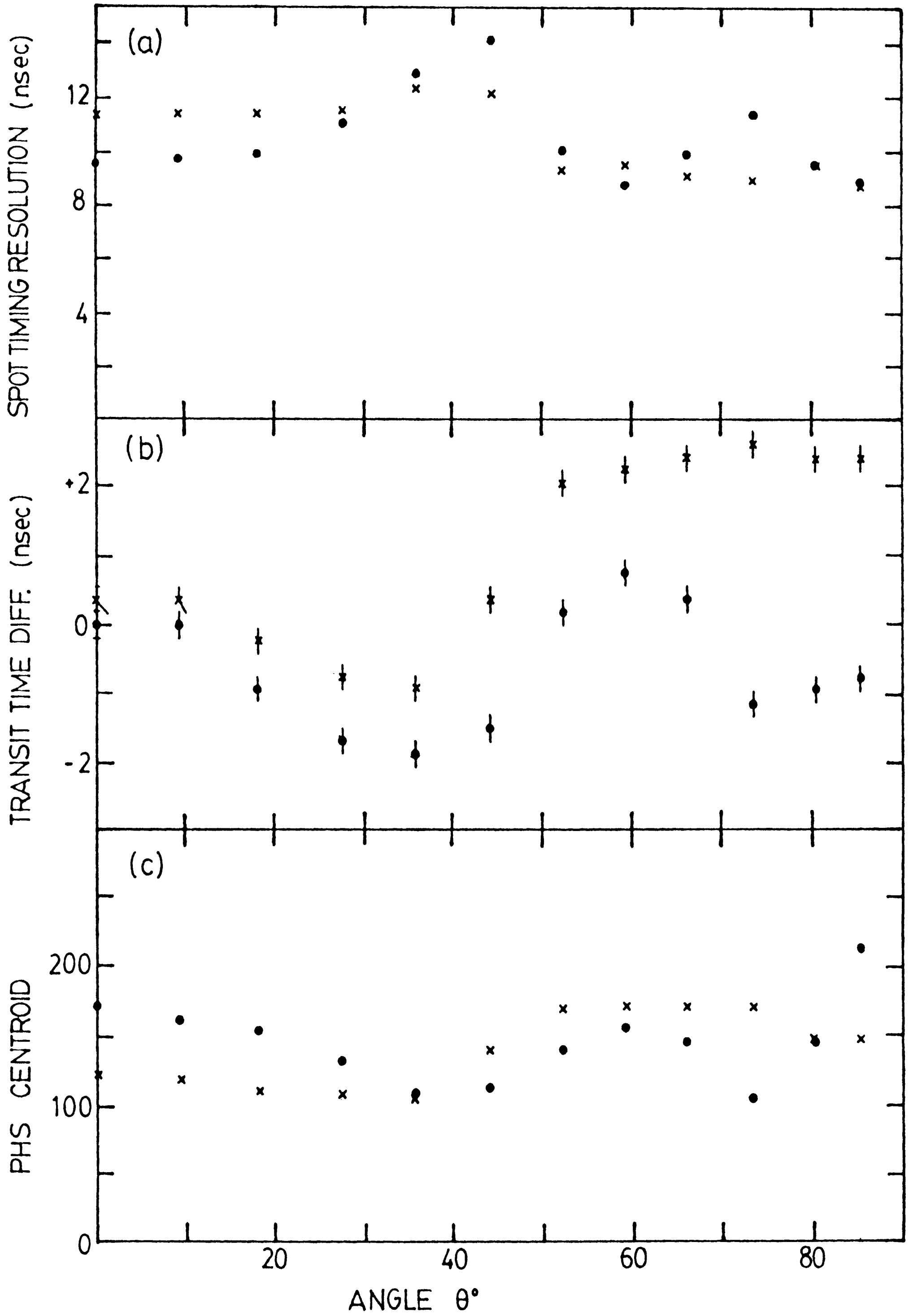

Figure 4.4: The spot timing resolution (a), the transit time difference (b), and the centroid of the single photoelectron pulse height distribution (2048 channels) (c) over the photocathode surface of PMT #ZW4706. The lower cutoff for the pulse height distribution is at channel #22. The crosses and dots are for scans perpendicular and parallel to the first dynode vanes, respectively.

from about 8.7 nsec up to 14 nsec. Combining these results indicates that the TTS for full photocathode illumination would be about 10.4 nsec. This resolution is worse than that quoted by Hamamatsu. However, when Hamamatsu measured the timing resolution, they set their lower cutoff at the 1/4 photoelectron (p.e.) level of the pulse height spectrum. Since there is no peak in the pulse height spectrum, the single photoelectron level m was determined to satisfy the equation [Ha82]:

$$\sum_{m/4}^{m}(\text{counts per channel}) = \frac{1}{2}\sum_{m/4}^{4m}(\text{counts per channel})$$

For the data shown above, the cutoff at channel #22 is substantially below the 1/4 p.e. level in all cases. As statistical fluctuations in the pulse shapes are larger for small amplitude pulses, the timing jitter of the CFD would increase with a lower cutoff. Figure 4.4 shows that poor timing resolution is associated with a large proportion of small amplitude pulses (*i.e.* the lowest pulse height spectrum centroids). Thus, the poorer resolution measured here is partially due to the lower cutoff.

In some cases, the rate at which the PMT was triggered by the light pulser near the outside of the photocathode increased by a factor of three or four over that at the centre. This is probably due to chemical impurities in the photocathode producing p-type levels between the valence and conduction bands [Na70]. The electrons at these levels could gain enough energy from the red light to be ejected from the photocathode where the valence electrons might not. This effect would not be as important for light above the threshold energy, as the density of electrons in the impurity levels is far lower than that in the valence levels.

4.3 A Comparison of Timing Techniques

A comparison of the LEAC and CFD techniques was first made using the fast RCA 8850 PMT, and the electronics described in section 3.5.2. With +2000V applied to the PMT, the walk adjust on the Ortec 473A CFD was set to minimize the width of the TAC peak. The digitized TAC and linear signals were then written to magtape in event-by-event mode. The CFD was switched into leading edge mode (selected by a front panel switch) without changing the discriminator settings, and the digitized signals were written to magtape. The data from each magtape were then read back event-by-event by the PDP-15 computer, and the TAC pulses were sorted in various spectra according to the amplitude of the corresponding linear pulses. For the first data set, with the CFD adjusted correctly to eliminate amplitude walk in the triggering time, the TAC peak is at the same location. For the leading edge data set, however, because of time slewing, the position of the TAC peak in the large amplitude pulse spectra is shifted down from those in the low amplitude pulse spectra. The relative shift in each peak for both timing techniques is shown in figure 4.5. The leading edge TAC spectra were shifted back by the corresponding amount before summing them together to give the LEAC timing spectrum.

The TAC spectra for the CFD, leading edge and LEAC timing techniques were compared to test the relative performance of each (see figure 4.6). A timing resolution of 2.1 nsec fwhm was measured using the CFD. A poorer resolution of 3.5 nsec fwhm was measured using the LE discriminator. This was improved to 2.5 nsec fwhm after correcting for the amplitude walk using the LEAC technique. Thus, for the RCA 8850

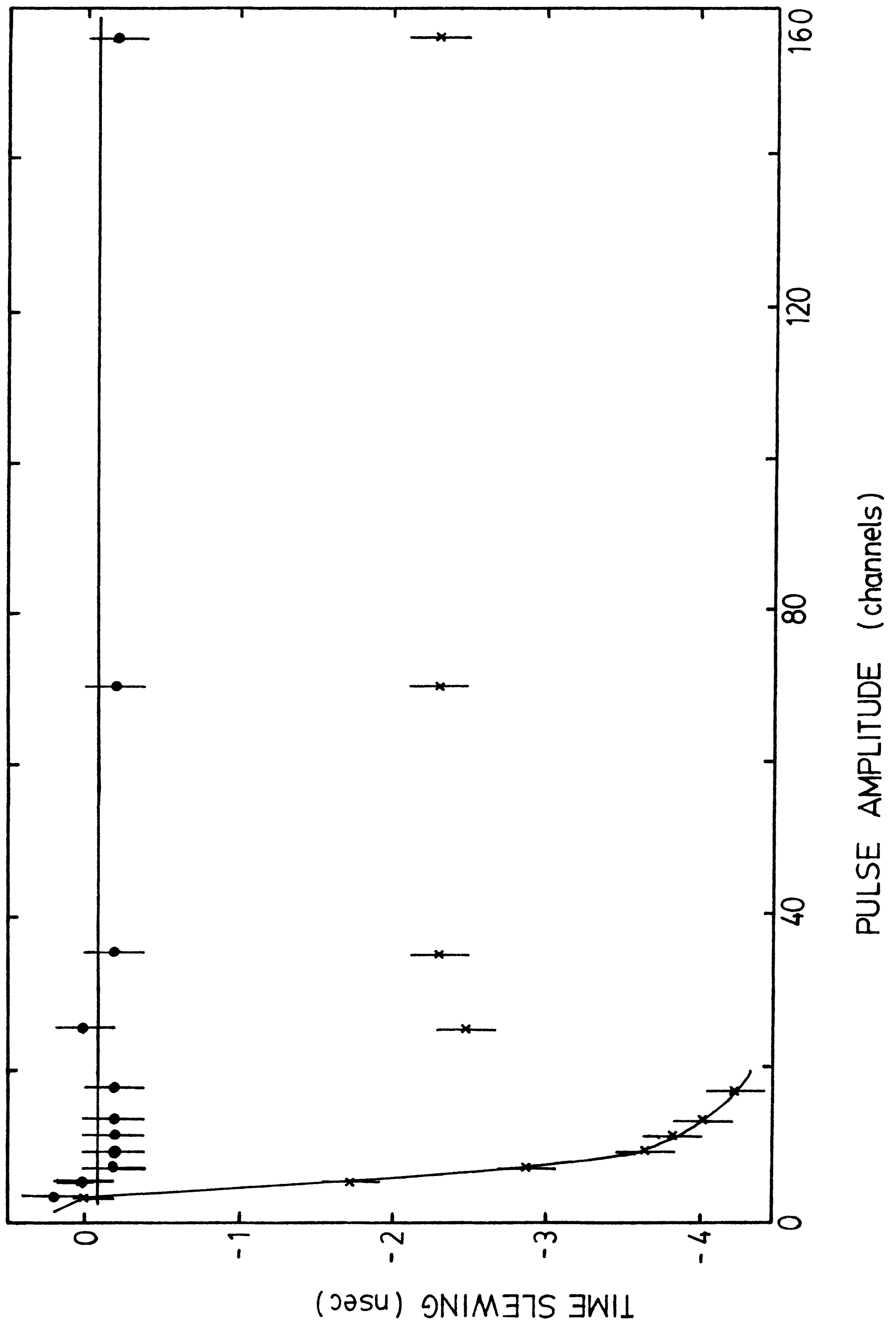

Figure 4.5: Trigger time slewing as a function of pulse amplitude for constant fraction and leading edge timing using the Ortec 473A CFD and the RCA 8850 PMT. The crosses and dots are for LE and CF timing, respectively, and the lines are guides to the eye. 'Pulses' with amplitudes above ~20 channels are probably multiple pulses summed together by the slow amplifier (integration time ~ 1 μsec). For these multiple pulses, the LE time slewing is determined by the amplitude of the first pulse, not by the summed amplitudes of all of the pulses. The TAC peaks measured for these multiple pulses are all identical in shape and position to the single pulse LE timing peak. Hence, the LE time slewing of ~2.3 nsec measured for these multiple pulses is the average time slewing of the single pulses.

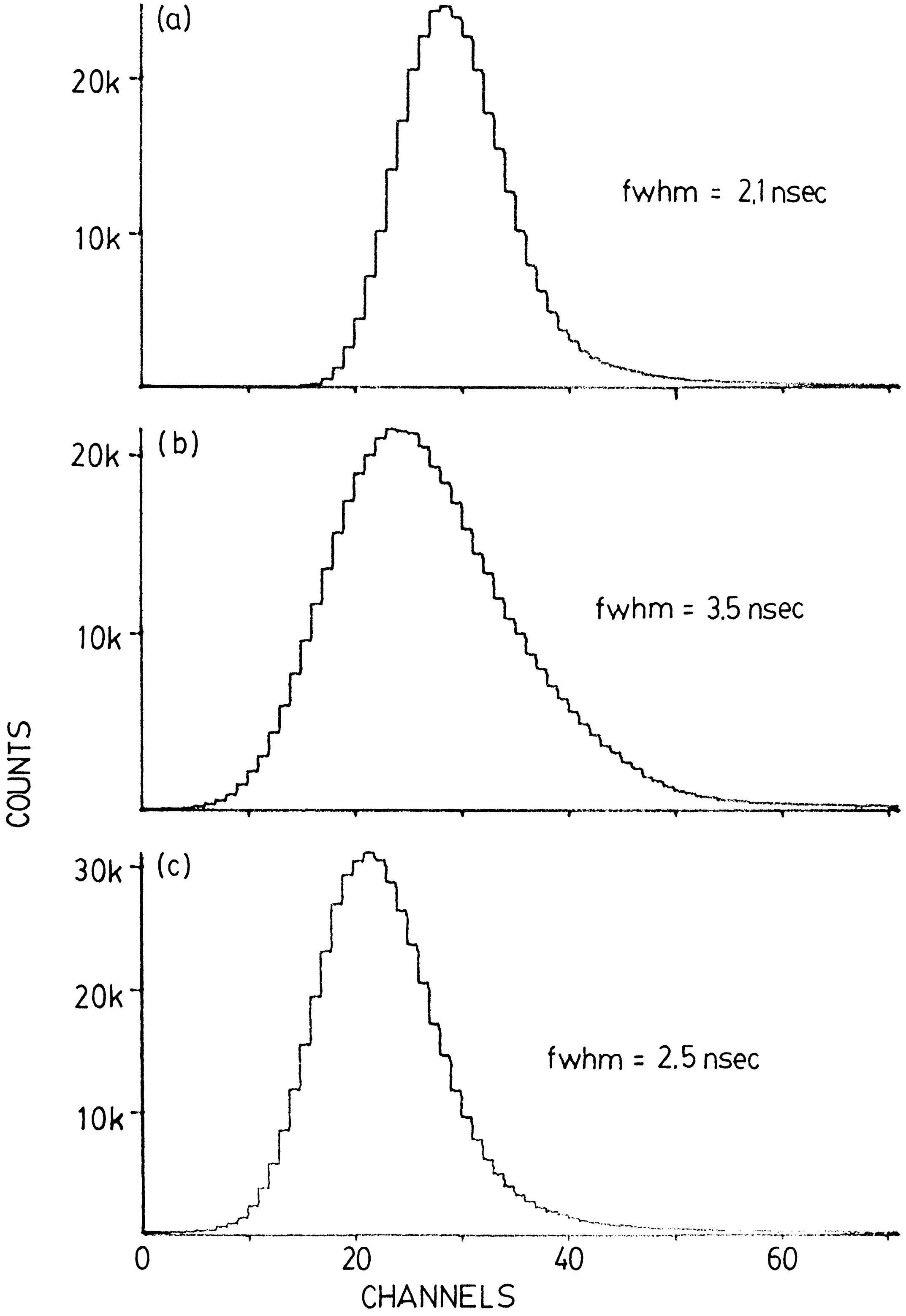

Figure 4.6: Comparison of the constant fraction (a), leading edge (b) and LEAC (c) timing resolutions for the RCA 8850 PMT.

PMT, the LEAC technique offers a substantial improvement in the timing resolution over LE timing, comparable to that of CF timing.

The next step was to test the LEAC technique with the 20″ PMT. With -2200V applied to the grounded anode voltage divider on PMT #ZW4706, and the timing unit switched to leading edge mode, the light was scanned over the PMT in two perpendicular directions (as described in section 4.2). In each scan, the light was shone at four points on the photocathode corresponding to angles of 0°, 30°, 60° and 85° (see figure **??**), and the pairs of digitized TAC and linear signals were written to magtape. The data were sorted by computer and the time slewing as a function of linear pulse height was measured. The average LE discriminator trigger time slewing is shown in figure 4.7. These measured offsets were then used to correct the raw data from the TAC, and the fwhm of the corrected TAC peak was measured for each location of the fibre-optic cable on the PMT surface. Table 4.1 gives the pulse height spectrum centroid and timing peak width measured at each photocathode location before and after correcting for the time slewing. The lower cutoff was roughly at the 1/4 p.e. level. The LEAC technique improved the timing resolution over the LE technique by about 4-5 nsec for the $\theta = 0°$, 60° and 85° data, and by about 1-2 nsec for the $\theta = 30°$ data. The resolutions of the amplitude sorted timing peaks are generally poorer for the small amplitude PMT pulses. However, the timing resolutions for the $\theta = 30°$ data are substantially worse than those measured at the other angles, for all amplitude pulses. This shows that the poor timing at that location may be intrinsic to the dynode structure, and is not due wholly to the timing unit's response to smaller amplitude pulses there.

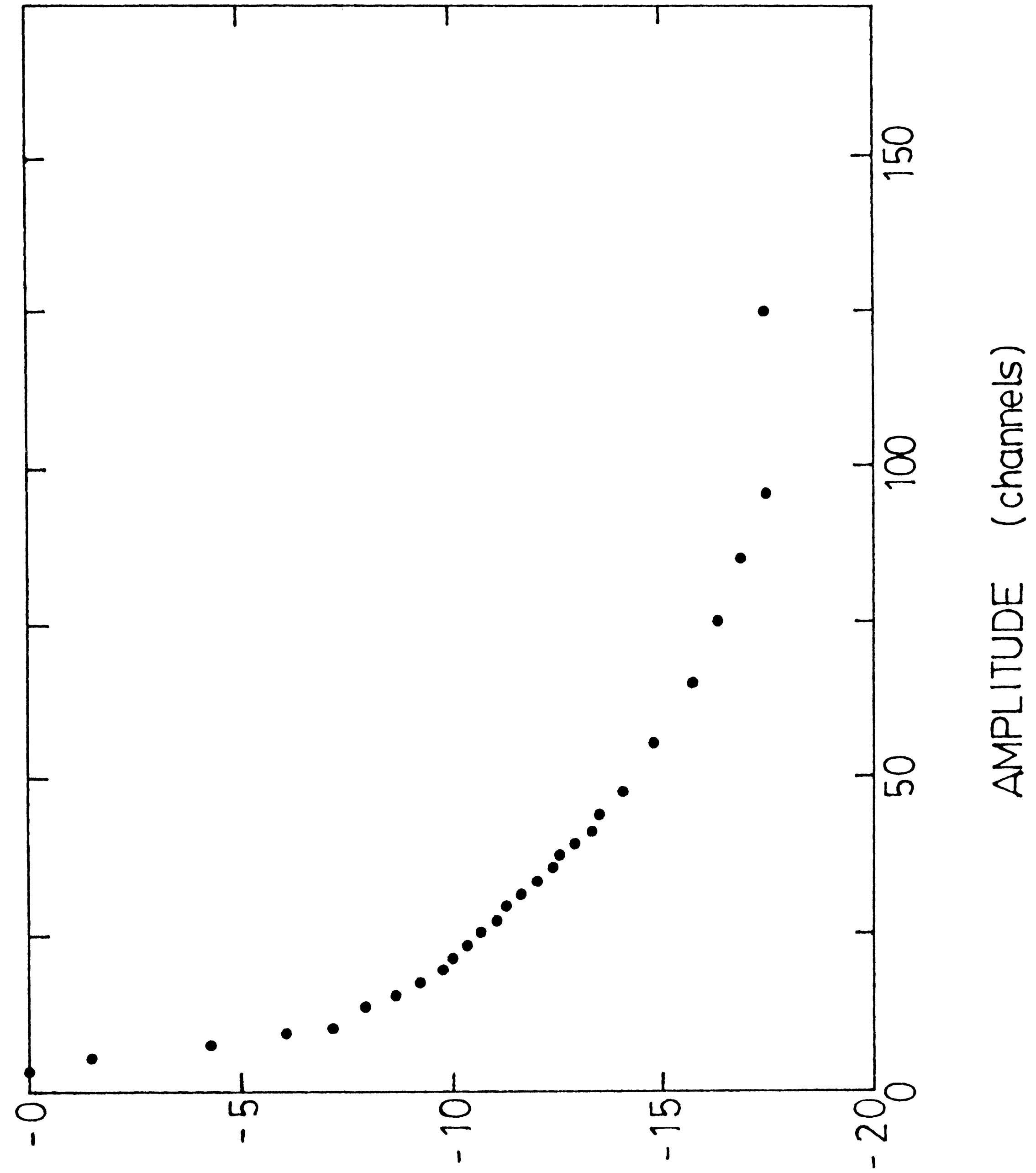

Figure 4.7: The average leading edge trigger time slewing as a function of pulse amplitude for PMT #ZW4706.

PMT orientation	fibre-optic position	pulse height centroid	TTS (nsec) unshifted	TTS (nsec) shifted
↓	30°	15±1	12.03±0.08	11.39±0.06
===	60°	24±1	12.97±0.09	8.81±0.07
===	85°	22±1	13.03±0.11	7.96±0.06
↓	0°	23±1	14.18±0.11	10.54±0.05
‖‖‖	30°	16±1	13.69±0.09	11.89±0.05
‖‖‖	60°	23±1	13.93±0.12	9.68±0.07
	85°	24±1	14.00±0.08	8.64±0.05

Table 4.1: The centroids of the single photoelectron pulse height spectra (256 channels) and the timing resolutions over the photocathode surface of PMT #ZW4706 before and after correcting for the leading edge time slewing. The cutoff for the pulse height spectrum was at the 1/4 p.e. level. The two PMT orientations refer to the scans perpendicular and parallel to the first dynode vanes.

The TTS measured at each photocathode location is in agreement with the previous measurement using the CFD timing unit (see section 4.2). However, the cutoff for the CFD unit was lower than that used for the LE unit. With the same cutoff, it is expected that the timing resolution would be better for the CFD unit.

In each timing spectrum, there is a small peak that starts on the tail of the main peak and is cut off about 100 nsec after the centroid of the main peak (see figure 4.8). The number of counts under each small peak ranges from 2% - 17% of that under the corresponding main peak. These peaks were also seen in the timing spectra of section 4.2 obtained with a CFD, indicating that they probably were not caused by the timing discriminators. The number of counts under each peak is not proportional to the number of counts under the main peak, indicating that they were not produced by delayed light emission in the light pulser. The shape and structure

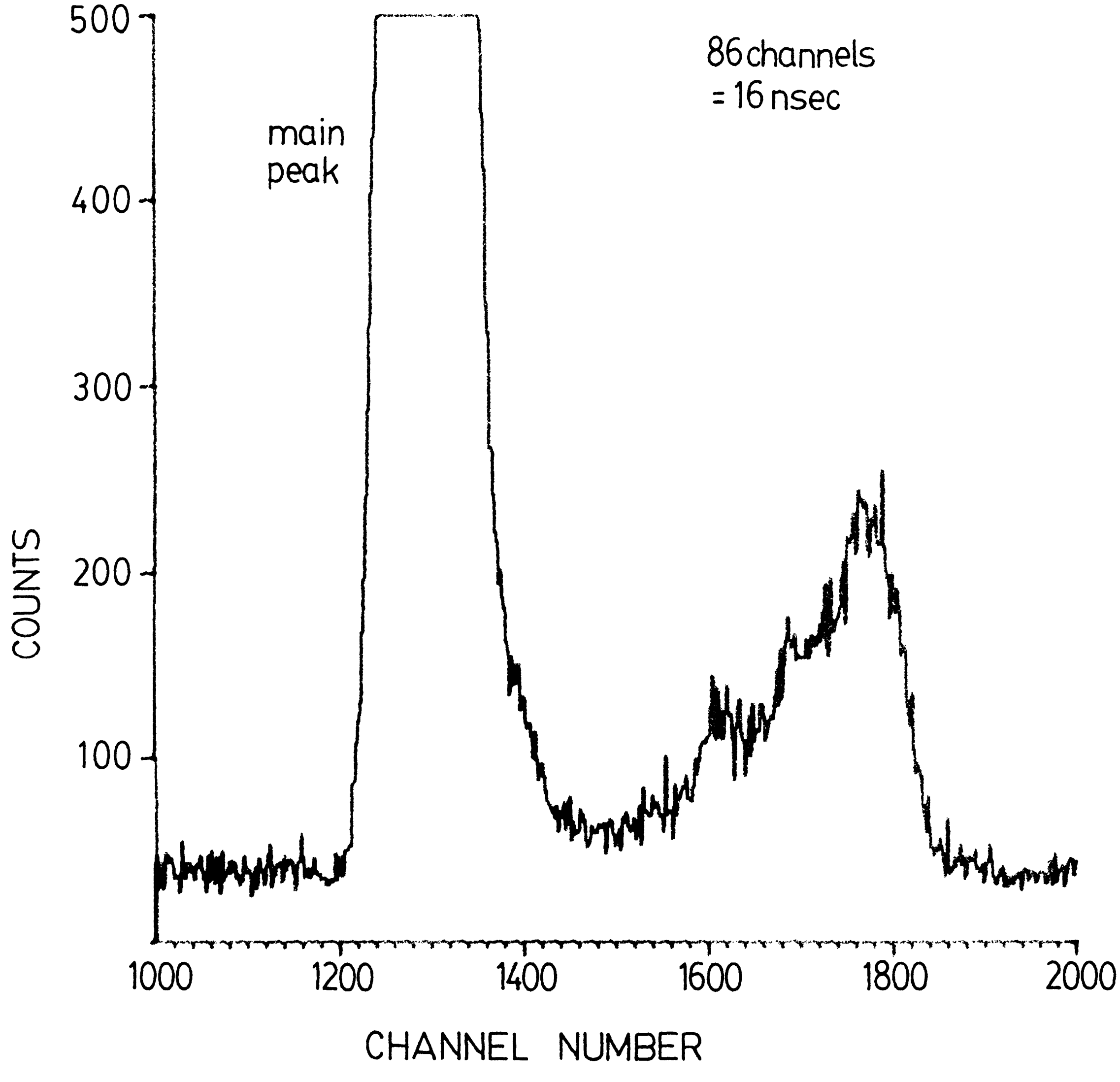

Figure 4.8: Afterpulsing peak in a timing spectrum of PMT #ZW4706, probably caused by photons generated at the dynodes ejecting photoelectrons from the photocathode.

of the trailing peaks, and their cut off 100 nsec after the main peak, suggest that they were produced by afterpulses in the PMT triggered by photons generated at the dynodes. The afterpulses would only stop the TAC if the initial pulses were below the discriminator level set on the timing unit. Thus, the true afterpulsing rate must be greater than that measured in the trailing peak, as larger pulses which triggered the timing unit would be expected to produce more photons at the dynodes.

4.4 Double Constant Fraction Timing

With the electronics described in section 3.5.3, the anode pulses from PMT #ZW4706 were visually examined. The fibre-optic cable was positioned at the centre of the photocathode. A new base with a 16-1-...-1 ratio of resistors in the grounded anode voltage divider was used to increase the potential between the photocathode and the first dynode and thus decrease the photoelectron flight time spread. This ratio, however, reduces the potential down the electron multiplier; so to maintain the gain a bias of -2600V was applied across the divider. Figure 4.9 shows some photographs of typical single photoelectron pulse shapes obtained with the 100 MHz storage oscilloscope.

For 438 single photoelectron pulses of random amplitude (the lower cutoff was at the 1/4 p.e. level), the time for each pulse to reach 1/4 and 3/4 of its maximum amplitude was recorded (equivalent to double constant fraction timing). Using linear extrapolation, the zero voltage intercept was calculated for each pulse and taken as its arrival time. A histogram of the pulse arrival times is shown in figure 4.10. The fwhm of the peak in the histogram was measured to be 6.5±0.3 nsec. The timing resolution previously measured with the Ortec 473A CFD was 9.5 nsec fwhm. This

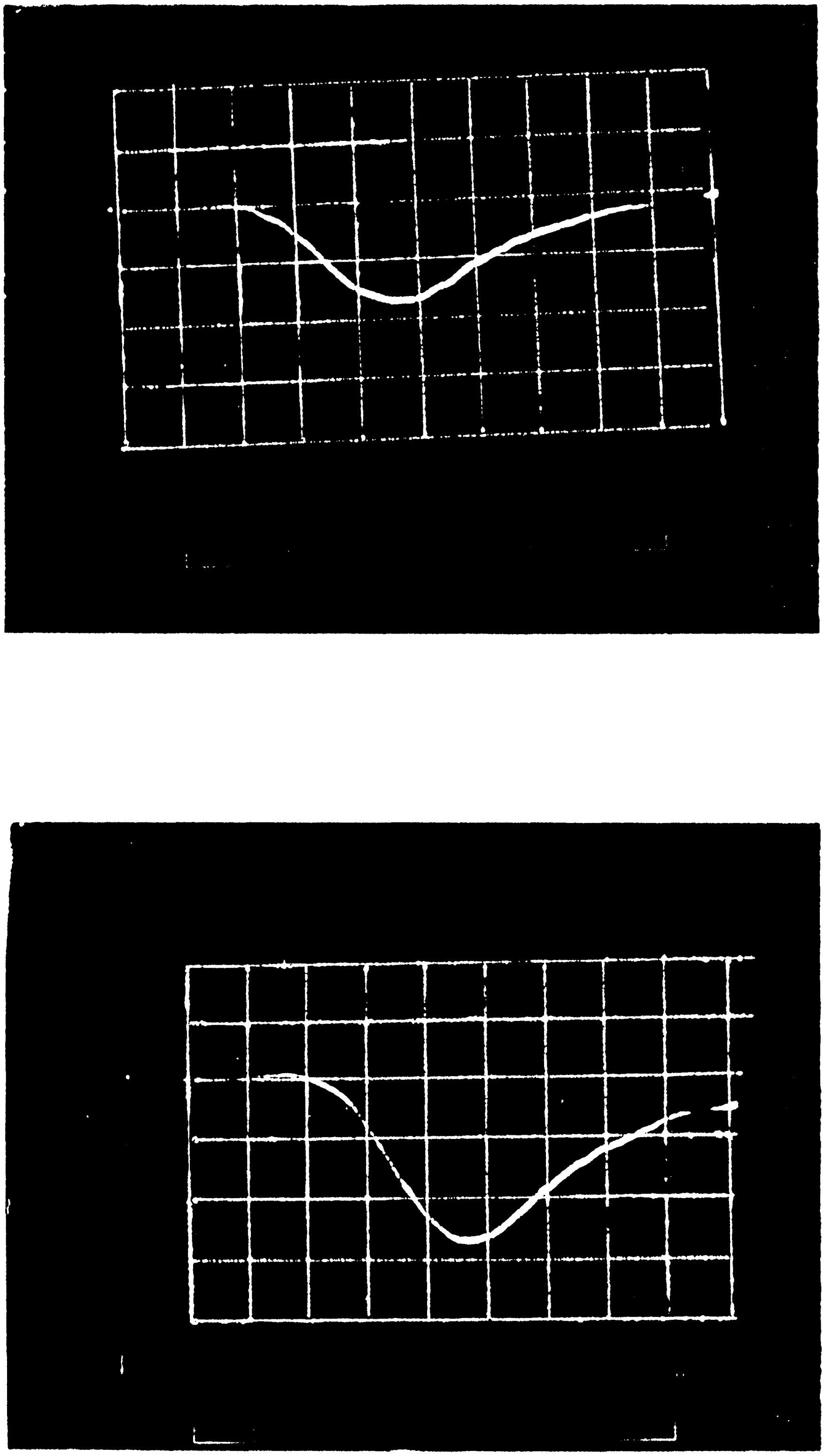

Figure 4.9: Photographs of typical single photoelectron pulses from PMT #ZW4706 after amplification by an Ortec 474 TFA (integration time ~10 nsec) obtained with the 100 MHz Tektronix 466 storage oscilloscope. The time scale is 10 nsec/div, and the voltage scale is 40 mV/div.

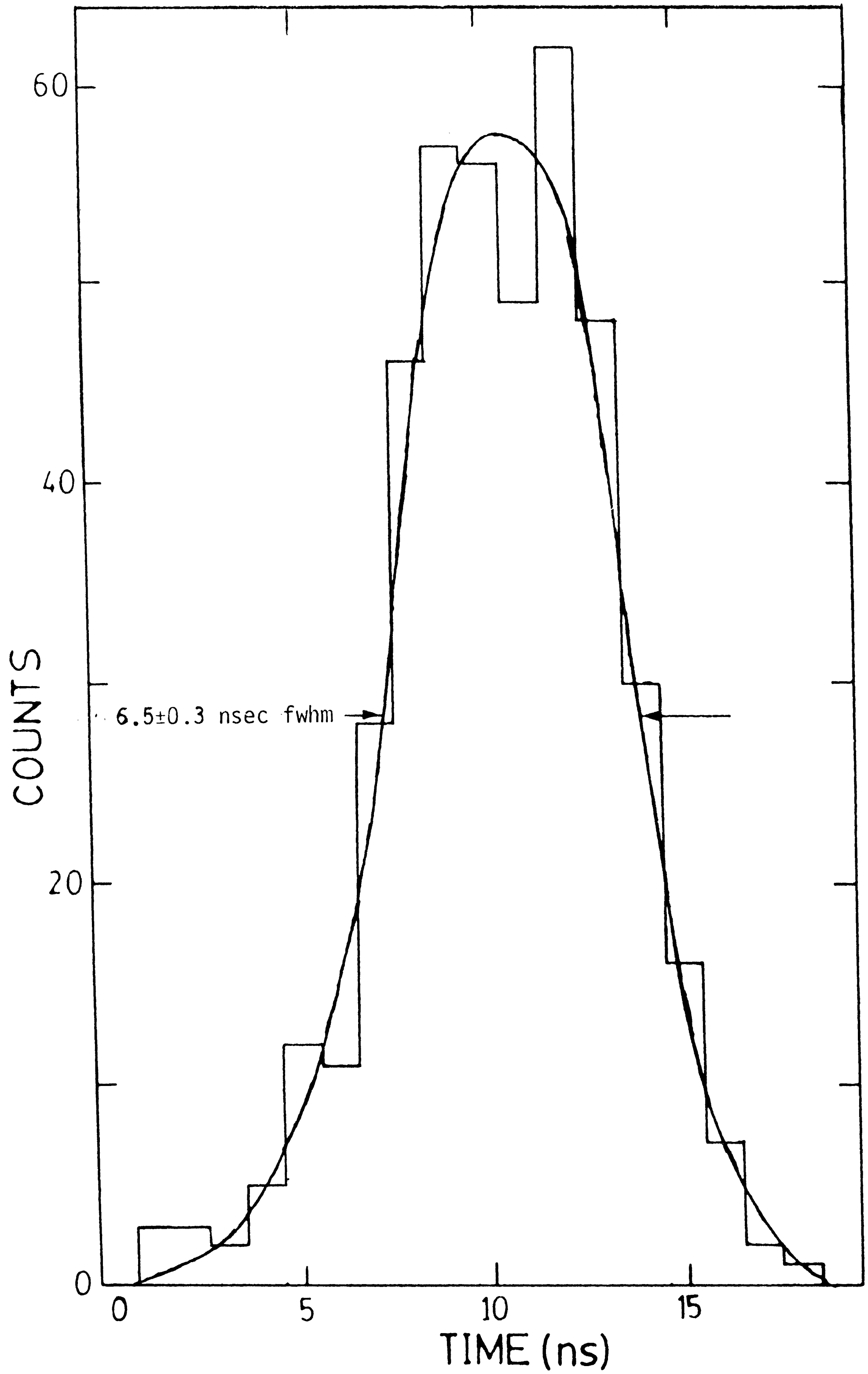

Figure 4.10: Spot timing resolution of the PMT #ZW4706 using double constant fraction timing with the 100 MHz Tektronix 466 storage oscilloscope.

indicates that the Ortec unit was significantly degrading the timing resolution of the system. The fibre-optic cable was scanned over the photocathode, but there was no measurable change in the pulse arrival times as seen on the oscilloscope, indicating that the transit time difference across the PMT surface was less than the TTS. An upper limit of 4 nsec is estimated for the transit time difference from these measurements.

4.5 Optimizing the Timing Jitter in the Electronics

This experiment determines what the best combination of timing filter amplifier and discriminator level on the timing unit is for minimizing the timing jitter in the electronics. The TFA reproduces pulse shapes most accurately if it can be operated at low gain. The discriminator level of the CFD or LE discriminator must then be set low as well so as not to reject too many small amplitude pulses and reduce the efficiency of the system. But it is for these small amplitude pulses that the timing walk is the worst, so that operating the TFA for good timing means poorer results from the timing unit. The reverse of this is also true in that raising the discriminator level means that the gain of the amplifier must be raised as well, which generally increases the risetime of the TFA's output.

The electronics described in section 3.5.2 for comparing timing techniques was used to find the optimum TFA gain/discriminator level combination. Two timing units were used: an Ortec 584 CFD and an Ortec 552 Pulse Shape Analyzer (PSA). The 584 CFD's discriminator can be set as low as 5 mV. The 552 PSA has a trailing edge CFD instead of the normal leading edge CFD, and a minimum discriminator level of 50 mV. A new base with a grounded cathode voltage divider (see figure 2.6b) was put on the 20″ PMT #ZW4706, as the dark count rate of both 20″ PMT's had suddenly increased (>50 kHz) after a period of a couple of months with the large negative potential applied to the photocathode. Grounding the photocathodes during operation reduced the noise rates to their previous levels. Hence, a bias of +2600V was applied to the PMT, and the signal was picked off the power line. The fibre-optic cable was positioned at the centre of the photocathode for each measurement, and the PMT was oriented so that the first dynode vanes were parallel to the horizontal component of the earth's magnetic field.

With the 584 CFD in place and operating in the CF mode, the discriminator level was set to 12 mV and the gain of the TFA adjusted until the cutoff in the pulse height spectrum was at the 1/4 p.e. level. At the same time, the walk adjust was set to minimize the TAC peak width. The lower level discriminator on the TSCA for the linear signals was set as low as possible so that the cutoff in the pulse height spectrum would be determined only by the discriminator level of the CFD. The reverse of this had been tried, where the discriminator of the TSCA for the linear signals was set to the 1/4 p.e. level and the CFD discriminator level was lowered below this. It was found, however, that the CFD was triggering constantly on the noise, so that this method was rejected.

With the CFD in CF mode, the linear and TAC spectra were collected on the PDP-15 computer. The CFD was then switched to leading edge mode and the pairs of linear and TAC signals were stored in event-by-event mode on magtape, so that the

Unit	Disc. Level (mV)	CF	LE	LEAC
Ortec 584	6	10.43±0.09	15.72±0.10	10.06±0.06
	12	9.93±0.07	16.03±0.11	10.10±0.06
	30	9.41±0.07	15.44±0.11	9.52±0.05
	50	9.19±0.07	15.46±0.11	9.51±0.05
	50*	9.36±0.10	14.41±0.11	9.65±0.05
	100*	9.17±0.10	14.90±0.11	9.67±0.06
Ortec 552	50	15.80±0.33	–	–

Table 4.2: The spot timing resolutions of PMT's #ZW4706 and #ZW4673 for the various timing techniques and discriminators used. The * indicates that PMT #ZW4673 was used in the measurement. In all other cases, PMT #ZW4706 was used.

TAC signals could later be corrected for time slewing by the LEAC technique. This procedure was repeated for discriminator levels of 6, 20, 30 and 50 mV on the 584 CFD, and for 50 mV on the 552 PSA. However, no leading edge event-by-event data were taken for the 552 PSA as it only operates on the trailing edge of the pulses. The 20″ PMT #ZW4706 was replaced by #ZW4673 so that it could be tested in a similar manner. The latter PMT was operated at +2500V so that its gain was the same as the first PMT's. The same procedure as above was carried out for discriminator levels of 50 and 100 mV on the 584 CFD.

The magtape data were sorted and the TAC signals corrected for time slewing in the LE discriminator. Table 4.2 shows the timing resolution of the R1449 PMT for the various timing techniques and discriminators used. The best resolution of 9.2 nsec fwhm was obtained using the Ortec 584 unit in CF mode, with a high discriminator level and timing amplifier gain. However, the timing resolution measured suing LEAC discrimination was only marginally worse at 9.5 nsec. The Ortec 552 pulse shape analyzer is a trailing edge CFD designed for use with slow pulses which have been shaped by a main amplifier, which explains why its timing performance for the fast anode pulses was as poor as that of the LE discriminator.

Chapter 5

The Simulation of Photoelectron Trajectories

To estimate the effects of magnetic fields on the collection efficiency and flight time spread of the photoelectrons in the 20″ PMT, a computer program was written to simulate their trajectories and flight times. This program solves the equations of motion of the electron in a static electric and magnetic field. The acceleration is given by

$$\vec{a} = \frac{q}{m}(\vec{E} + \vec{v} \times \vec{B}) \tag{5.1}$$

where q/m is the charge to mass ratio of the electron, $\vec{E}$ is the electric field, $\vec{v}$ is the velocity of the electron and $\vec{B}$ is the magnetic field. Since the photoelectron energy never exceeds 1.5 keV (corresponding to v/c $\approx$ 0.076), relativistic effects are ignored. The potential in the 20″ PMT is calculated using relaxation techniques. The electric field (gradient of the potential) is calculated using finite difference methods. The three coupled second-order differential equations obtained from eqn. 5.1 are solved numerically using the Fourth-Order Runge-Kutta method. A detailed description of these calculations is given below (the computer source code is given in the appendix).

Since the 20″ PMT is axially symmetric, the potential in the PMT can be expressed as $V(r, z)$ with no ϕ-dependence in the cylindrical coordinate frame. However, the equations of motion of the electron are most easily solved using a Cartesian coordinate system. Hence the gradient of the potential is calculated in the cylindrical coordinate frame and transformed to the Cartesian coordinate frame through the equations:

$$\frac{\partial V}{\partial x} = \frac{x}{r}\frac{\partial V}{\partial r} = \frac{x}{\sqrt{x^2+y^2}}\frac{\partial V}{\partial r} \tag{5.2a}$$

$$\frac{\partial V}{\partial y} = \frac{y}{r}\frac{\partial V}{\partial r} = \frac{y}{\sqrt{x^2+y^2}}\frac{\partial V}{\partial r} \tag{5.2b}$$

The acceleration is then written as:

$$\frac{d^2x}{dt^2} = \frac{q}{m}\left[\frac{-x}{\sqrt{x^2+y^2}}\frac{\partial V}{\partial r} + \frac{dy}{dt}B_z - \frac{dz}{dt}B_y\right] \tag{5.3a}$$

$$\frac{d^2y}{dt^2} = \frac{q}{m}\left[\frac{-y}{\sqrt{x^2+y^2}}\frac{\partial V}{\partial r} + \frac{dz}{dt}B_x - \frac{dx}{dt}B_z\right] \tag{5.3b}$$

$$\frac{d^2z}{dt^2} = \frac{q}{m}\left[-\frac{\partial V}{\partial z} + \frac{dx}{dt}B_y - \frac{dy}{dt}B_x\right] \tag{5.3c}$$

To solve the three coupled second-order differential equations 5.3, the potential in the PMT has to be calculated first. This was done using a Successive Over-Relaxation calculation on a grid with 0.25 cm spacing. The steps to the solution are outlined below.

5.1 The PMT Geometry

Figure 5.1 shows the geometry of the 20″ PMT used in the calculations. Since the PMT is axially symmetric, all of the calculations for the potential or electric field need only be done in the $r - z$ plane. The scale on the axes was chosen to be 1 unit

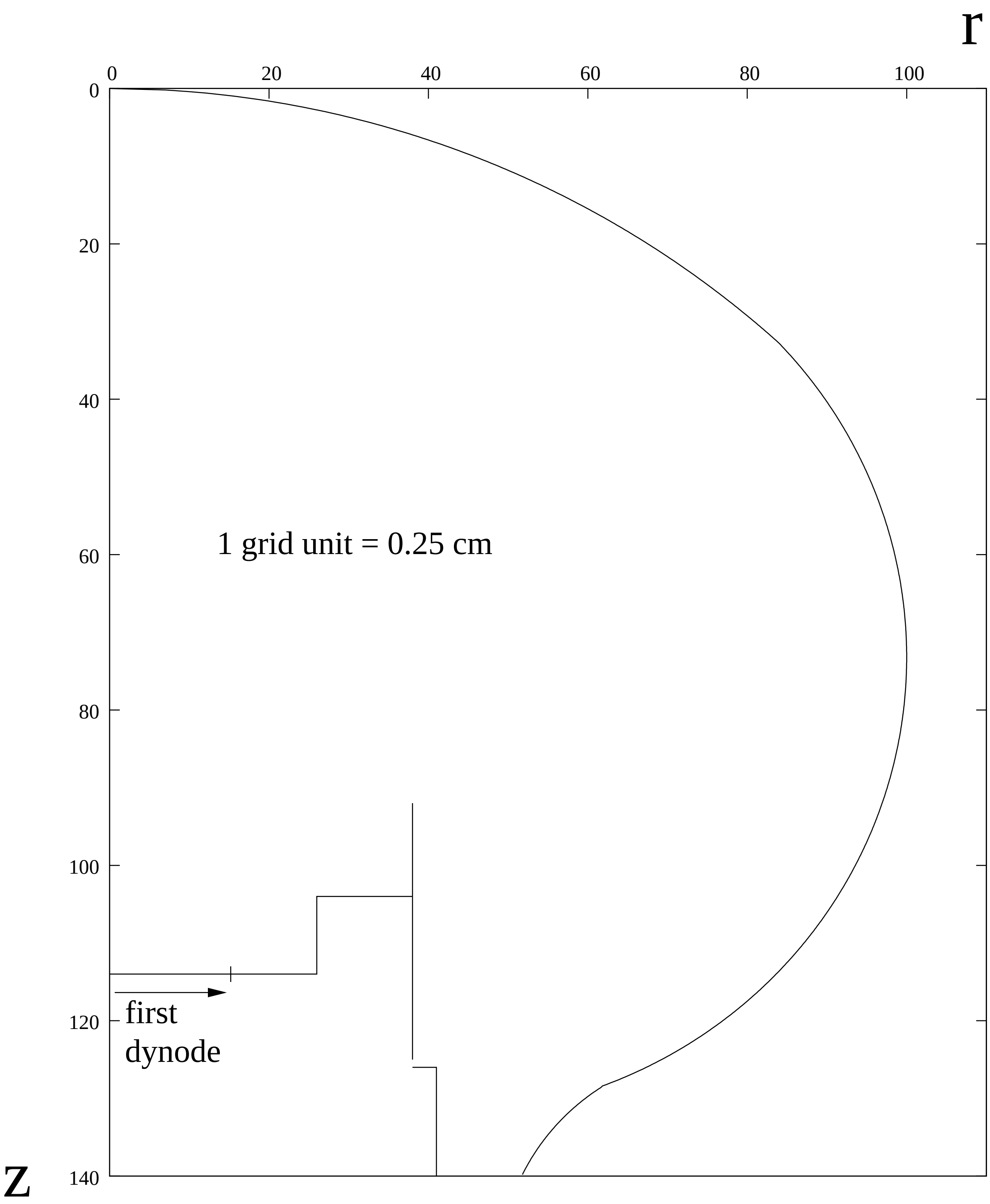

Figure 5.1: Geometry of the R1449 PMT used in the computer simulations.

= 0.25 cm to coincide with the grid spacing of the potential array. The size and position of each part was obtained from a scale drawing provided by Hamamatsu. The photocathode surface in the $r-z$ plane was modelled using parts of circles, and described algebraically as:

$$r = \sqrt{124^2 - (124 - z)^2} \qquad ; \quad 0 \leq z < 32.7 \tag{5.4a}$$

$$r = 41 + \sqrt{59^2 - (z - 73.2)^2} \qquad ; \quad 32.7 \leq z < 128.5 \tag{5.4b}$$

$$r = 77 - \sqrt{28^2 - (152 - z)^2} \qquad ; \quad 128.5 \leq z \leq 152.0 \tag{5.4c}$$

5.2 Derivatives Using the Central Difference Approximation

The derivatives of the potential on the grid are approximated using the central difference method. All equations are derived using Taylor expansions. The value of a function f at small displacement Δx from x_0 can be expressed as

$$f(x_0 + \Delta x) = f_0 + f_0' \cdot (\Delta x) + 1/2 f_0'' \cdot (\Delta x)^2 + 1/6 f_0''' \cdot (\Delta x)^3 + \cdots \tag{5.5}$$

where f_0, f_0', f_0'' and f_0''' are the values of the function and its first, second and third partial derivatives at x_0. At positions $x_1 = x_0 + ph$ and $x_{-1} = x_0 - rh$, where h is the grid spacing and p, r are some positive coefficients, the functions can be expressed as

$$f_1 = f_0 + f_0' \cdot ph + 1/2 f_0'' \cdot (ph)^2 + 1/6 f_0''' \cdot (ph)^3 + \cdots \tag{5.5a}$$

$$f_{-1} = f_0 - f_0' \cdot rh + 1/2 f_0'' \cdot (rh)^2 - 1/6 f_0''' \cdot (rh)^3 + \cdots \tag{5.5b}$$

The f_0'' terms can be eliminated from eqns. 5.5a and 5.5b and the value of f_0' expressed as

$$f_0' = \frac{r^2 f_1 - p^2 f_{-1} + (p^2 - r^2) f_0}{(r^2 p + p^2 r)} \qquad + \quad \mathcal{O}(h^2) \tag{5.6}$$

where $\mathcal{O}(h^2)$ indicates an error term on the order of h^2.

For the case where x_{-1}, x_0 and x_1 are on the grid (*i.e.* $r = p = 1$), we have the well-known expression for the first order partial derivative at x_0

$$f_0' = \frac{f_1 - f_{-1}}{2h} \qquad + \quad \mathcal{O}(h^2) \tag{5.7}$$

The f_0' term can be eliminated from eqns. 5.5a and 5.5b and the value of f_0'' expressed as

$$f_0'' = \frac{2(r f_1 + p f_{-1} - (p + r) f_0)}{(r p^2 + r^2 p) h^2} \qquad + \quad \mathcal{O}(h) \tag{5.8}$$

For the case where $r = p = 1$,

$$f_0'' = \frac{f_1 - 2 f_0 + f_{-1}}{h^2} \qquad + \quad \mathcal{O}(h^2) \tag{5.9}$$

In all of the following calculations, the partial derivatives are calculated using the four basic equations 5.6 - 5.9.

5.3 Calculating the Potential in the PMT

The iterative Successive Over-Relaxation method was used to calculate the potential in the PMT. The Laplace equation for an axially symmetric potential V in cylindrical coordinates is

$$\nabla^2 V = \frac{\partial^2 V}{\partial r^2} + \frac{1}{r}\frac{\partial V}{\partial r} + \frac{\partial^2 V}{\partial z^2} = 0 \tag{5.10}$$

By substituting into 5.10 the appropriate expressions for the partial derivatives 5.6 - 5.9, the potential at any point in the grid can be expressed in terms of the potentials at its neighbouring points. There are three basic cases to consider.

In the first case, the point at which the potential is calculated has four equidistant grid points around it (*i.e.* $p = q = r = s = 1$). Denoting the potential at grid point (i, j) as $V_{i,j}$, and using eqns. 5.7 and 5.9, Laplace's eqn. becomes

$$\begin{aligned}
\nabla^2 V &= \frac{V_{i,j+1} - 2V_{i,j} + V_{i,j-1}}{h^2} + \frac{V_{i,j+1} - V_{i,j-1}}{2(j-1)h^2} \\
&\quad + \frac{V_{i+1,j} - 2V_{i,j} + V_{i-1,j}}{h^2} \qquad + \quad \mathcal{O}(h^2) \\
&= \frac{mV_{i,j+1} + nV_{i,j-1} + V_{i+1,j} + V_{i-1,j} - 4V_{i,j}}{h^2} \qquad + \quad \mathcal{O}(h^2) \\
&= 0
\end{aligned}$$

$$\text{where} \quad m = (1 + 1/(2(j-1)) \quad \text{and} \quad n = (1 - 1/(2(j-1))$$

From this, $V_{i,j}$ can be expressed as

$$V_{i,j} = \frac{mV_{i,j+1} + nV_{i,j-1} + V_{i+1,j} + V_{i-1,j}}{4} \qquad + \quad \mathcal{O}(h^4) \tag{5.11}$$

In the second case, at $r = 0$, the derivative $\partial V/\partial r$ goes to zero and the $1/r\ \partial V/\partial r$ term in Laplace's eqn. cannot be approximated as above. However;

$$\lim_{r \to 0} \left[\frac{1}{r} \frac{\partial V}{\partial r} \right] = \frac{\partial^2 V}{\partial r^2}$$

so that

$$\begin{aligned}
\left[\frac{\partial^2 V}{\partial r^2} + \frac{1}{r} \frac{\partial V}{\partial r} \right]_{r=0} &= 2\frac{\partial^2 V}{\partial r^2} \\
&= \frac{4(V_{i,2} - V_{i,1})}{h^2} \qquad + \quad \mathcal{O}(h^2)
\end{aligned}$$

since $j = 1$ at $r = 0$. Laplace's eqn. then becomes

$$\begin{aligned}\nabla^2 V &= \frac{4(V_{i,2} - V_{i,1})}{h^2} + \frac{V_{i+1,j} - 2V_{i,1} + V_{i-1,j}}{h^2} \qquad + \quad \mathcal{O}(h^2) \\ &= 0\end{aligned}$$

$V_{i,1}$ is then expressed as

$$V_{i,1} = \frac{4V_{i,2} + V_{i+1,1} + V_{i-1,1}}{6} \qquad + \quad \mathcal{O}(h^4) \tag{5.12}$$

In the final case, if the point is near the photocathode where some of the grid points on the boundary may not be equidistant from the other points (*i.e.* at least one of $p, q, r, s \neq 1$), then the more general expressions 5.6 and 5.8 must be substituted into Laplace's eqn. The potential $V_{i,j}$ is then expressed as

$$V_{i,j} = \frac{aV_{i,j+1} + bV_{i,j-1} + cV_{i+1,j} + dV\,{}_i - 1, j}{e} \qquad + \quad \mathcal{O}(h^3) \tag{5.13}$$

$$\text{where} \qquad \begin{aligned} a &= \frac{(2 + r/(j-1))}{p(p+r)} & b &= \frac{(2 - p/(j-1))}{r(p+r)} \\ c &= \frac{2}{q(q+s)} & d &= \frac{2}{s(q+s)} \\ e &= \frac{2}{pr} + \frac{2}{qs} - \frac{p-r}{pr(j-1)} \end{aligned}$$

Using eqns. 5.11 - 5.13, one could repeatedly sweep through all of the points in the grid, recalculating the potential at each point until they all converge to their final values. This technique is known as the Relaxation method. A variation on this technique was used here, the Successive Over-Relaxation (SOR) method. Denoting V^k as the value of V calculated on the k'th sweep through the grid, eqn. 5.11 is rewritten as

$$V^k_{i,j} = \frac{mV^{k-1}_{i,j+1} + nV^k_{i,j-1} + V^{k-1}_{i+1,j} + V^k_{i-1,j}}{4}$$

where m and n are defined as in eqn. 5.11. The values of $V_{i,j+1}$ and $V_{i+1,j}$ are recalculated after $V_{i,j}$ on the k'th sweep, so their values from the $k-1$'th sweep are used in recalculating $V_{i,j}$. Both adding and subtracting $V_{i,j}^{k-1}$ to the right-hand side gives

$$V_{i,j}^{k} = V_{i,j}^{k-1} + \left[\frac{mV_{i,j+1}^{k-1} + nV_{i,j-1}^{k} + V_{i+1,j}^{k-1} + V_{i-1,j}^{k} - 4V_{i,j}^{k-1}}{4}\right]$$

The term in brackets is the residual, and would be zero when convergence has been reached. To obtain faster convergence, the residual is multiplied by a factor w (between 1.0 and 2.0) in calculating $V_{i,j}$.

$$V_{i,j}^{k} = V_{i,j}^{k-1} + w\left[\frac{mV_{i,j+1}^{k-1} + nV_{i,j-1}^{k} + V_{i+1,j}^{k-1} + V_{i-1,j}^{k} - 4V_{i,j}^{k-1}}{4}\right] \tag{5.14}$$

For the second case, on the axis of the PMT, eqn. 5.12 becomes

$$V_{i,1}^{k} = V_{i,1}^{k-1} + w\left[\frac{4V_{i,2}^{k-1} + V_{i+1,1}^{k-1} + V_{i-1,1}^{k} - 6V_{i,1}^{k-1}}{6}\right] \tag{5.15}$$

and for the case near the boundaries

$$V_{i,j}^{k} = V_{i,j}^{k-1} + w\left[\frac{aV_{i,j+1}^{k-1} + bV_{i,j-1}^{k} + cV_{i+1,j}^{k-1} + dV_{i-1,j}^{k}}{e} - V_{i,j}^{k-1}\right] \tag{5.16}$$

where a, b, c, d, e are defined as in eqn. 5.13.

Using the geometry of figure 5.1, with the photocathode and bottom flange grounded and the first dynode and electrode fixed at positive potential V_0, the potential at each point $V_{i,j}$ was recalculated using eqns. 5.14 - 5.16 for each sweep through the grid. The values $V_{i,j}$ were considered to have converged and the calculation ended when the residual at every point was less than a stipulated value V_{err}. So, with V_{err} set to a relatively large value of 1 Volt, the PMT potential was calculated for different values of the over-relaxation factor w to see which calculation converged soonest. It was found that a value of $w = 1.6$ gave the quickest convergence. For this value of w, V_{err} was set to 10^{-10} Volts and the potential recalculated to higher accuracy. This potential was then used when calculating the photoelectron trajectories.

5.4 Calculating the Electric Field in the PMT

The electric field $\vec{E}$ in the PMT is calculated from the potential using the expression

$$\begin{aligned} \vec{E} &= -\vec{\nabla} V(r,z) \\ &= -\frac{\partial V(r,z)}{\partial r} \cdot \tilde{r} \quad - \quad \frac{\partial V(r,z)}{\partial z} \cdot \tilde{z} \end{aligned} \tag{5.17}$$

where $\tilde{r}$ and $\tilde{z}$ are unit vectors pointing in the same directions as the r and z axes respectively. A two dimensional Taylor expansion is used to calculate the gradient of the potential off the grid points.

$$\frac{\partial V(r,z)}{\partial r} = \frac{\partial V(i,j)}{\partial r} + \frac{\partial^2 V(i,j)}{\partial r^2} \cdot (r-j) + \frac{\partial^2 V(i,j)}{\partial r \partial z} \cdot (z-i) \tag{5.18a}$$

$$\frac{\partial V(r,z)}{\partial z} = \frac{\partial V(i,j)}{\partial z} + \frac{\partial^2 V(i,j)}{\partial r \partial z} \cdot (r-j) + \frac{\partial^2 V(i,j)}{\partial z^2} \cdot (z-i) \tag{5.18b}$$

where (i,j) are the coordinates of the nearest grid point to (r,z). Table 5.1 gives the expressions used for the partial derivatives calculated on the grid points as derived from eqns. 5.6 - 5.9.

5.5 Solving the Differential Equations of Motion

To solve the three coupled second-order differential equations of motion 5.3, the Fourth-Order Runge-Kutta method was used. This method is commonly used in numerically solving differential equations and is well documented in most texts dealing with these techniques [Ge80], so only a brief description of it will be given here.

	Normal case $(r = p = q = s = 1)$	On axis of PMT	Near the boundary $(r \neq p \neq q \neq s)$
$\frac{\partial V_0}{\partial r}$	$\frac{V_1 - V_2}{2h}$	0	$\frac{r^2 V_1 + (p^2 - r^2) V_0 - p^2 V_2}{(r^2 p + p^2 r) h}$
$\frac{\partial V_0}{\partial z}$	$\frac{V_4 - V_3}{2h}$	$\frac{V_4 - V_3}{2h}$	$\frac{q^2 V_4 + (s^2 - q^2) V_0 - s^2 V_3}{(q^2 s + s^2 q) h}$
$\frac{\partial^2 V_0}{\partial r^2}$	$\frac{V_1 - 2V_0 + V_2}{h^2}$	$\frac{2V_0 - V_4 - V_3}{2h^2}$	$\frac{2}{h^2}\left[\frac{V_1}{p(p+r)} - \frac{V_0}{pr} + \frac{V_2}{r(p+r)}\right]$
$\frac{\partial^2 V_0}{\partial z^2}$	$\frac{V_4 - 2V_0 + V_3}{h^2}$	$\frac{V_4 - 2V_0 + V_3}{h^2}$	$\frac{2}{h^2}\left[\frac{V_4}{s(q+s)} - \frac{V_0}{qs} + \frac{V_3}{q(q+s)}\right]$
$\frac{\partial^2 V_0}{\partial r \partial z}$	$\frac{V_7 + V_6 - V_5 - V_8}{4h^2}$	0	$\frac{V_0 - V_8}{h^2} + \frac{\frac{\partial V_0}{\partial z} - \frac{\partial V_0}{\partial r}}{h}$ $+ \frac{\frac{\partial^2 V_0}{\partial z^2} + \frac{\partial^2 V_0}{\partial r^2}}{2}$

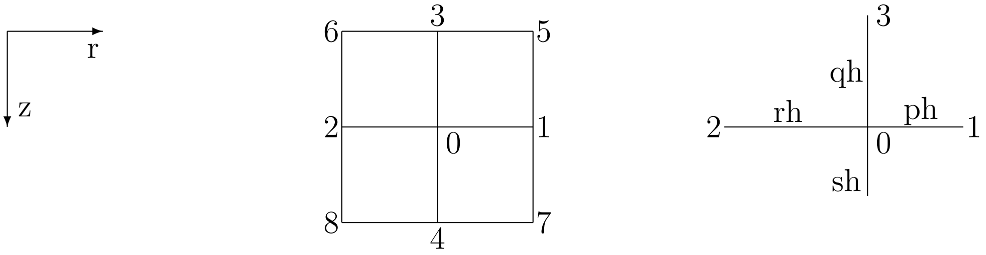

Table 5.1: Central difference approximations for the partial derivatives on the grid points.

The technique uses a step-wise method to solve first-order differential equations. It is applied here by splitting each second-order equation into two first-order equations. For example, eqn. 5.3a

$$\frac{d^2x}{dt^2} = \frac{q}{m}\left[\frac{-x}{\sqrt{x^2+y^2}}\frac{\partial V}{\partial r} + \frac{dy}{dt}B_z - \frac{dz}{dt}B_y\right]$$

is split into the two first-order equations

$$\begin{aligned} \frac{dx}{dt} &= x' && (5.19a) \\ \frac{dx'}{dt} &= \frac{q}{m}\left[\frac{-x}{\sqrt{x^2+y^2}}\frac{\partial V(x,y,z)}{\partial r} + y'B_z - z'B_y\right] \\ &= f(x,y,z,x',y',z') && (5.19b) \end{aligned}$$

where y' and z' are the time derivatives of y and z. The eqns. 5.3b and 5.3c are split in the same way.

The values of x and x' after a time step of Δt are then given by

$$x(t+\Delta t) = x(t) + \frac{1}{6}(k_{1_x} + 2k_{2_x} + 2k_{3_x} + k_{4_x}) \tag{5.20}$$

$$\begin{aligned} \text{where} \qquad k_{1_x} &= \Delta t \cdot x' \\ k_{2_x} &= \Delta t \cdot (x' + \frac{1}{2}k_{1_{x'}}) \\ k_{3_x} &= \Delta t \cdot (x' + \frac{1}{2}k_{2_{x'}}) \\ k_{4_x} &= \Delta t \cdot (x' + k_{3_{x'}}) \end{aligned}$$

and

$$x'(t+\Delta t) = x'(t) + \frac{1}{6}(k_{1_{x'}} + 2k_{2_{x'}} + 2k_{3_{x'}} + k_{4_{x'}}) \tag{5.21}$$

$$\begin{aligned} \text{where} \qquad k_{1_{x'}} &= \Delta t \cdot f_x(x, y, z, x', y', z') \\ k_{2_{x'}} &= \Delta t \cdot f_x(x + \frac{1}{2}k_{1_x}, y + \frac{1}{2}k_{1_y}, z + \frac{1}{2}k_{1_z}, x' + \frac{1}{2}k_{1_{x'}}, y' + \frac{1}{2}k_{1_{y'}}, z' + \frac{1}{2}k_{1_{z'}}) \\ k_{3_{x'}} &= \Delta t \cdot f_x(x + \frac{1}{2}k_{2_x}, y + \frac{1}{2}k_{2_y}, z + \frac{1}{2}k_{2_z}, x' + \frac{1}{2}k_{2_{x'}}, y' + \frac{1}{2}k_{2_{y'}}, z' + \frac{1}{2}k_{2_{z'}}) \\ k_{4_{x'}} &= \Delta t \cdot f_x(x + k_{3_x}, y + k_{3_y}, z + k_{3_y}, x' + k_{3_{x'}}, y' + k_{3_{y'}}, z' + k_{3_{z'}}) \end{aligned}$$

The k_{n_y}, k_{n_z}, $k_{n_{y'}}$ and $k_{n_{z'}}$ terms are defined in the same way as the x-terms in the eqns. 5.20 and 5.21. The values of all of the k_1 and $k_{1'}$ terms are calculated first, then the k_2 and $k_{2'}$ terms, and so on, until all the k and k' terms are known. The new values of x, y, z and x', y', z' are then calculated. To start the calculation, the initial position on the photocathode, energy and direction of motion is given for the photoelectron (*i.e.* x, y, z, x', y', z' at time $t = 0$). The new position and velocity are calculated after each time step Δt, until the photoelectron hits the first dynode or electrode. In this way, the photoelectrons are tracked, and the time and position of each collision with the dynode is calculated. Figure 2.3 shows the calculated equipotentials and several photoelectron trajectories for a potential of 800V applied between the photocathode and the first dynode and electrodes, and no magnetic field.

5.6 Calculating the Magnetic Field Effects

To calculate the effects of the magnetic field on the photoelectron collection efficiency and flight times, the published initial energy and angular distributions of the photoelectrons emitted from the photocathode are used. The energy distribution of photoelectrons generated by ∼650 nm light was deduced from shorter wavelength distributions measured by Nathan *et al.* [Na70] to be a Gaussian with a mean of 1/2 eV and a standard deviation of 1/6 eV.

$$N(E) = C \cdot exp\left[-18\left(E-\frac{1}{2}\right)^2\right] \qquad ; \quad 0 \leq E \leq 1\text{eV}$$

The angular distribution of photoelectrons from a bialkali photocathode could not be found, but often for other photocathode materials the distributions are Maxwellian [Br77]. Hence, the angular distribution used was

$$N(\theta) = C \cdot \frac{\theta}{\theta_m} \cdot exp\left[-\frac{1}{2}\left(\frac{\theta}{\theta_m}\right)^2\right]$$

where θ is the angle between the direction of emission and the normal to the surface. It was assumed that the photoelectrons are emitted with equal probability over all azimuthal angles. To determine the value of the parameter θ_m, a simulation of the experiment described in section 4.2 was performed. Using the energy distribution shown above, and a magnetic field strength and orientation as shown in figure 3.6, different values of θ_m were tried until the calculated photoelectron collection efficiency across the photocathode resembled the measured trigger rate of the PMT for red light. The trigger rate was used in the comparison because the photoelectron collection efficiency could not be directly measured. A value of $\theta_m = 20°$ was chosen as the best value (see figure 5.2). The trigger rate, however, depends on other factors besides the photoelectron collection efficiency. It also depends on the intensity of the light, the photoelectron generation efficiency and the gain of the multiplier. The light intensity could be reduced by dust or dirt which gets between the fibre-optic cable and the glass, by abrasions in the end of the cable caused by dragging it over the dusty glass, and by spot imperfections in the glass surface. The photoelectron generation efficiency for red light depends strongly on the presence of chemical impurities in

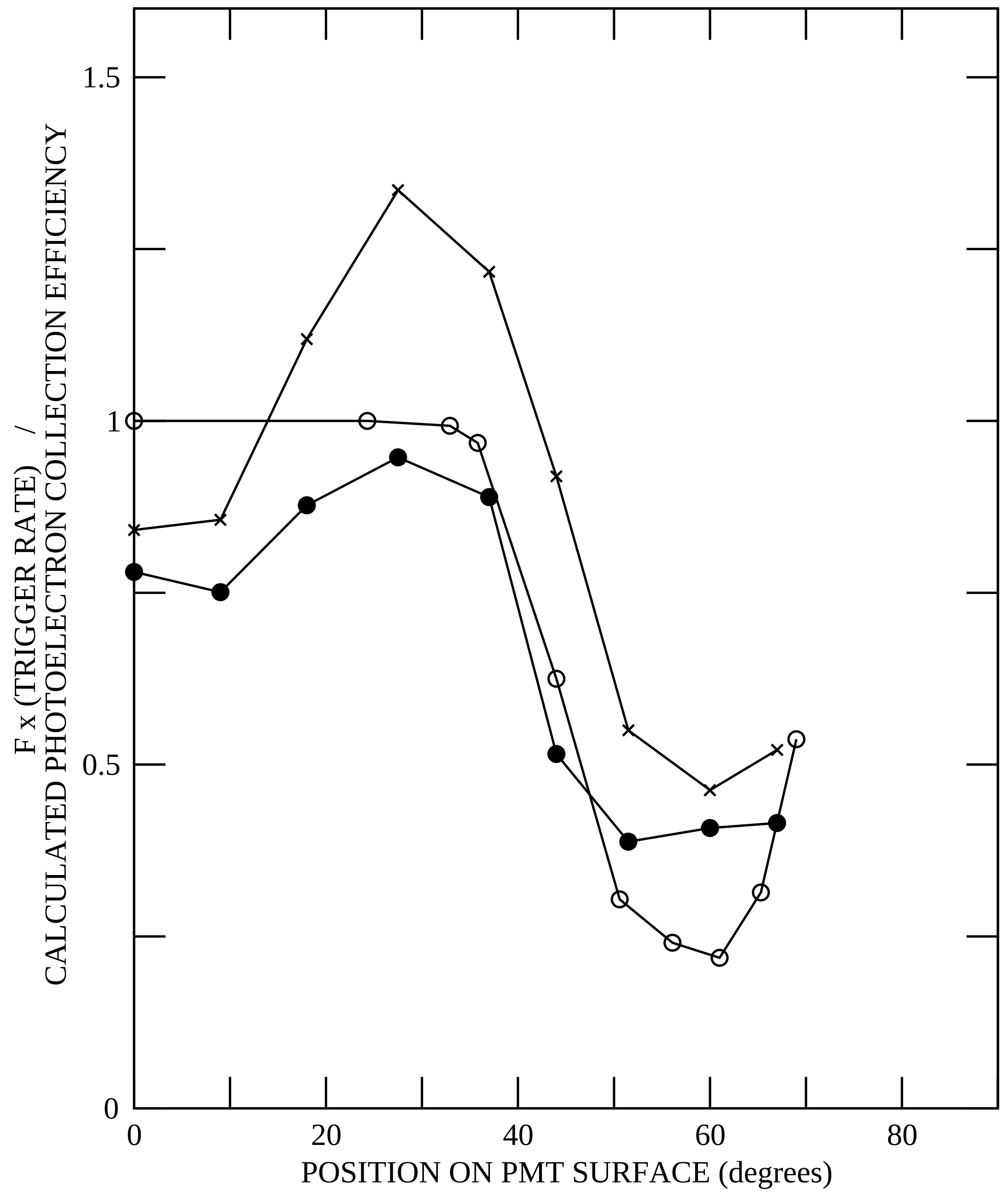

Figure 5.2: Comparison between the calculated photoelectron collection efficiency and the measured trigger rate over the photocathode surface of the R1449 PMT for the earth's magnetic field oriented as shown in figure 3.6. The hollow dots are for the calculated results, and the crosses and solid dots are for the scans perpendicular and parallel to the first dynode vanes, respectively. The lines are guides to the eye. The trigger rates are fit to the collection efficiencies by minimizing the χ^2 given by: $\chi^2 = \sum_i \left[\frac{F \cdot T_i - C_i}{\Delta T_i}\right]^2$ where T_i is the trigger rate measured at the i'th position on the PMT surface, C_i is the simulated photoelectron collection efficiency at the same position, ΔT_i is the uncertainty in T_i, and F is the free parameter whose value is determined in this calculation. Due to the effects of impurities on the photoelectron production rate, the fit does not include the data from the outside of the photocathode.

the photocathode, and the gain of the multiplier depends on the angle at which the photoelectrons strike the first dynode vanes. For these reasons, the calculations are not expected to closely match the data. However, the comparison is good enough to reasonably estimate θ_m.

From the same calculations, values of the photoelectron flight times and flight time spreads were obtained as a function of the photoelectron's starting position on the photocathode. The results of the calculations are shown in figure 5.3. The calculated average flight time from the various points on the photocathode surface varied between 44.2 nsec and 45.9 nsec, and the calculated flight time spread at each point varied between 1 nsec and 2.8 nsec. These results are discussed in the next chapter.

A measurement of the relative efficiency of PMT #ZW4673 was done using a ^{241}Am α-source coupled to a Pilot U plastic scintillator as the light source [Le87]. This source emits bursts of thousands of photons with wavelengths centred around 390 nm. The amplitude of the PMT output pulse is proportional to

$$\begin{aligned}\text{pulse amplitude} \quad \propto \quad & (\text{ \# photons incident on PMT}) \\ & \times (\text{photoelectron production eff. / photon}) \\ & \times (\text{photoelectron collection eff.}) \\ & \times (\text{gain of multiplier})\end{aligned}$$

Figure 5.4 shows the peak position in the pulse height spectrum for photoelectrons generated at various locations on the photocathode. The PMT was positioned as described in section 3.5.1, and scans were made parallel and perpendicular to the

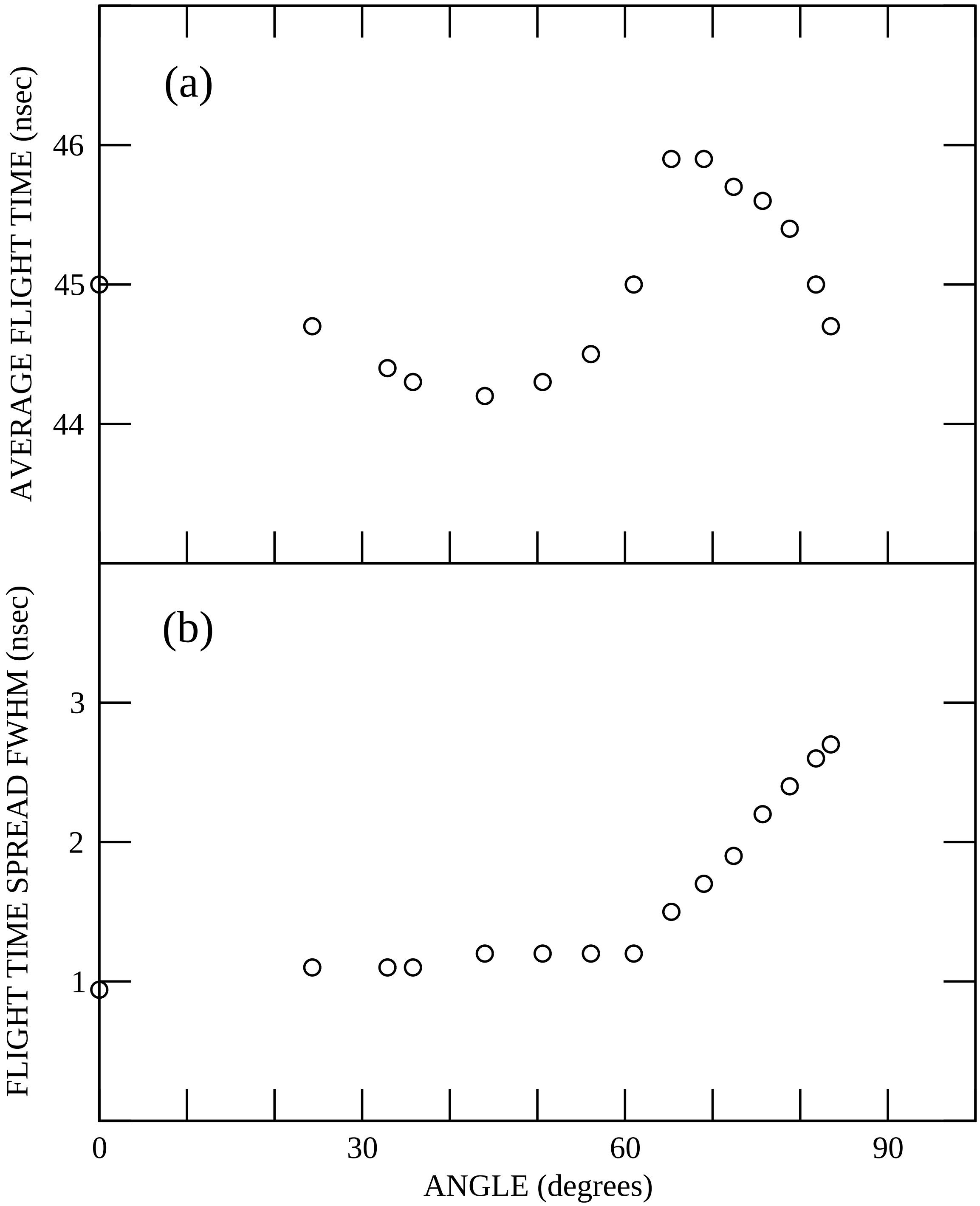

Figure 5.3: The simulated spot flight time (a), and flight time spread fwhm (b) of the photoelectrons for 800V applied between the photocathode and first dynode of the R1449 PMT, and the earth's magnetic field oriented as shown in figure 3.6.

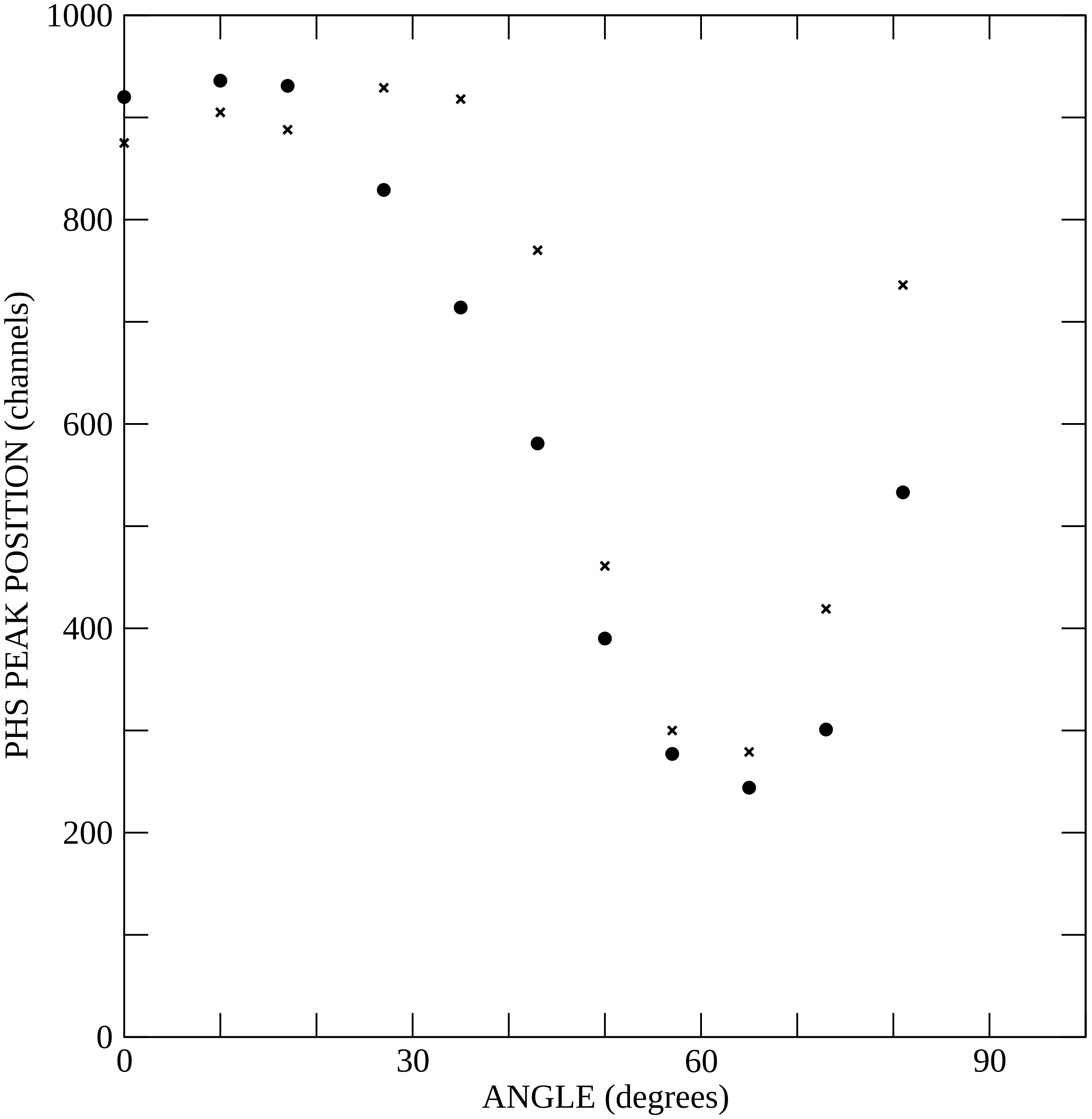

Figure 5.4: The peak position in the pulse height spectrum as a function of the position of the α-source/scintillator light source on the photocathode. The crosses and dots are for the scans perpendicular and parallel to the first dynode vanes, respectively. The earth's magnetic field was oriented as shown in figure 3.6 (data from [Le87]).

first dynode vanes. There are differences in the peak positions between the two scans, probably due to changes in the first dynode gain with differing angles of incidence of photoelectrons on the tilted vane surfaces. The plot shows a dip of the same size and at the same position as that calculated in the simulations, indicating that the calculations are reasonably accurate. The measured pulse amplitudes between $\theta = 70°$ and 85° are not as high as expected from the simulation calculations. This is most likely due to a drop in the photoelectron generation efficiency, as the photocathode is probably thinner near the outside. As expected, no effects of chemical impurities were observed with the ultraviolet light.

With these energy and angular photoelectron emission distributions, the next step was to calculate what magnetic field strengths could be tolerated before the PMT's collection efficiency dropped significantly, to determine how well the earth's magnetic field would have to be compensated for at the SNO detector site. So, for 800V applied between the photocathode and first dynode, and with the photoelectrons generated at random locations over the photocathode surface, photoelectron collection efficiencies were calculated for 0.5 gauss magnetic fields oriented at various angles with respect to the long axis of the PMT (see figure 5.5). The collection efficiency was the lowest at 62% for the magnetic field oriented perpendicular to the long axis of the PMT (parallel to the first dynode).

Finally, for photoelectrons generated randomly over the whole photocathode and with 800V applied between the photocathode and first dynode, the worst case photoelectron collection efficiencies and flight time spreads were calculated for various strengths of magnetic fields oriented parallel to the first dynode (see figure 5.6). The

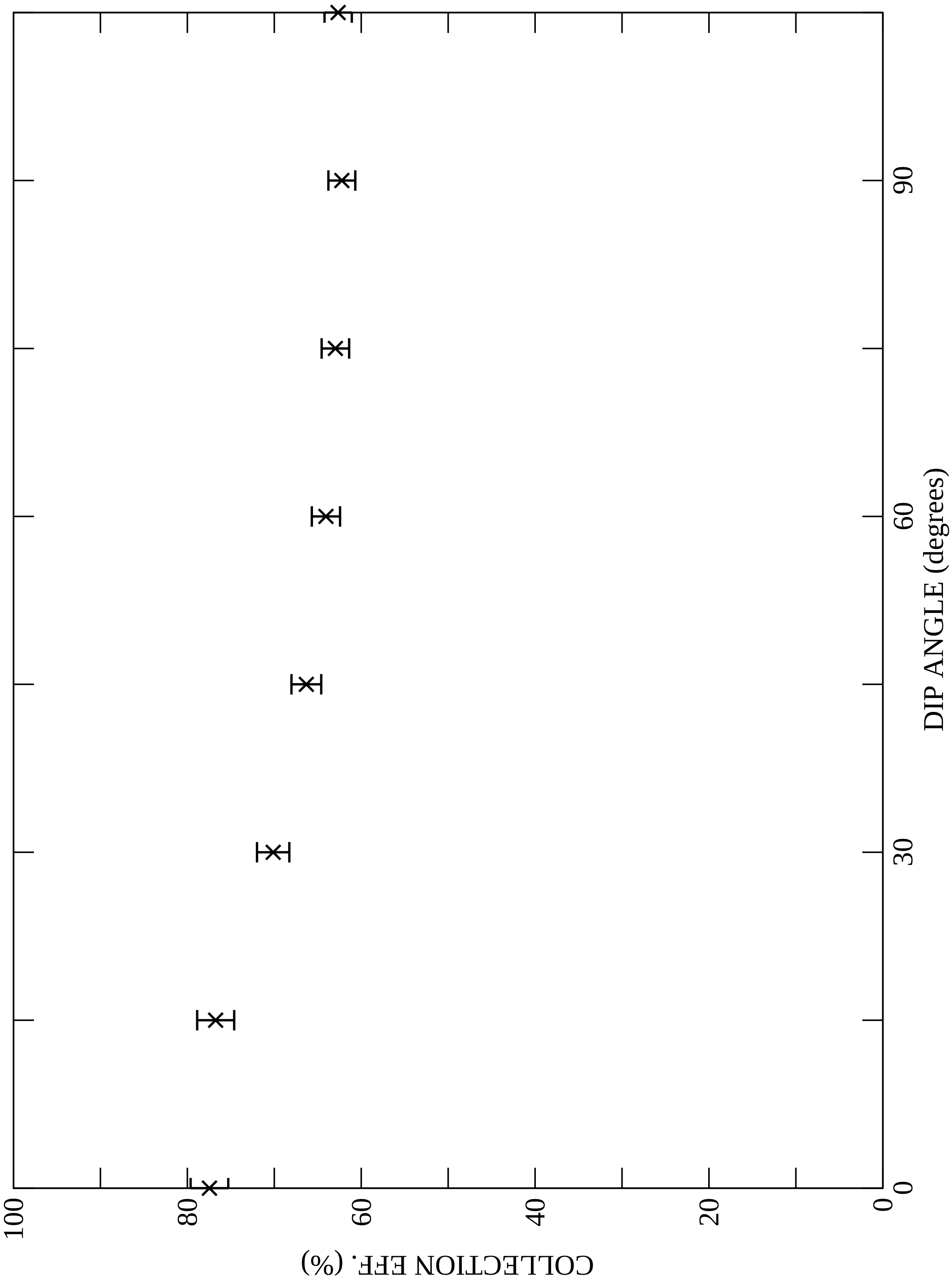

Figure 5.5: Monte Carlo simulation of the photoelectron collection efficiency for a 0.5 gauss magnetic field oriented at various dip angles with respect to the long axis of the R1449 PMT. Photoelectrons were emitted uniformly over the entire photocathode.

results indicate that if the magnetic field at the SNO detector is reduced to less than 0.1 gauss (20% of the earth's magnetic field), the photoelectron collection efficiency of any PMT will not drop below 95% of its zero field efficiency.

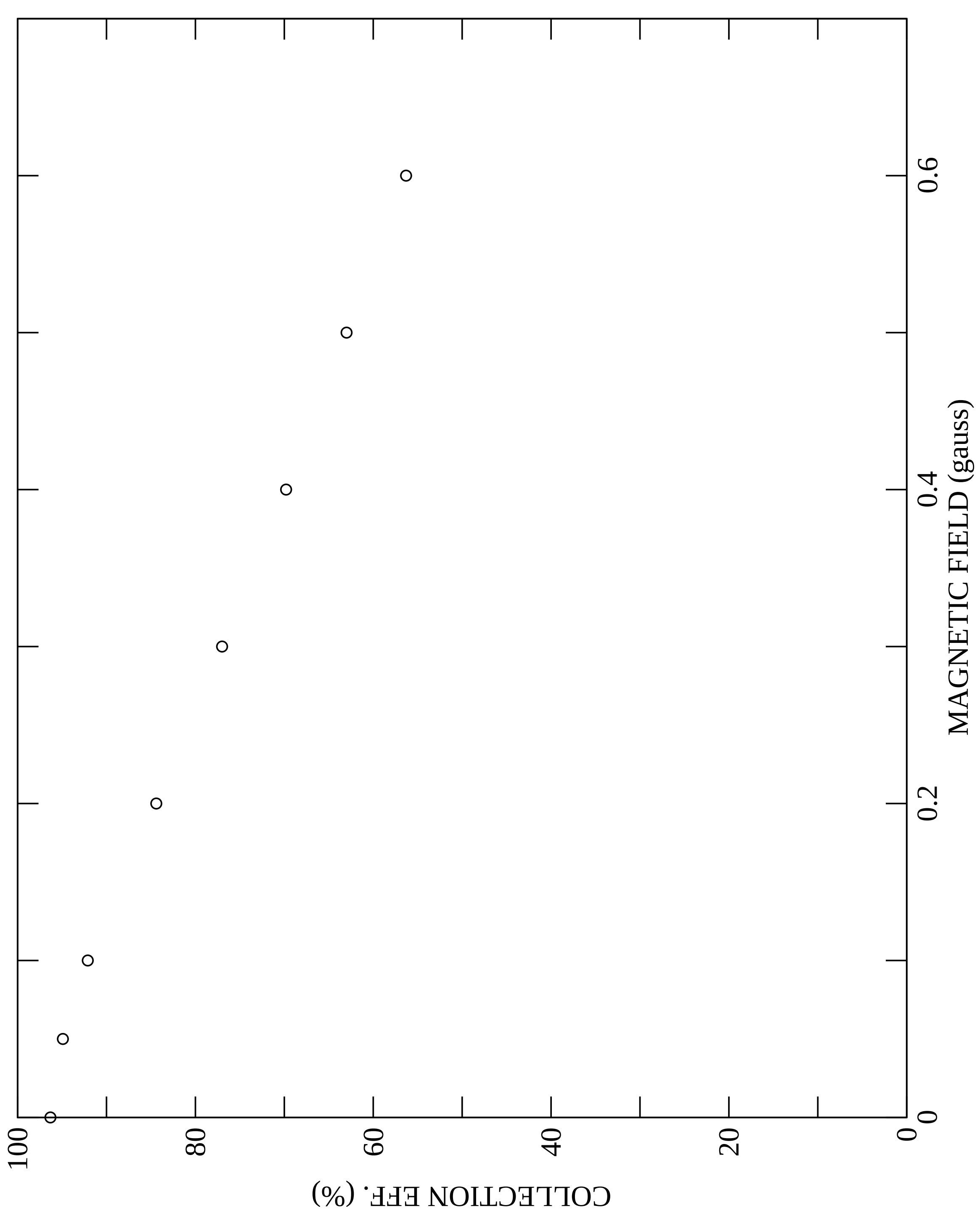

Figure 5.6: Monte Carlo simulation of the photoelectron collection efficiency for various strengths of magnetic field oriented parallel to the first dynode. Photoelectrons were emitted uniformly over the entire photocathode.

Chapter 6

Discussion

The light pulser constructed to trigger the PMT's emitted red light pulses ($\lambda \approx 650 \pm 10$ nm fwhm) whose widths were ≤ 1.9 nsec fwhm. These pulses are short enough to allow accurate measurement of the 20″ PMT's TTS, but their wavelengths fall within the tail-end of the PMT's spectral response. It is expected that the TTS will increase with the incident photon energy [Mo77], so that the timing response measured here might be a 'best case' result. Also, the quantum efficiency of the PMT was found to be very sensitive to photocathode non-uniformities for red light, whereas it was found to be more uniform for ultraviolet light. Thus, if a tube-testing facility is set up for the SNO project, it is recommended that a light pulser which can emit ultraviolet light be used.

The single photoelectron pulse height spectra of the 20″ PMT showed no peak, indicating poor energy resolution. Single and multiple photoelectron pulses could not be distinguished, nor could either be distinguished from any of the PMT noise. Thus, initially, every PMT pulse in the SNO detector would have to be assumed to be generated by a single Čerenkov photon.

The PMT dark noise rate above the 1/4 p.e. level was measured to be about

8 kHz. This dark noise can adversely affect the performance of the SNO detector in two ways. PMT's triggering on random noise during a valid event can degrade the accuracy of the vertex reconstruction, and they can degrade the energy resolution by adding a variable number of counts to the number of valid PMT triggers. It is expected that about 2000 PMT's would be used in the SNO detector, and reconstruction would start with all PMT triggers in a 100 nsec time window [Sn87]. The number of random noise triggers in this window can be approximated using a Binomial distribution:

$$\begin{aligned} P(n) &= \frac{N!}{(N-n)!n!} \cdot (1-e^{-r\tau})^{n} \cdot (e^{-r\tau})^{N-n} \\ \text{where} \quad n &= \text{\# random PMT triggers} \\ \tau &= \text{time window } (=100 \text{ nsec}) \\ r &= \text{random PMT noise rate} \\ N &= \text{\# PMT's in detector } (\approx 2000) \\ P(n) &= \text{probability of } n \text{ PMT's triggered by noise in time } \tau \end{aligned}$$

Using the measured dark noise rate of 8 kHz, the average number of random PMT triggers in the time window will be $Nr\tau = 1.6$. The expected threshold for analysis is about 24 PMT's [Sn87], far larger than the average number of random PMT nose triggers. Also, for the vertex reconstruction a final time window of 30 nsec would be used, and this would screen out most PMT triggers due to noise. Thus, a noise rate of 8 kHz is not expected to appreciably degrade the accuracy of the reconstructions.

There is a probability that enough PMT's will be triggered by noise to simulate an event and trigger the data collection hardware. For a trigger threshold of m

PMT's, the rate at which this will occur is:

$$R(m) = Nr \cdot \sum_{n=m-1}^{2000} P(n)$$

where N, r and $P(n)$ are defined as above. From estimates of the low energy background in the SNO detector, the threshold for triggering the data collection hardware will probably be about 18 PMT triggers [Sn87]. At this threshold level, the expected rate of noise events caused by PMT dark counts is 2.4 per day, which is reasonably low.

Because of the difference in conditions between the test facility here and the SNO detector, the PMT dark noise rate will not be the same in both cases. If the magnetic fields are eliminated at the detector site, then from figures 5.5 and 5.6, one sees that the increase in the photoelectron collection efficiency will also bring about a 50% increase in the dark noise rate. However, the dark noise rate of 8 kHz was measured at a temperature of about 25°C, while it is expected that the water in the SNO detector will be cooled to 10°C. Measurements by Hamamatsu have shown that the PMT noise rate falls by a factor of two or three between the two temperatures [Ku83]. Thus, 8 kHz is a conservative estimate to use in the previous calculations. However, it is still low enough to be acceptable.

There were no measurable differences in the timing properties of the 20″ PMT when the cathode-grounded and anode-grounded voltage dividers were used. However, when using the anode ground scheme, the dark noise rate of both PMT's suddenly increased (>50 kHz) after a few months of operation. The noise rates returned to normal levels after the cathode ground scheme was implemented, indicating that the problem was due to ohmic leakage through the glass envelope and that the photocathodes should be ground if the bias is to be applied for long periods of time. The cathode ground scheme also has the advantage that only one cable need be run to each PMT, as the signal is picked off the power cable. Thus, fewer cables would be needed, and there would be less chance of failure at the waterproof interface between cables and PMT's.

The best timing resolution of 6.5 nsec fwhm for spot illumination at the centre of the photocathode was obtained using double constant fraction (DCF) timing with the 100 MHz storage oscilloscope. The advantage of using a storage oscilloscope to visually examine the pulses is that one obtains 'true' constant fraction timing, independent of pulse risetime variations. Also, with DCF timing, the zero-extrapolated pulse arrival time is less sensitive to pulse shape changes than the trigger time for single CF timing. As there was substantial improvement in the timing resolution of the 20″ PMT with DCF timing over single CF timing, there must have been significant pulse shape variations from the PMT. Using DCF timing in the SNO detector, however, would entail a substantial increase in the size and cost of the discriminator electronics.

The best spot timing resolution measured at the photocathode centre with the Ortec 584 CFD was 9.2 nsec fwhm. This result was obtained at a high timing amplifier gain / high discriminator level setting, indicating that the timing jitter of the system was affected more by the CFD than the TFA. A spot timing resolution of 9.5 nsec fwhm using the LEAC technique was measured with the Ortec 584 timing unit. This is only marginally worse than the best result obtained with the CFD. So, if the

Hamamatsu R1449 PMT is chosen for the SNO detector, it is recommended that the LEAC technique be used as well, as the savings in cost and space of the discriminator electronics would justify the slight decrease in timing resolution.

The TTD over the surface of the PMT was measured in the first part of the experiment to vary over ±2 nsec. This is consistent with the results obtained with the storage oscilloscope, which showed that the TTD varies by less than 4 nsec. The measurements of the timing resolution for spot illumination on the PMT surface using CFD and LEAC timing techniques were in agreement with each other, and showed that the resolution over the photocathode surface varies between 8.7 and 14 nsec fwhm. Combining the TTD and spot timing resolution results indicates that the timing resolution for full photocathode illumination is about 10.4 nsec fwhm. This is substantially worse than the 7.0 nsec fwhm quoted by Hamamatsu [Ku83]. Some possible sources of the discrepancy are: 1) the PMT used (#ZW4706) might have had a poor timing response due to a misaligned multiplier structure, dynode and anode non-uniformities, etc., 2) the timing jitter in our electronics might have been worse, or 3) the earth's magnetic field was not compensated for during our measurements, and so it could have significantly degraded the timing response of the multiplier by causing the electrons to deviate from their normal paths between dynodes. Fortunately, it is unlikely that any of these would seriously affect the results of the comparison between the timing discriminators.

The photoelectron flight path simulations have shown that the main effect of a weak magnetic field is to reduce the photoelectron collection efficiency, without significantly affecting the flight times. It was calculated that if the magnetic field at the SNO detector was reduced to less than 0.1 gauss, the photoelectron collection efficiency of the R1449 PMT would not drop below 95% of its zero field efficiency. All of the flight path simulations were performed with the photoelectron initial energy and angular distributions obtained for red light, whereas the light detected in the SNO detector will mostly be in the ultraviolet range. However, the results of the measurements performed with the α-source and scintillator, which emits mostly ultraviolet light, closely matched the calculated photoelectron collection efficiencies for the red light. This indicates that the results of the calculations of the magnetic field effects on the PMT efficiency will still apply for the conditions in the SNO detector. These calculations, however, do not include effects in the dynodes, where the magnetic field will cause the secondary electrons to deviate from their normal paths, and thus degrade the overall efficiency and timing response of the PMT. Because of this, it is possible that more magnetic field compensation will be needed than was calculated here.

In magnetic fields less than or equal to that of the earth's, the calculated flight time spread for full photocathode illumination is about 2 nsec fwhm. The small spread shows that the geometry of the photocathode, focussing electrode and first dynode is very well designed, and that most of the TTS of the PMT is introduced by the electron multiplier. This is not unexpected, in that the venetian blind multiplier is noted for its poor timing properties. It is also responsible for the large variations in the gain of the PMT for photoelectrons starting at different points on the photocathode, and for the poor single photoelectron response, as the yield of secondary electrons from the first dynode strongly depends on the angle at which the photoelectrons strike the vanes. To overcome these problems, Hamamatsu has recently developed a new 20″ PMT (R1449Z) which has the same glass envelope, but has a smaller 13 stage venetian blind multiplier. Although this is expected to improve the timing performance and the uniformity of the gain of the PMT, it has the disadvantage that the size of the photoelectron collection area had been reduced to 2″ in diameter. This means that the photoelectron collection efficiency will be lower and more sensitive to magnetic fields. Hence, it is possible that the new PMT might not improve the energy and directional resolution of the SNO detector as expected, if its efficiency is too low.

Chapter 7

Conclusions

A characterization of the Hamamatsu R1449 20″ PMT was performed so that its suitability for the SNO heavy water Čerenkov detector could be determined. Measurements of the TTS of the R1449 PMT were performed using various timing techniques to determine which gives the best timing resolution. The dark noise rate of the PMT was measured to determine if it is low enough to ensure that true signals from the heavy water will not be buried in PMT noise, and the single photoelectron response of the PMT was measure to determine if the signals generated by the Čerenkov light can be distinguished from some of the PMT noise based on pulse height. In addition, photoelectron trajectories were simulated by computer to determine their contribution to the TTS, and to gauge the effects of magnetic fields on the timing and efficiency of the PMT.

The tests were performed at the single photoelectron level, using a weak pulsed light source of wavelength 650±10 nm (fwhm), and pulse width $\leq$1.9 nsec fwhm. There was no single photoelectron peak observed in the pulse height spectra, making it impossible to distinguish between noise, single and multiple photoelectron pulses based on pulse amplitude. The TTS for full photocathode illumination was determined to be about 10.4 nsec, substantially worse than the 7.0 nsec quoted by Hamamatsu [Ku83]. However, it is recommended that the tests be repeated with a pulser that can emit ultraviolet light and with the earth's magnetic field compensated for, to more accurately simulate the conditions in the SNO detector.

The dark noise rate above the 1/4 p.e. level was measured to be ~8 kHz, which is acceptable for the SNO project. This rate will decrease by a factor of two to three in the heavy water detector due to the lower temperature there, and will increase by a factor of one and one half due to the magnetic field compensation. The net effect on the nose rate will be a decrease of 25% - 50%. It is recommended that the LEAC timing technique be used for determining pulse arrival times. Its timing performance was found to be only marginally worse than the CF technique. The electronics for the LEAC technique, however, are much simpler than that for the CF technique, and the trigger efficiency is higher. To minimize the timing jitter of the electronics, a combination of high TFA gain / high timing discriminator level should be used, since most of the jitter comes from the discriminator.

From the computer simulations of the photoelectron trajectories, it was found that the flight time spread of photoelectrons accelerated over 800V is ~2 nsec fwhm, which is only a small component of the TTS of ~10.4 nsec. In addition, it was found that the main effect of a weak magnetic field is to reduce the photoelectron collection efficiency without significantly affecting the flight times. The main design problem with the R1449 PMT is that a large first dynode area is needed for efficient photoelectron collection, which precludes all but the venetian blind design for the electron multiplier. However, the venetian blind multiplier is noted for its poor timing resolution, and large changes in gain with changes in the angle of incidence of the photoelectrons, and is responsible for the pulse shape variations that degrade the performance of the single timing discriminators. To improve the timing performance of the PMT, a smaller (faster) electron multiplier is needed, along with better focussing of the photoelectrons onto the smaller first dynode.

Hamamatsu has developed a new model of the 20″ PMT, the R1449Z, with a smaller venetian blind multiplier, but with essentially the same focussing electrode structure. The photoelectron simulations for the old geometry, however, indicate that the smaller first dynode area will result in reduced PMT efficiency. It will probably be necessary to redesign the electrodes as well, to improve the focussing of the photoelectrons.

Appendix

```
      PROGRAM TUBPT3
C     This program calculates the potential in the 20" Hamamatsu
C     phototubes using the successive over-relaxation technique.
C
      IMPLICIT REAL*8 (A-H,O-Z)
      INTEGER BOUND,FLAG,COUNT
      BYTE NAME(16)
C
      VIRTUAL U(141,101)
C
      COMMON /MISC/ NAME,BOUND(141,5),ERROR,W,COUNT,V
      COMMON /STAR/ P,Q,R,S
C
      CALL FILRD3
C
      COUNT=0
C
      DO 3 I=1,141
         DO 2 J=1,101
            U(I,J)=0.0D0
            IF(J.GE.BOUND(I,4) .AND. J.LE.BOUND(I,5)) U(I,J)=V
 2       CONTINUE
 3    CONTINUE
C
 10   CONTINUE
      FLAG=0
      COUNT=COUNT+1
      DO 30 I=140,2,-1
         DO 20 J=BOUND(I,1),BOUND(I,2)
            IF(J.GE.BOUND(I,4) .AND. J.LE.BOUND(I,5)) GO TO 20
            IF(J.GT.1) GO TO 11
              RES=(4.0D0*U(I,2)+U(I+1,1)+U(I-1,1)-6.0D0*U(I,1))/6.0D0
              GO TO 13
C
 11         IF(J.GE.BOUND(I,3)) GO TO 12
```

```
                RES=U(I,J-1)*(1.0D0-0.5D0/(J-1))+U(I,J+1)*(1.0D0+0.5D0/(J-1))
                RES=(RES+U(I+1,J)+U(I-1,J)-4.0*U(I,J))/4.0D0
                GO TO 13
C
 12             CALL PQRS3(I,J)
                UP=0.0D0
                IF(P .GE. 1) UP=U(I,J+1)
                UQ=0.0D0
                IF(Q .GE. 1) UQ=U(I-1,J)
                UR=U(I,J-1)
                US=0.0D0
                IF(S .GE. 1) US=U(I+1,J)
                RES=((2.0D0+R/(J-1))*UP/P+(2.0D0-P/(J-1))*UR/R)/(P+R)
                RES=RES+(2.0D0*UQ/Q+2.0D0*US/S)/(Q+S)
                RES=RES/(2.0D0/(P*R)+2.0D0/(Q*S)-(P-R)/(P*R*(J-1)))-U(I,J)
C
 13           CONTINUE
              U(I,J)=U(I,J)+W*RES
              IF(ABS(RES).GE.ERROR) FLAG=1
 20        CONTINUE
 30     CONTINUE
        IF(FLAG.NE.0) GO TO 10
C
        CALL ASSIGN(2,NAME,0)
        WRITE(2,*) V,W,ERROR
        WRITE(2,*) COUNT
        DO 40 I=1,141
           WRITE(2,*)(U(I,J),J=1,BOUND(I,2))
 40     CONTINUE
        CALL CLOSE(2)
C
        END
C
C       ****************************************************************
C
        SUBROUTINE FILRD3
C       This routine reads the inputs for TUBPT3 from the data
C       file TUBDT3.DAT.
C
        IMPLICIT REAL*8 (A-H,O-Z)
        INTEGER BOUND,COUNT
        BYTE NAME(16)
        LOGICAL*1 ERR
C
        COMMON /MISC/ NAME,BOUND(141,5),ERROR,W,COUNT,V
```

```
C
        CALL ASSIGN(1,'DK:TUBDT3.DAT',0)
        CALL GETSTR(1,NAME,15,ERR)
        READ(1,*) V
        READ(1,*) W
        READ(1,*) ERROR
        DO 10 I=1,141
           READ(1,*)(BOUND(I,J),J=1,5)
 10     CONTINUE
C
        CALL CLOSE(1)
        RETURN
        END
C
C       ****************************************************************
C
        SUBROUTINE PQRS3(I,J)
C       This routine calculates the length of the branches of the
C       star for the program TUBPT3.
C
        IMPLICIT REAL*8 (A-H,O-Z)
C
        COMMON /STAR/ P,Q,R,S
C
        IF(I.LE.33) GO TO 1
        IF(I.GE.34 .AND. I.LE.74) GO TO 2
        IF(I.GE.75 .AND. I.LE.129) GO TO 3
        IF(I.GE.130) GO TO 4
C
  1     P=1.0D0+DSQRT(1.5376D4-(1.25D2-I)**2)-J
        Q=I-1.25D2+DSQRT(1.5376D4-(J-1.0D0)**2)
        S=1.0D0
        GO TO 5
C
  2     P=4.2D1+DSQRT(3.481D3-(7.42D1-I)**2)-J
        Q=I-7.42D1+DSQRT(3.481D3-(4.2D1-J)**2)
        S=1.0D0
        GO TO 5
C
  3     P=4.2D1+DSQRT(3.481D3-(7.42D1-I)**2)-J
        Q=1.0D0
        S=7.42D1+DSQRT(3.481D3-(4.2D1-J)**2)-I
        GO TO 5
C
  4     P=7.8D1-DSQRT(7.84D2-(1.53D2-I)**2)-J
```

```
      Q=1.0D0
      S=1.53D2-DSQRT(7.84D2-(7.8D1-J)**2)-I
C
 5    IF(P.GE.1.0D0) P=1.0D0
      IF(Q.GE.1.0D0) Q=1.0D0
      R=1.0D0
      IF(S.GE.1.0D0) S=1.0D0
C
      RETURN
      END
```

```
        PROGRAM ELTRJ4
C       This program calculates the trajectories of electrons in the
C       20" Hamamatsu phototubes using a potential calculated by
C       the routine TUBPT3.  The differential equations of motion
C       for the electron are solved using the Fourth-order Runge-
C       Kutta method.
C
        IMPLICIT REAL*8 (A-H,O-Z)
        INTEGER BOUND
        BYTE NAME(16),Q
        LOGICAL*1 ERR
C
        VIRTUAL U(141,101)
C
        COMMON /BOUND/ BOUND(141,5)
        COMMON /STATUS/ ELCTRN(7,2)
        COMMON /TIME/ T,DT
        COMMON /HIT/ XHIT,YHIT,RHIT,THIT,POL,AZI
        COMMON /MAG/ BX,BY,BZ
        COMMON /POT/ VV,VR
C
        CALL RDFIL4
C
        WRITE(7,*)' ENTER THE FILENAME WITH THE POTENTIAL ARRAY'
        CALL GETSTR(7,NAME,15,ERR)
        CALL ASSIGN(1,NAME,0)
        READ(1,*) VR,W,ERROR,M
        DO 5 I=1,141
           READ(1,*)(U(I,J),J=1,BOUND(I,2))
  5     CONTINUE
        CALL CLOSE(1)
C
 10     CONTINUE
        CALL ELINT4
 20     CONTINUE
        CALL STEP4(U)
        E1=ELCTRN(1,1)/2.0D0
        E2=ELCTRN(2,1)/2.0D0
        E3=(ELCTRN(3,1)+1.0D0)/2.0D0
        WRITE(2,25) T,E1,E2,E3
 25     FORMAT(1X,F6.2,5X,F6.2,5X,F6.2,5X,F6.2)
        CALL PSCHK4(IPC)
        GO TO (20,30,40,50,60),IPC
C
 30     CONTINUE
```

```
      WRITE(7,*)' ELECTRON HIT ELECTRODE'
      WRITE(2,*)' ELECTRON HIT ELECTRODE'
      GO TO 80
C
 40   CONTINUE
      WRITE(7,*)' ELECTRON PASSED OUTSIDE OF ELECTRODE'
      WRITE(2,*)' ELECTRON PASSED OUTSIDE OF ELECTRODE'
      GO TO 80
C
 50   CONTINUE
      WRITE(7,*)' ELECTRON HIT DYNODE'
      WRITE(2,*)' ELECTRON HIT DYNODE'
 51   CONTINUE
      WRITE(7,*)' TIME OF HIT IS:  (nsec)'
      WRITE(7,52) THIT
      WRITE(2,52) THIT
 52   FORMAT(10X,'T=',F5.2)
      WRITE(7,*)' POSITION OF HIT IS:  (cm)'
      WRITE(7,53) XHIT,YHIT
      WRITE(2,53) XHIT,YHIT
 53   FORMAT(10X,'X=',F5.2,/,10X,'Y=',F5.2)
      WRITE(7,*)' ANGLE OF HIT IS:  (degrees)'
      WRITE(7,54) POL,AZI
      WRITE(2,54) POL,AZI
 54   FORMAT(10X,'POLAR ANGLE=',F6.1,/,10X,'AZIM. ANGLE=',F6.1)
      GO TO 80
C
 60   CONTINUE
      WRITE(7,*)' ELECTRON HIT ELECTRODE'
      WRITE(2,*)' ELECTRON HIT ELECTRODE'
      GO TO 51
C
 80   CONTINUE
      CALL CLOSE(2)
      WRITE(7,*)' DO YOU WISH TO TRACK ANOTHER ELECTRON (Y/N)?'
      READ(7,90) Q
 90   FORMAT(A1)
      IF(Q .EQ. 'Y') GO TO 10
C
      END
C
C     ****************************************************************
C
      SUBROUTINE RDFIL4
C     This routine reads the tube parameters from the file
```

```
C       TUBDT3.DAT for the routine ELTRJ4.
C
        IMPLICIT REAL*8 (A-H,O-Z)
        INTEGER BOUND
        BYTE NAME(16)
        LOGICAL*1 ERR
C
        COMMON /BOUND/ BOUND(141,5)
        COMMON /MAG/ BX,BY,BZ
        COMMON /POT/ VV,VR
C
        CALL ASSIGN(1,'DK:TUBDT3.DAT',0)
        CALL GETSTR(1,NAME,15,ERR)
        READ(1,*) VV,W,ERROR
        DO 10 I=1,141
           READ(1,*)(BOUND(I,J),J=1,5)
 10     CONTINUE
        READ(1,*) BX,BY,BZ
        CALL CLOSE(1)
C
        RETURN
        END
C
C       ****************************************************************
C
        SUBROUTINE ELINT4
C       This routine prompts the user for the initial position and
C       energy of the electron, the time step size and the output
C       file name.  This routine is called by program ELTRJ4.
C
        IMPLICIT REAL*8 (A-H,O-Z)
        BYTE NAME1(16)
        LOGICAL*1 ERR
C
        COMMON /STATUS/ ELCTRN(7,2)
        COMMON /TIME/ T,DT
C
        WRITE(7,*)' ENTER THE INITIAL Z-COORD. OF THE ELECTRON'
        READ(7,*) ZSTART
        WRITE(7,*)' ENTER THE INITIAL ENERGY OF THE ELECTRON (eV)'
        READ(7,*) ENIN
        WRITE(7,*)' ENTER THE INITIAL ANGLES OF MOTION (degrees)'
        READ(7,*) POLIN,AZIN
        WRITE(7,*)' ENTER THE TIME STEP SIZE (nsec)'
        READ(7,*) DT
```

```
      WRITE(7,*)' ENTER THE OUTPUT FILE NAME'
      CALL GETSTR(7,NAME1,15,ERR)
      CALL ASSIGN(2,NAME1,0)
      WRITE(2,*) ZSTART,ENIN,POLIN,AZIN,DT
C
      IF(ZSTART .NE. 1.0D0) GO TO 5
      RSTART=1.0D0
      CTH=0.0D0
      STH=1.0D0
      GO TO 15
  5   CONTINUE
      IF(ZSTART.GE.33.682D0) GO TO 10
      RSTART=1.0D0+DSQRT(1.5376D4-(1.25D2-ZSTART)**2)
      RSTRTP=(1.25D2-ZSTART)/DSQRT(1.5376D4-(1.25D2-ZSTART)**2)
      GO TO 14
 10   CONTINUE
      RSTART=4.2D1+DSQRT(3.481D3-(7.42D1-ZSTART)**2)
      RSTRTP=(7.42D1-ZSTART)/DSQRT(3.481D3-(7.42D1-ZSTART)**2)
 14   CONTINUE
      THETA=DATAN(RSTRTP)
      CTH=DCOS(THETA)
      STH=DSIN(THETA)
 15   CONTINUE
      V0=DSQRT(ENIN)*2.372378D-1
      POLIN=POLIN/57.29577951D0
      AZIN=AZIN/57.29577951D0
      TEMP=-CTH*DCOS(POLIN)+STH*DSIN(POLIN)
      VXSTRT=V0*DCOS(AZIN)*TEMP
      VYSTRT=V0*DSIN(AZIN)*TEMP
      VZSTRT=V0*(STH*DCOS(POLIN)+CTH*DSIN(POLIN))
C
      T=0.0D0
C
      ELCTRN(1,1)=RSTART-1.0D0
      ELCTRN(2,1)=0.0D0
      ELCTRN(3,1)=ZSTART
      ELCTRN(4,1)=RSTART
      ELCTRN(5,1)=VXSTRT
      ELCTRN(6,1)=VYSTRT
      ELCTRN(7,1)=VZSTRT
C
      E1=ELCTRN(1,1)/2.0D0
      E2=ELCTRN(2,1)/2.0D0
      E3=(ELCTRN(3,1)+1.0D0)/2.0D0
      WRITE(2,20) T,E1,E2,E3
```

```
 20     FORMAT(1X,F6.2,5X,F5.2,5X,F5.2,5X,F5.2)
C
        RETURN
        END
C
C       ****************************************************************
C
        SUBROUTINE STEP4(U)
C       This routine uses the Fourth-order Runge-Kutta method for
C       solving the differential equations for the electron's
C       motion to calculate the position of the electron after
C       each time step.  It is called by the program ELTRJ4.
C
        IMPLICIT REAL*8 (A-H,O-Z)
        INTEGER BOUND
C
        VIRTUAL U(141,101)
C
        COMMON /BOUND/ BOUND(141,5)
        COMMON /STATUS/ ELCTRN(7,2)
        COMMON /TIME/ T,DT
        COMMON /STEPFP/ XX,YY,ZZ,XPP,YPP,ZPP,FX,FY,FZ
C
        X=ELCTRN(1,1)
        Y=ELCTRN(2,1)
        Z=ELCTRN(3,1)
        XP=ELCTRN(5,1)
        YP=ELCTRN(6,1)
        ZP=ELCTRN(7,1)
C
        CX1=DT*XP
        CY1=DT*YP
        CZ1=DT*ZP
C
        XX=X
        YY=Y
        ZZ=Z
        XPP=XP
        YPP=YP
        ZPP=ZP
        CALL FP4(U)
        CXP1=DT*FX
        CYP1=DT*FY
        CZP1=DT*FZ
C
```

```
      XX=X+CX1/2.0
      YY=Y+CY1/2.0
      ZZ=Z+CZ1/2.0
      XPP=XP+CXP1/2.0
      YPP=YP+CYP1/2.0
      ZPP=ZP+CZP1/2.0
      CX2=DT*XPP
      CY2=DT*YPP
      CZ2=DT*ZPP
C
      CALL FP4(U)
      CXP2=DT*FX
      CYP2=DT*FY
      CZP2=DT*FZ
C
      XX=X+CX2/2.0
      YY=Y+CY2/2.0
      ZZ=Z+CZ2/2.0
      XPP=XP+CXP2/2.0
      YPP=YP+CYP2/2.0
      ZPP=ZP+CZP2/2.0
      CX3=DT*XPP
      CY3=DT*YPP
      CZ3=DT*ZPP
C
      CALL FP4(U)
      CXP3=DT*FX
      CYP3=DT*FY
      CZP3=DT*FZ
C
      XX=X+CX3
      YY=Y+CY3
      ZZ=Z+CZ3
      XPP=XP+CXP3
      YPP=YP+CYP3
      ZPP=ZP+CZP3
      CX4=DT*XPP
      CY4=DT*YPP
      CZ4=DT*ZPP
C
      CALL FP4(U)
      CXP4=DT*FX
      CYP4=DT*FY
      CZP4=DT*FZ
C
```

```
      ELCTRN(1,2)=X
      ELCTRN(2,2)=Y
      ELCTRN(3,2)=Z
      ELCTRN(4,2)=DSQRT(X**2+Y**2)+1.0D0
      ELCTRN(5,2)=XP
      ELCTRN(6,2)=YP
      ELCTRN(7,2)=ZP
C
      ELCTRN(1,1)=X+(CX1+2.0D0*(CX2+CX3)+CX4)/6.0D0
      ELCTRN(2,1)=Y+(CY1+2.0D0*(CY2+CY3)+CY4)/6.0D0
      ELCTRN(3,1)=Z+(CZ1+2.0D0*(CZ2+CZ3)+CZ4)/6.0D0
      ELCTRN(4,1)=DSQRT(ELCTRN(1,1)**2+ELCTRN(2,1)**2)+1.0D0
      ELCTRN(5,1)=XP+(CXP1+2.0D0*(CXP2+CXP3)+CXP4)/6.0D0
      ELCTRN(6,1)=YP+(CYP1+2.0D0*(CYP2+CYP3)+CYP4)/6.0D0
      ELCTRN(7,1)=ZP+(CZP1+2.0D0*(CZP2+CZP3)+CZP4)/6.0D0
C
      T=T+DT
C
      RETURN
      END
C
C     ***************************************************************
C
      SUBROUTINE FP4(U)
C     This routine calculates the values of the second-derivatives
C     wrt time of the electron's position X,Y,Z.  It is called by
C     the routine STEP4.
C
      IMPLICIT REAL*8 (A-H,O-Z)
      INTEGER BOUND
C
      VIRTUAL U(141,101)
C
      COMMON /BOUND/ BOUND(141,5)
      COMMON /MAG/ BX,BY,BZ
      COMMON /STEPFP/ X,Y,Z,XP,YP,ZP,FX,FY,FZ
      COMMON /GRADV/ I,J,R,ZZ,DVR,DVZ
      COMMON /POT/ VV,VR
C
      A=X**2+Y**2
      IF(A .LE. 0.0D0) R=1.0D0
      IF(A .GT. 0.0D0) R=DSQRT(A)+1.0D0
      ZZ=Z
      I=IDINT(Z+0.5D0)
      IF(I .LE. 1) I=2
```

```
      IF(I .GE. 115) I=114
      J=IDINT(R+0.5D0)
      IF(J .GT. BOUND(I,2)) J=BOUND(I,2)
C
      IF(J .EQ. 1) CALL GV04(U)
      IF(J.GT.1 .AND. J.LT.(BOUND(I,3)-1)) CALL GV14(U)
      IF(J .GE. (BOUND(I,3)-1)) CALL GV24(U)
C
      QM=2.814087D-2
      QB=1.758805D-2
      IF(R .NE. 1.0D0) FX=QM*X*(VV/VR)*DVR/(R-1.0D0)+QB*(ZP*BY-YP*BZ)
      IF(R .EQ. 1.0D0) FX=QB*(ZP*BY-YP*BZ)
      IF(R .NE. 1.0D0) FY=QM*Y*(VV/VR)*DVR/(R-1.0D0)+QB*(XP*BZ-ZP*BX)
      IF(R .EQ. 1.0D0) FY=QB*(XP*BZ-ZP*BX)
      FZ=QM*(VV/VR)*DVZ+QB*(YP*BX-XP*BY)
C
      RETURN
      END
C
C     ****************************************************************
C
      SUBROUTINE GV04(U)
C     This routine calculates the gradient of the potential on the
C     axis of the tube for the program ELTRJ4.
C
      IMPLICIT REAL*8 (A-H,O-Z)
C
      VIRTUAL U(141,101)
C
      COMMON /GRADV/ I,J,R,Z,DVR,DVZ
C
      DR=R-J
      DZ=Z-I
C
      DVR0=0.0D0
      DVZ0=(U(I+1,1)-U(I-1,1))/2.0D0
      DVZZ0=U(I+1,1)-2.0D0*U(I,1)+U(I-1,1)
      DVRR0=-0.5D0*DVZZ0
      DVRZ0=0.0D0
C
      DVR=DVR0+DVRR0*DR+DVRZ0*DZ
      DVZ=DVZ0+DVRZ0*DR+DVZZ0*DZ
C
      RETURN
      END
```

```
C
C       ****************************************************************
C
        SUBROUTINE GV14(U)
C       This routine calculates the gradient of the potential for the
C       normal case; for the program ELTRJ4.
C
        IMPLICIT REAL*8 (A-H,O-Z)
C
        VIRTUAL U(141,101)
C
        COMMON /GRADV/ I,J,R,Z,DVR,DVZ
C
        DR=R-J
        DZ=Z-I
C
        DVR0=(U(I,J+1)-U(I,J-1))/2.0D0
        DVRR0=U(I,J+1)-2.0D0*U(I,J)+U(I,J-1)
        DVZ0=(U(I+1,J)-U(I-1,J))/2.0D0
        DVZZ0=U(I+1,J)-2.0D0*U(I,J)+U(I-1,J)
        DVRZ0=(U(I+1,J+1)+U(I-1,J-1)-U(I+1,J-1)-U(I-1,J+1))/4.0D0
C
        DVR=DVR0+DVRR0*DR+DVRZ0*DZ
        DVZ=DVZ0+DVRZ0*DR+DVZZ0*DZ
C
        RETURN
        END
C
C       ****************************************************************
C
        SUBROUTINE GV24(U)
C       This routine calculates the gradient of the potential near the
C       boundaries for the program ELTRJ4.
C
        IMPLICIT REAL*8 (A-H,O-Z)
C
        VIRTUAL U(141,101)
C
        COMMON /GRADV/ I,J,RR,Z,DVR,DVZ
        COMMON /STAR/ P,Q,R,S
C
        DR=RR-J
        DZ=Z-I
C
        CALL EPQRS4(I,J)
```

```
C
      UP=0.0D0
      UQ=0.0D0
      UR=U(I,J-1)
      US=0.0D0
      IF(P .GE. 1.0D0) UP=U(I,J+1)
      IF(Q .GE. 1.0D0) UQ=U(I-1,J)
      IF(S .GE. 1.0D0) US=U(I+1,J)
C
      DVR0=(UP*R**2+(P**2-R**2)*U(I,J)-UR*P**2)/(P*R**2+R*P**2)
      DVRR0=2.0D0*((UP/P+UR/R)/(P+R)-U(I,J)/(P*R))
      DVZ0=(US*Q**2+(S**2-Q**2)*U(I,J)-UQ*S**2)/(S*Q**2+Q*S**2)
      DVZZ0=2.0D0*((US/S+UQ/Q)/(Q+S)-U(I,J)/(Q*S))
      DVRZ0=U(I,J)-U(I+1,J-1)+DVZ0-DVR0+(DVRR0+DVZZ0)/2.0D0
C
      DVR=DVR0+DVRR0*DR+DVRZ0*DZ
      DVZ=DVZ0+DVRZ0*DR+DVZZ0*DZ
C
      RETURN
      END
C
C     *************************************************************
C
      SUBROUTINE EPQRS4(I,J)
C     This routine calculates the length of the branches of the
C     star for the program ELTRJ4.
C
      IMPLICIT REAL*8 (A-H,O-Z)
C
      COMMON /STAR/ P,Q,R,S
C
      IF(I.LE.33) GO TO 1
      IF(I.GE.34 .AND. I.LE.74) GO TO 2
      IF(I.GE.75 .AND. I.LE.129) GO TO 3
      IF(I.GE.130) GO TO 4
C
  1   P=1.0D0+DSQRT(1.5376D4-(1.25D2-I)**2)-J
      Q=I-1.25D2+DSQRT(1.5376D4-(J-1.0D0)**2)
      S=1.0D0
      GO TO 5
C
  2   P=4.2D1+DSQRT(3.481D3-(7.42D1-I)**2)-J
      Q=I-7.42D1+DSQRT(3.481D3-(4.2D1-J)**2)
      S=1.0D0
      GO TO 5
```

```
C
  3     P=4.2D1+DSQRT(3.481D3-(7.42D1-I)**2)-J
        Q=1.0D0
        S=7.42D1+DSQRT(3.481D3-(4.2D1-J)**2)-I
        GO TO 5
C
  4     P=7.8D1-DSQRT(7.84D2-(1.53D2-I)**2)-J
        Q=1.0D0
        S=1.53D2-DSQRT(7.84D2-(7.8D1-J)**2)-I
C
 5      IF(P.GE.1.0D0) P=1.0D0
        IF(Q.GE.1.0D0) Q=1.0D0
        R=1.0D0
        IF(S.GE.1.0D0) S=1.0D0
C
        RETURN
        END
C
C       ****************************************************************
C
        SUBROUTINE PSCHK4(IPC)
C       This routine returns an integer which is determined from the
C       electron's postion.  It is called by program ELTRJ4.
C
        IMPLICIT REAL*8 (A-H,O-Z)
C
        COMMON /STATUS/ ELCTRN(7,2)
        COMMON /HIT/ XHIT,YHIT,RHIT,THIT,POL,AZI
C
        IF(ELCTRN(3,1) .GT. 93.0D0) GO TO 10
        IPC=1
        RETURN
C
 10     CONTINUE
        IF(ELCTRN(4,1) .LT. 39.0D0) GO TO 40
        IF(ELCTRN(4,2) .LT. 39.0D0) GO TO 20
        IPC=3
        RETURN
C
 20     CONTINUE
        CALL ECTRD4(Z1)
        IF(Z1 .GE. 93.0D0) GO TO 30
        IPC=3
        RETURN
C
```

```
 30     CONTINUE
        IPC=2
        RETURN
C
 40     CONTINUE
        IF(ELCTRN(4,2) .LT. 39.0D0) GO TO 50
        CALL ECTRD4(Z1)
        IF(Z1 .LT. 93.0D0) GO TO 50
        IPC=2
        RETURN
C
 50     CONTINUE
        IF(ELCTRN(3,1) .GT. 105.0D0) GO TO 60
        IPC=1
        RETURN
C
 60     CONTINUE
        IF(ELCTRN(3,1) .GE. 115.0D0) GO TO 80
        IF(ELCTRN(4,1) .LT. 27.0D0) GO TO 70
        IPC=2
        RETURN
C
 70     CONTINUE
        IPC=1
        RETURN
C
 80     CONTINUE
        CALL DYNOD4
        IF(RHIT .GE. 16.2D0) GO TO 90
        IPC=4
        RETURN
C
 90     CONTINUE
        IPC=5
        RETURN
C
        END
C
C       *****************************************************************
C
        SUBROUTINE ECTRD4(Z1)
C       This routine calculates the intercept of the electron's path
C       with the cylinder of the outer electrode.  It is called by
C       the routine PSCHK4.
C
```

```
      IMPLICIT REAL*8 (A-H,O-Z)
C
      COMMON /STATUS/ ELCTRN(7,2)
C
      A=(ELCTRN(1,1)-ELCTRN(1,2))**2+(ELCTRN(2,1)-ELCTRN(2,2))**2
      B=ELCTRN(1,2)*(ELCTRN(1,1)-ELCTRN(1,2))
      B=2.0D0*(B+ELCTRN(2,2)*(ELCTRN(2,1)-ELCTRN(2,2)))
      C=ELCTRN(1,2)**2+ELCTRN(2,2)**2-1.444D3
      T=(-B+DSQRT(B*B-4.0D0*A*C))/(2.0D0*A)
      IF(T.GE.0.0D0 .AND. T.LE.1.0D0) GO TO 10
      T=(-B-DSQRT(B*B-4.0D0*A*C))/(2.0D0*A)
 10   CONTINUE
      Z1=ELCTRN(3,2)+(ELCTRN(3,1)-ELCTRN(3,2))*T
C
      RETURN
      END
C
C     ****************************************************************
C
      SUBROUTINE DYNOD4
C     This routine calculates the position of the hit with the
C     flat plate.  It is called by routine PSCHK4.
C
      IMPLICIT REAL*8 (A-H,O-Z)
C
      COMMON /STATUS/ ELCTRN(7,2)
      COMMON /HIT/ XHIT,YHIT,RHIT,THIT,POL,AZI
      COMMON /TIME/ T,DT
C
      TEMP=(115.0D0-ELCTRN(3,2))/(ELCTRN(3,1)-ELCTRN(3,2))
      THIT=T+(TEMP-1.0D0)*DT
      XHIT=ELCTRN(1,2)+(ELCTRN(1,1)-ELCTRN(1,2))*TEMP
      YHIT=ELCTRN(2,2)+(ELCTRN(2,1)-ELCTRN(2,2))*TEMP
      RHIT=DSQRT(XHIT**2+YHIT**2)+1.0D0
      IF(RHIT .NE. 1.0D0) GO TO 10
      POL=1.570796327D0
      AZI=0.0D0
      GO TO 20
 10   CONTINUE
      POL=DSQRT((ELCTRN(1,2)-XHIT)**2+(ELCTRN(2,2)-YHIT)**2)
      POL=DATAN((115.0D0-ELCTRN(3,2))/POL)
      AZI=DATAN((ELCTRN(2,2)-YHIT)/(ELCTRN(1,2)-XHIT))
 20   CONTINUE
C
C     Convert to cm's and degrees.
```

```
C
         XHIT=XHIT/4.0D0
         YHIT=YHIT/4.0D0
         POL=9.0D1-POL*57.29577951D0
         AZI=AZI*57.29577951D0
C
         RETURN
         END
```

Bibliography

[Aa87] G. Aardsma, R.C. Allen, J.D. Anglin, M. Bercovitch, A.L. Carter, H.H. Chen, W.F. Davidson, P.J. Doe, E.D. Earle, H.C. Evans, G.T. Ewan, E.D. Hallman, C.K. Hargrove, P. Jagam, D. Kessler, H.W. Lee, J.R. Leslie, J.D. MacArthur, H.-B. Mak, A.B. MacDonald, W. McLatchie, B.C. Robertson, J.J. Simpson, D. Sinclair, P. Skensved and R.S. Storey, Phys. Lett. **B194** (1987), 321.

[Ah83] A. Ahrens, S.H. Aronson, P.L. Connolly, T.E. Erickson, B.G. Gibbard, M. Montag, M.J. Murtagh, S.J. Murtagh, S. Terada, A.M. Thorndike, W.G. Walker, P.J. Wanderer, D.H. White, J.L. Callas, D. Cutts, R.S. Dulude, B.W. Hughlock, R.E. Lanou, J.T. Massimo, T. Shinkawa, K. Amako, S. Kabe, Y. Nagashima, Y. Suzuki, S. Tatsumi, K. Abe, E.W. Beier, D.C. Doughty, L.S. Durkin, R.S. Galik, S.M. Heagy, M. Hurley, A.K. Mann, F.M. Newcomer, R. Van Berg, H.H. Williams, T. York, P. Clarke, D. Hedin, M.D. Marx, E. Stern and T. Miyachi, Phys. Lett. **51** (1983), 1514.

[Al85] R.C. Allen, V. Bharadwaj, G.A. Brooks, H.H. Chen, P.J. Doe, R. Hausammann, W.P. Lee, H.J. Mahler, M.E. Potter, A.M. Rushton, K.C. Wang, T.J. Bowles, R.L. Burman, R.D. Carlini, D.R.F. Cochran, J.S. Frank, E. Piasetzky, V.D. Sandberg, D.A. Krakauer and R.L. Talaga, Phys. Rev. Lett. **55** (1985), 2401.

[An74] J.R. Andrews, Rev. Sci. Instrum. **45** (1974), 22.

[Ba85] J.N. Bahcall, in *Solar Neutrinos and Neutrino Astronomy (Homestake 1984)*, AIP Conf. Proc. **126** (1985), 60.

[Ba86] J.N. Bahcall, S.V. Petcov, S. Toshev and J.W.F. Valle, Phys. Lett. **B181** (1986), 369.

[Be85] C.A. Benulis and W.K. McFarlane, NIM **A240** (1985), 135.

[Br77] D.J. Bradley, M.B. Allenson and B.R. Holeman, J. Phys. D: Appl. Phys. **10** (1977), 111.

[Ch85] H.H. Chen, Phys. Rev. Lett. **55** (1985), 1534.

[Da85] M.B. Das, S. Bose and R. Bhattacharya, NIM **A242** (1985), 156.

[Fr79] D.L. Franzen and G.W. Day, Rev. Sci. Instrum. **50** (1979), 1029.

[Ge80] C.F. Gerald, *Applied Numerical Analysis 2nd Ed.*, Addison-Wesley, Reading, Mass., 1978.

[Gr78] D.R. Green, NIM **151** (1978), 307.

[Ha82] Hamamatsu Technical Data Sheet, Catalog No. PM-250, T82-9-2.

[Ha85] Hamamatsu Photonics K.K., *Photomultiplier Tubes for Scintillator Counting & High Energy Physics*, SEP/85 (1985).

[Hu80] Khalaf A.Z.A. Hussain and D.K. Butt, NIM **173** (1980), 471.

[Ke66] F.J. Kelly and H. Uberall, Phys. Rev. Lett. **16** (1966), 145.

[Ku76] B. Kuchowicz, Rep. Prog. Phys. **39** (1976), 291.

[Ku83] H. Kume, S. Sawaki, M. Ito, K. Arisaka, T. Kajita, A. Nishimura and A. Suzuki, NIM **205** (1983), 443.

[Le75] B. Leskovar and C.C. Lo, NIM **123** (1975), 145.

[Le87] J.R. Leslie, private communication, (1987).

[Mc87] W. McLatchie and E.D. Earle, *The Sudbury Neutrino Observatory*, Internal report SNO-87-6, August 1987.

[Mi65] J. Millman and H. Taub, *Pulse, Digital and Switching Waveforms*, McGraw-Hill, New York, 1965, 308.

[Mo77] M. Moszynski and J. Vacher, NIM **141** (1977), 319.

[Na70] R. Nathan and C.H.B. Mee, Phys. Stat. Solidi (a) **2** (1970), 67.

[Ph70] *Philips Data Handbook, Electron Tubes* Part 6, June 1970.

[Po72] S.K. Poultney, Advan. Elec. Electron Phys. **31** (1972), 39.

[Po79] J. Pouthas and M .Engrand, NIM **161** (1979), 331.

[Rc80] R.W. Engstrom, *RCA Photomultiplier Handbook*, Technical Series PMT-62, RCA Solid State Division, Electo-Optics and Devices, Lancaster, PA, (1980).

[Ro85] J.K. Rowley, B.T. Cleveland and R. Davis, Jr., in *Solar Neutrinos and Neutrino Astronomy (Homestake 1984)*, AIP Conf. Proc. **126** (1985), 1.

[Sn87] G.T. Ewan *et al.*, *The Sudbury Neutrino Observatory Proposal 1987.*

[Su87] A. Suzuki, private communication, (1987).

[Wo79] L. Wolfenstein, Phys. Rev. **D20** (1979), 2634.

Vita

Name:	Robert John Komar
Place and year of birth:	Sudbury, Ontario, 1963
Education:	Ontario primary and secondary schools; completed Grade XIII 1981
	Queen's University 1981-85; awarded B.Sc. Eng. (Physics) 1985
	Queen's University 1985-87; present program
Experience:	Summer Student (Nuclear Physics) Queen's University 1984, 1985
	Teaching Assistant (Physics) Queen's University 1985-86, 1986-87
Awards:	Ontario Scholarship, 1981
	Susan Near Scholarship, Queen's University, 1984
	Dean's Award, Queen's University, 1984
	G. Neilson Whyte Fellowship, Queen's University, 1985-86
	Reinhardt Fellowship, Queen's University, 1986-87, 1987